UNIVERSITÉ DE NANTES
FACULTÉ DES SCIENCES ET DES TECHNIQUES

———

ÉCOLE DOCTORALE Végétal, Environnement, Nutrition, Agroalimentaire, Mer (VENAM)

Année 2014

Caractérisation de la microstructure spatiale de la pomme en lien avec ses propriétés mécaniques par des méthodes quantitatives d'IRM

———————

THÈSE DE DOCTORAT
Discipline : Sciences
Spécialité : Biophysique

Présentée
et soutenue publiquement par

Guillaume WINISDORFFER

Le 12 décembre 2014, devant le jury ci-dessous

Président	Serge AKOKA, Professeur, Université de Nantes
Rapporteurs	Geneviève GUILLOT, Chargée de recherche, Université Paris-Sud - 11
	Bart NICOLAI, Professor, KU Leuven
Examinateurs	Nadia BERTIN, Directeur de recherche, INRA
	Serge AKOKA, Professeur, Université de Nantes

Directeurs de thèse :
Marc LAHAYE, directeur de recherche, INRA
François MARIETTE, directeur de recherche, IRSTEA

Co-encadrante : Maja MUSSE, chargée de recherche, IRSTEA

Remerciements

Remerciements

Ce projet a été l'objet d'une réalisation scientifique entre l'équipe IRM-Food d'Irstea (Rennes) et l'équipe PVPP de l'INRA (Nantes) et a été financé par les régions Bretagne et Pays de La Loire. Je tiens donc à remercier chacune de ces parties sans lesquelles il n'aurait jamais vu le jour.

Je souhaiterais remercier toutes les personnes qui ont contribué, de près ou de loin, lors de ces trois années, à l'avancée de cette thèse et sans qui ce travail n'aurait pas été possible.

Je remercie en premier lieu mes directeurs, François Mariette et Marc Lahaye, ainsi que mon encadrante Maja Musse, pour leur implication, leur travail et leur disponibilité. Merci pour votre patience et vos conseils ainsi que votre motivation qui m'ont beaucoup apporté et permis d'aller au bout de ce projet.

Pour leur aide dans l'organisation (parfois compliquée) et la réalisation de la partie expérimentale de cette thèse, j'adresse mes plus vifs remerciements à Stéphane Quellec pour m'avoir familiarisé avec l'IRM et Mireille Cambert pour le pendant RMN des mesures, ainsi qu'à Sylvain Challois pour ses réponses à mes problèmes de traitement de données.

Pour leurs apports scientifiques et humains, j'adresse également mes remerciements à Mickaël Delaire, dont l'implication et les connaissances en biologie végétale m'ont grandement aidé, Marie-Françoise Devaux pour m'avoir initié à la macro-vision et ses traitements et Adelin Barbacci pour son aide scientifique et technique sur la mécanique du fruit.

Merci également à Sophie Le Gall et Laurent Helary pour leur aide dans la réalisation des mesures de chimie et d'imagerie.

J'adresse également mes remerciements à Mesdames et Messieurs les membres du jury, qui ont accepté de lire et de juger ce travail : M^{me} Geneviève Guillot et M. Bart Nicolai en tant que rapporteurs, M^{me} Nadia Bertin et M. Serge Akoka en tant qu'examinateurs.

Un grand merci à tous les membres d'Irstea pour leur amitié, leur gentillesse et leur bonne humeur quotidienne, et en particulier à Julie, Clément, Julien, Ruzica, Yves, Yannick, Delphine et Cécile.

Enfin merci à ma famille et mes amis pour leur écoute, leurs encouragements et leur soutien constant, et en particulier à Laura, pour toutes ces raisons et bien d'autres.

A ma famille,

Abréviations

Liste des abréviations utilisées/Abbreviations

IRM/MRI: Imagerie par Résonance Magnétique/Magnetic Resonance Imaging

RMN/NMR: Résonance Magnétique Nucléaire/Nuclear Magnetic Resonance

RSB/SNR: Rapport Signal sur Bruit/Signal Noise Ratio

GSC: Gradient de Sélection de Coupe

MSE: Multi-Spin Echo

MGE: Multi-Gradient Echo

TE: Temps d'Echo/Echo Time

TR: Temps de répétition/Repetition Time

τ: Espace inter-pulse/Pulse spacing

RD: Délai de récupération/Recovery Delay

σ: Contrainte/Stress

ε: Déformation/Strain

E: Module d'Young/Young's modulus

HG: HomoGalacturonan

RG: RhamnoGalacturonan

DM: Degré de Méthylesterification/Degree of Methylesterification

DA: Degré d'Acétylation/Degree of Acetylation

WC: Water Content

MIA/AIM: Matériel Insoluble à l'Alcool/Alcohol Insoluble Material

SSC: Soluble Solid Content

UA: Uronic Acid

PCA: Principal Component Analysis

MANOVA: Multiple factor ANalysis Of Variance

Table of contents

Introduction

Introduction

Ce projet de thèse s'inscrit dans cadre du projet AI-Fruit qui vise à caractériser, mesurer, intégrer et modéliser les rôles et fonctions des différents acteurs clés de la qualité de la pomme. De par sa place de troisième fruit produit dans le monde, elle est d'un intérêt particulier pour la recherche. Dans l'optique d'arriver à une sélection variétale raisonnée et une maîtrise de la qualité de la pomme dans ses diverses utilisations (fraiche, transformée), le projet AI–Fruit développe une approche multidisciplinaire alliant des démarches biologiques et relevant des sciences des aliments ainsi que des approches issues du domaine de la physique et des mathématiques appliquées. Ce projet fait intervenir différents partenaires : INRA ACO IRHS, ENSAM LAMPA, ESA GRAPPE, ONIRIS, Université d'Angers LASQUO, Université d'Angers LISA, Université d'Angers LAUM et Université d'Angers IMMM. Dans ce contexte, ce travail de thèse a cherché à relier la microstructure du fruit caractérisée par IRM aux propriétés physicochimiques et mécaniques du fruit. Dans cette optique, deux points majeurs sont abordés : d'un côté la hiérarchisation de l'influence des caractéristiques histologiques, biophysiques et biochimiques sur les mécanismes de relaxation RMN, et de l'autre l'évaluation des potentialités de l'IRM quantitative pour identifier les caractéristiques du fruit intervenant sur les propriétés mécaniques des tissus. De façon originale, ce travail a utilisé des méthodes récemment mises au point au sein de l'équipe IRM-Food (TEAA-IRSTEA) à savoir la mesure de la porosité apparente et la possibilité d'extraire des signaux de relaxation transversale multi-exponentielle à partir d'une séquence IRM appropriée. En effet, jusqu'à ce jour les approches IRM pour la caractérisation des fruits étaient basées sur des signaux de relaxation mono-exponentiels. Or il est connu que cette approche mono-exponentielle est une approximation d'un comportement de relaxation RMN plus complexe. De plus, l'analyse multi-exponentielle permet d'estimer différentes fractions de molécules d'eau en lien avec l'organisation interne des tissus végétaux. Ainsi cette démarche serait plus juste et plus sensible que les mesures mono-exponentielles.

Le travail expérimental a été décomposé en plusieurs étapes :

- Une première étape a consisté en l'étude de l'influence de la taille des cellules sur la relaxation multi-exponentielle. Cette démarche a été

entreprise sur une même variété puis son extrapolation a été évaluée sur d'autres variétés.

- Une deuxième étape a été centrée sur le comportement des pommes au stockage comme levier permettant de moduler les propriétés mécaniques du parenchyme. Pour cette étape, une large gamme de variétés et de fruits a été sélectionnée afin d'évaluer la généralisation des résultats.

Une approche multi-instrumentale a été appliquée, permettant d'identifier les caractéristiques physiologiques (microporosité, répartition de l'eau dans les cellules, teneur en eau, etc.) et la composition globale des tissus et des parois.

Cinq chapitres constituent cette thèse. Dans un premier temps, une synthèse bibliographique abordera l'IRM ainsi que la pomme, sa texture, et les mesures instrumentales qui en sont faites. Le deuxième chapitre est centré sur l'étude par IRM de la compartimentation intracellulaire de l'eau et de la microporosité au sein du fruit. Le troisième chapitre décrit l'analyse des propriétés mécaniques dynamiques du péricarpe en lien avec l'état de l'eau et la distribution du gaz estimés par IRM ainsi que les propriétés histologiques et la composition chimique du tissu. Le quatrième chapitre s'intéresse à l'évolution de la distribution spatiale de la répartition de l'eau au sein des cellules dans un fruit entier en fonction du stockage. Enfin, une discussion générale mettra en exergue les liens entre les différents résultats et aboutira à une conclusion générale permettant de dégager les perspectives de ce travail.

Ce travail a été réalisé dans deux laboratoires : à IRSTEA de Rennes (TEAA : Technologie des Equipements Agro-Alimentaires, équipe IRM-Food) sous la direction de François Mariette et encadré par Maja Musse et à l'INRA de Nantes (Biopolymères, Interactions, Assemblages ; équipe Parois Végétales et Polysaccharides Pariétaux) sous la direction de Marc Lahaye.

Ce travail a été financé par les régions Bretagne et Pays de la Loire dans le cadre du projet AI-Fruit.

Chapitre 1 :
Etude Bibliographique et Objectifs

1. Etude bibliographique et objectifs

I. LA POMME

La pomme est un fruit charnu provenant d'un ovule inférieur et composé en majorité de tissu extra-carpellaire (ne provenant pas du pistil). Le tissu carpellaire est appelé vrai fruit alors que le tissu extra-carpellaire est appelé faux fruit (Esau, 1977). La pomme fait partie des fruits qui se ramollissent modérément au cours du mûrissement et gardent une texture croquante et cassante (Toivonen and Brummell, 2008). Dans le cadre de ce travail, nous nous intéresserons à la structure du fruit et comment elle peut être liée aux propriétés mécaniques et en conséquence à la texture.

1) Anatomie

Au cours de la formation du fruit, les tissus se différencient en cinq structures principales : le cœur (apparenté au vrai fruit), les vaisseaux conducteurs, le parenchyme, le derme et la cuticule (ces quatre derniers étant apparentés au faux fruit) (Figure 1-1).

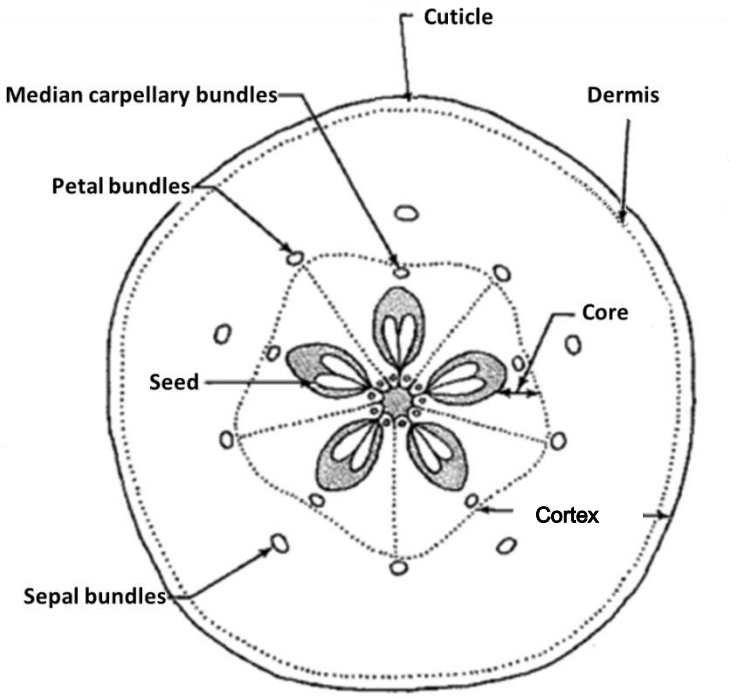

Figure 1-1 modifiée de Esau, 1977 : Schéma d'une coupe radiale de la pomme.

Le parenchyme représente, dans le fruit mature, la majorité du tissu. Il compose la très grande majorité du cortex et on le retrouve dans le cœur du fruit. Le derme est composé de l'épiderme et de l'hypoderme, ses cellules croissent en taille depuis la cuticule vers l'intérieur du fruit. Les cellules proches du derme sont à peu près circulaires et font 50 µm de diamètre. Vers l'intérieur du fruit, les cellules atteignent 300 µm et s'allongent radialement vers le cœur pour former des structures en colonnes (Figure 1-2). Entre ces cellules, il y a des régions d'air que l'on appelle espaces intercellulaires. Dans le cortex, en progressant vers l'intérieur du fruit, les cellules sont mieux organisées et les espaces intercellulaires réduits.

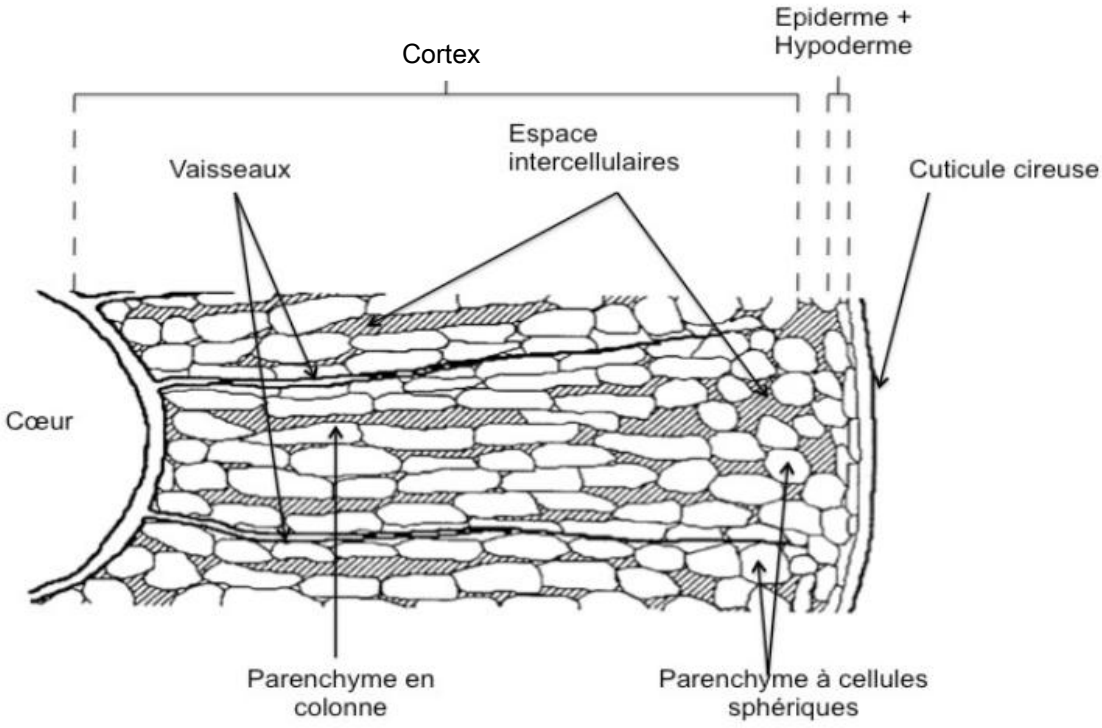

Figure 1-2 modifiée de Khan and Vincent, 1990 : Représentation d'une coupe radiale du cortex de la pomme.

La porosité (fraction volumique occupée par du gaz) du parenchyme de la pomme est estimée dans quelques études par micro RX entre 15% et 32% (Herremans et al., 2013; Verboven et al., 2008). Des modélisations du fruit ont été réalisées afin d'en comprendre la structure, s'aidant de la microtomographie RX (Mebatsion et al., 2009) : Le fruit est modélisé ayant une partie solide (paroi cellulaire) et une partie liquide et gazeuse (les cellules et les espaces intercellulaires). Les cellules sont approximées par

des ellipses entre lesquelles on trouve du gaz. Ces travaux de modélisation ont pour perspective la simulation du comportement du tissu durant des tests mécaniques, durant la croissance du fruit ou suite à des affections des tissus comme le *watercore* ou le brunissement pour mieux comprendre les mécanismes mis en jeu.

a. *La cellule végétale*

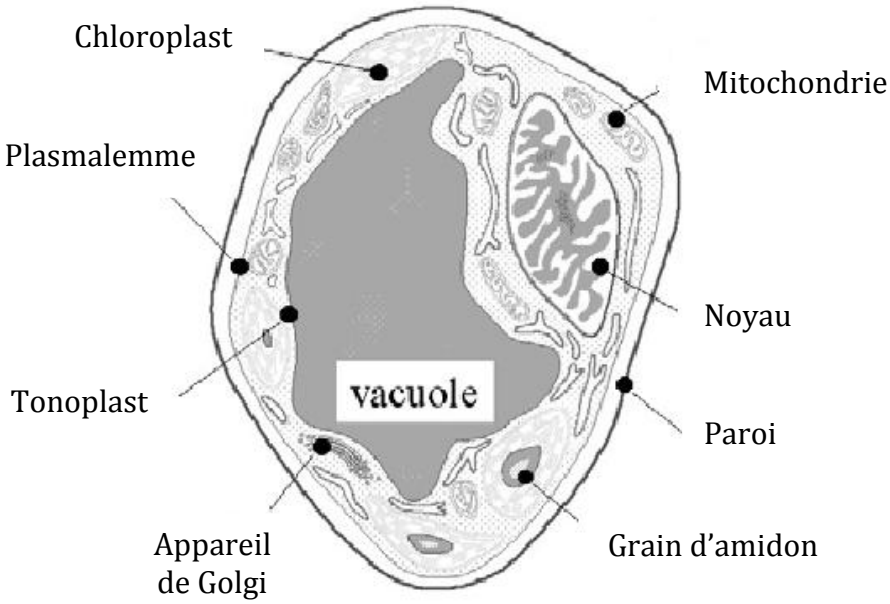

Figure 1-3 : Schéma d'une cellule végétale

La cellule végétale (Figure 1-3) est composée de plusieurs compartiments dont les principaux sont la vacuole, qui centralise environ 80% de l'eau cellulaire, le cytoplasme et la paroi cellulaire. Le cytoplasme est composé d'eau (le cytosol) dans laquelle se trouve un certain nombre d'organites. On y trouve aussi les éléments du cytosquelette de la cellule (microtubules et actine) ainsi que, pour les fruits, des granules d'amidon sous forme d'amyloplastes. C'est le cas pour la pomme où le stade de régression de l'amidon permet d'établir la maturité du fruit (Vaysse P., 2004).

Au niveau cellulaire, il existe une pression exercée par les fluides vacuolaires sur le tonoplaste, le plasmalemme et la paroi cellulaire. Elle est due à la différence de

concentration en osmolites (sucres, acides aminés, ions, acides organiques…) entre les compartiments cellulaires internes (vacuole, cytoplasme) et externes (apoplaste), appelée pression de turgescence.

b. Les espaces intercellulaires

Les espaces intercellulaires proviennent d'une rupture ou d'une séparation des cellules : les forme, taille et organisation cellulaire laissent plus ou moins d'espace rempli de gaz. Ces espaces intercellulaires peuvent se connecter au cours du temps (Esau, 1977) et ont donc des formes et des tailles variables qui peuvent dépendre à la fois du tissu considéré dans le fruit (Khan and Vincent, 1990) et de la variété (Ting et al., 2013). La fonction de ces espaces est de permettre la respiration du tissu. La microporosité correspond au volume relatif de ces espaces. Elle est indépendante de la teneur en eau (WC), exprimée en fraction massique de l'eau dans ce travail.

c. La paroi cellulaire

Les parois englobent les cellules et sont séparées des parois voisines par la lamelle moyenne qui a un rôle d'adhésif. La paroi cellulaire est amenée à changer durant la vie de la cellule : elle accompagne la croissance cellulaire et l'épaisseur et le type de paroi varie d'un type de cellule à un autre (Albersheim et al., 2010b). Comme tous les tissus végétaux, la paroi est essentiellement composée d'eau, à hauteur d'environ 65%. On distingue des parois primaires et secondaires : les parois primaires sont composées de quatre types de macromolécules qui sont de la cellulose, des hémicelluloses, des pectines et des protéines (Albersheim et al., 2010a; Carpita, 2000). Au cours de la vie de la cellule, des couches supplémentaires de paroi peuvent être produites entre la paroi primaire et la membrane cellulaire et forment alors la paroi secondaire. La composition de la paroi secondaire est plus variable ; en général elle contient une plus grande proportion de cellulose que la paroi primaire et moins de pectines, et elle peut être lignifiée. C'est en particulier le cas pour les vaisseaux et les fibres dans les végétaux. Dans la pomme, la paroi primaire est prédominante et il y a très peu de paroi secondaire.

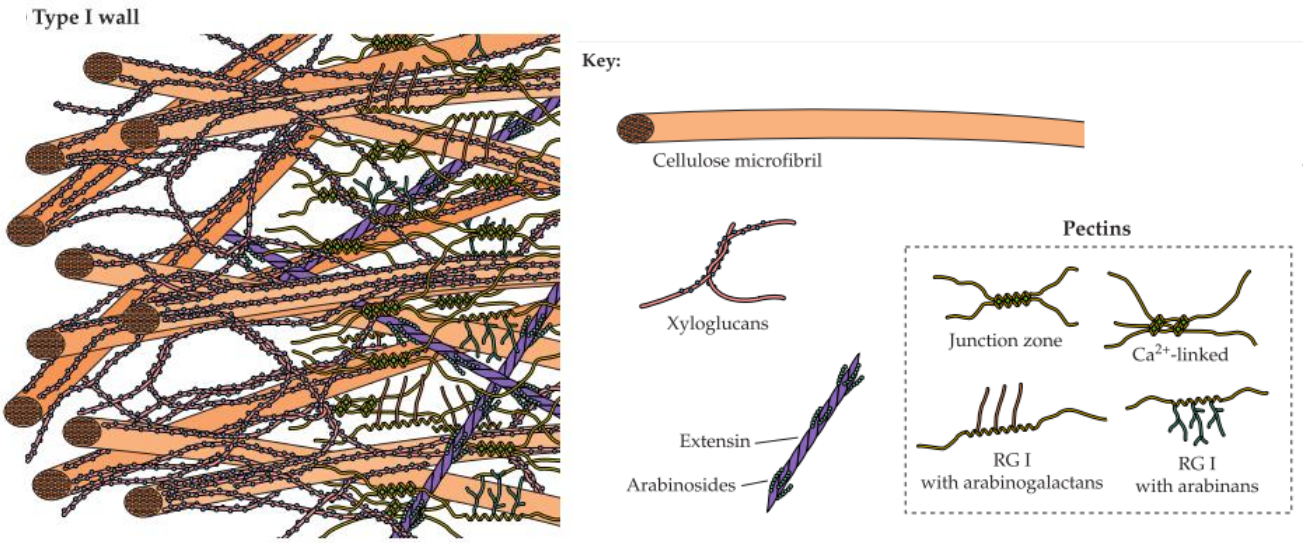

Figure 1-4 extraite de Carpita, 2000: Schéma de la paroi cellulaire.

Les différents polysaccharides de la paroi s'agencent en réseaux (Figure 1-4) (Brummell, 2006; Carpita, 2000; Johnston et al., 2002) : un réseau de microfibres de cellulose rigides inextensibles longues et parallèles dont la région interne est cristalline et hydrophobe et les couches extérieures sont amorphes, sur lequel viennent s'amarrer par liaison hydrogène des hémicelluloses qui forment un second réseau. Les xyloglucanes représentent l'hémicellulose majoritaire. Leur structure est basée sur un squelette de type cellulose sur lequel sont ramifiés des résidus xylose plus ou moins étendus par des résidus galactose et fucose. Ces réseaux baignent dans une matrice de pectines, composant jusqu'à 50% de la paroi pour les fruits. Cette matrice est riche en acides galacturoniques : les homogalacturonans (HG ou HG substitués), et les rhamnogalacturonan-I et –II (RG-I et –II). Ces domaines pectiques sont reliés entre eux par leur squelette et peuvent être liés aux hémicelluloses d'après le modèle actuel (Mohnen, 2008). Les régions HG peuvent être plus ou moins méthylesterifiées en fonction du tissu et de la plante considérés et les régions non-estérifiées sont supposées être les principaux acteurs de la formation de gels. Dans un premier cas, pour un bas degré de méthylesterification (DM < 50, 50% des acides galacturoniques ne sont pas méthylesterifiés sur leur C-6), des chaînes d'acides galactosyluroniques non méthylesterifiées forment des dimères par des liaisons calciques. Dans un second cas, pour un haut degré de méthylesterification (DM > 50), un réseau tridimensionnel se formerait par des liaisons hydrogènes et des interactions hydrophobes. Le réseau de

pectines permet de réguler la porosité de la paroi (Fleischer et al., 1999) en agissant ainsi sur la diffusion et sur l'accès à ses constituants. Elles ont aussi le rôle de réguler l'adhésion cellule-cellule au niveau de la lamelle moyenne.

La paroi comporte enfin de 1 à 10% de protéines de structure, d'enzymes et autres protéines. Les protéines de structure contribuent aux propriétés physiques de la paroi et n'ont pas de propriétés catalytiques. Bien qu'encore à définir, leur rôle influencerait la rigidité, la flexibilité et l'élasticité de la paroi ainsi que sa porosité et son hydratation.

Il existe plusieurs modèles de paroi qui font débat car n'expliquant pas tous les différentes propriétés des parois : le modèle de réseau collant (Carpita, 2000) ('Sticky network', Figure 1-4) implique une interaction hydrogène entre les hémicelluloses situées entre les microfibres de cellulose, les reliant et les maintenant ainsi à distance prévenant leur agrégation. Les pectines formeraient un réseau séparé. Un autre modèle dit multicouche (Talbott and Ray, 1992) ('Multi-coat', Figure 1-5) suppose que les couches d'hémicellulose encadrent les fibres de cellulose, chaque couche successive étant moins fortement liée. Les fibres de cellulose ne sont pas en contact. Les pectines se trouvent entre ces couches d'hémicellulose et permettent de les maintenir. Les xyloglucanes se lient avec la cellulose dans les portions non cristallines de la fibre, laissant une boucle libre. Cette boucle est en contact avec des polymères pectiques arabinane/galactane qui forment une couche supplémentaire par des interactions intermoléculaires faibles et par liaison covalente le cas échéant. Cette couche serait aussi en interaction avec les microfibres de cellulose. Enfin, un gel pectique se logerait entre les microfibres entourées d'hémicelluloses, quelques chaînes des RG se projetant dans la couche d'arabinan/galactan et interagissant avec elle.

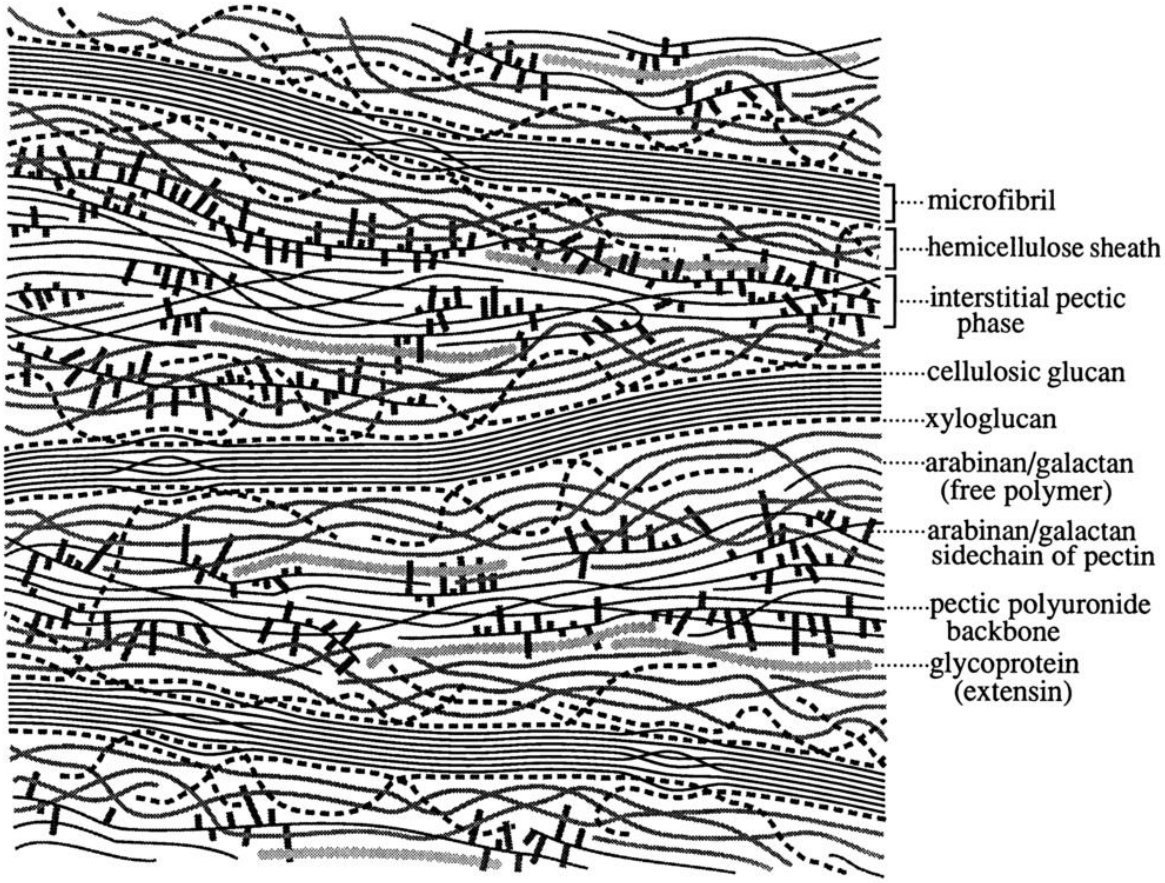

Figure 1-5 (extraite Talbott and Ray, 1992): Schéma de la paroi.

La paroi est en constante évolution. Entre autres, elle possède durant la croissance une dynamique de relâchement et de dépôt de nouveau matériel (Carpita, 2000). Le phénomène de croissance cellulaire permet de mettre en évidence le lien entre la paroi et la pression de turgescence puisque l'équilibre pression de turgescence/relâchement de la paroi est à l'origine de l'élongation des cellules (Burgert and Dunlop, 2011; Cosgrove, 1993).

La matrice de pectine a un rôle très important dans la paroi : elle limite l'accès aux différents composants de cette dernière. De plus, la taille des pores de la paroi peut varier de 4 nm à 10 nm, notamment de par la quantité de liaisons borate-ester (Fleischer et al., 1999), et est souvent limitante dans les processus de diffusion.

L'arrêt de la croissance cellulaire entraine le début de la dé-méthylestérification de la pectine. L'augmentation de la rigidité de la paroi est associée à la perte de solubilité des

extensines et à l'apport de calcium formant des liaison avec la pectine dé-estérifiée (Jackman and Stanley, 1995).

Dans ce travail, la paroi est assimilée au matériel insoluble à l'alcool (MIA ou Alcohol Insoluble Material AIM) qui a été utilisé pour les dosages de sucres et le profilage des saccharides. L'évolution de la paroi au cours de la maturation du fruit sera abordée dans le paragraphe suivant.

2) La texture et son évolution, vues par les mesures instrumentales

La texture est due à plusieurs paramètres qui influent sur la qualité du fruit. Bourne la définit en 1982 (Bourne, 1982) : "La texture est l'ensemble des caractéristiques physiques résultant de la structure des aliments, expérimenté par la sensation de toucher dans la main ou la bouche, lié à la déformation, la décomposition et au comportement soumis à des forces, et mesuré en fonction de la force, de la distance et du temps". Dans le fruit, la texture est déterminée par les caractéristiques structurelles, physiologiques et biochimiques des tissus et leur modification dans le temps à travers les différents stades de développement, maturation et sénescence (Abbott, 2004). Pour le consommateur, la texture correspond à la fermeté et au caractère juteux du fruit (Toivonen and Brummell, 2008). Cependant, il existe quatre déterminants texturaux majeurs que sont la jutosité, la fermeté, le croquant et la farinosité (Daillant-Spinnler et al., 1996; Jaeger et al., 1998). La fermeté dépend de la taille, de la forme et de l'agencement des cellules, de l'épaisseur de la paroi et de la force de l'adhésion cellulaire ainsi que de la pression de turgescence. Plusieurs études ont cherché à relier les déterminants texturaux à des mesures instrumentales dans le but, à terme, de pouvoir faire une mesure systématique de cet attribut de qualité.

a. Texture et propriétés mécaniques

Les tests les plus courants permettant d'évaluer les propriétés mécaniques des végétaux sont les tests de compression et d'étirement. On définit la contrainte (σ) comme la force rapportée à une surface d'application (unité Pa). Une autre grandeur

apparentée est la déformation (ε) définie comme le changement de taille divisé par la taille initiale. Il existe un équivalent de ces deux valeurs pour des forces de cisaillement : la contrainte de cisaillement et la déformation de cisaillement (Burgert and Dunlop, 2011). Lors d'un test, le tracé de σ en fonction de ε permet de révéler les différents régimes suivant lesquels l'échantillon réagit (Figure 1-6).

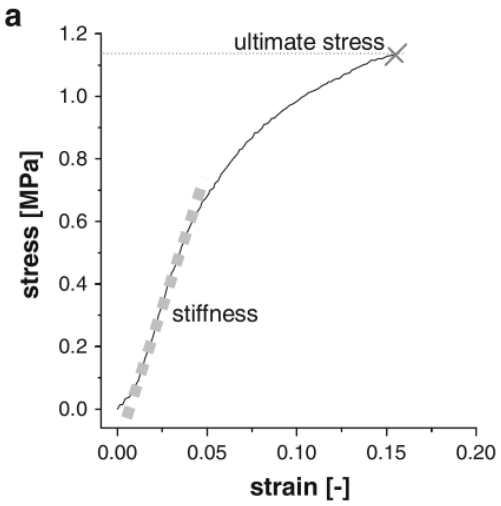

Figure 1-6 extraite de Burgert and Dunlop, 2011: Courbe obtenue par un test de compression sur un tissu d'*Arabidopsis*.

On voit sur cette courbe une première portion, linéaire, correspondant à une réaction purement élastique de l'échantillon : la déformation est réversible. Dans cette première partie de la courbe, la relation entre la contrainte et la déformation permet d'accéder au module d'élasticité ou module d'Young : $E = \frac{\sigma}{\varepsilon}$ (carrés gris).

A partir d'une valeur seuil, notée σ_y, la déformation devient irréversible et la réaction est visco-élastique. Le régime élastique implique un réseau de liaisons fixes alors que le régime visco-élastique implique une réorganisation des liaisons labiles de l'échantillon et les phénomènes biologiques sous-jacents ne sont pas encore élucidés (Burgert and Dunlop, 2011).

Outre ses propriétés élastiques pour lesquelles les tests couramment utilités viennent d'être détaillés, la pomme, comme l'ensemble des fruits charnus, est un matériau visco-élastique (Vincent, 2012) qui n'a pourtant que rarement été étudié

comme tel (Abbott, 1999). Dans la plupart des études, seul le comportement élastique du tissu a été étudié par pénétrométrie, compression ou tension (Harker et al., 1997a). Quelques études en dynamique existent et l'évaluation des propriétés élastiques présente des résultats cohérents avec les tests classiquement utilisés (Varela et al., 2007).

Les mesures de pénétrométrie et de force de rupture en tension et en cisaillement ont été corrélées avec la fermeté du fruit dans différents fruits, dont la pomme (Figure 1-7) (Harker et al., 1997b). Ces mesures permettent d'observer différents comportements liés à la texture : la force de rupture du tissu varie et, si l'on se focalise sur la pomme, le pic arrondi de rupture en cisaillement témoigne d'une rupture progressive alors qu'en tension la rupture est brutale. La mesure de rigidité par les différentes techniques (force nécessaire à la rupture) a montré que le test de tension était le plus à même de distinguer les fruits. Par la suite, des mesures en pénétrométrie ont été reliées au croquant et à la fermeté dans la pomme (Mehinagic et al., 2004) et des mesures en compression et tension de la rigidité ont été reliées aux mêmes déterminants dans la pomme et la poire (Chauvin et al., 2010).

La texture évolue de manière importante durant la maturation du fruit.

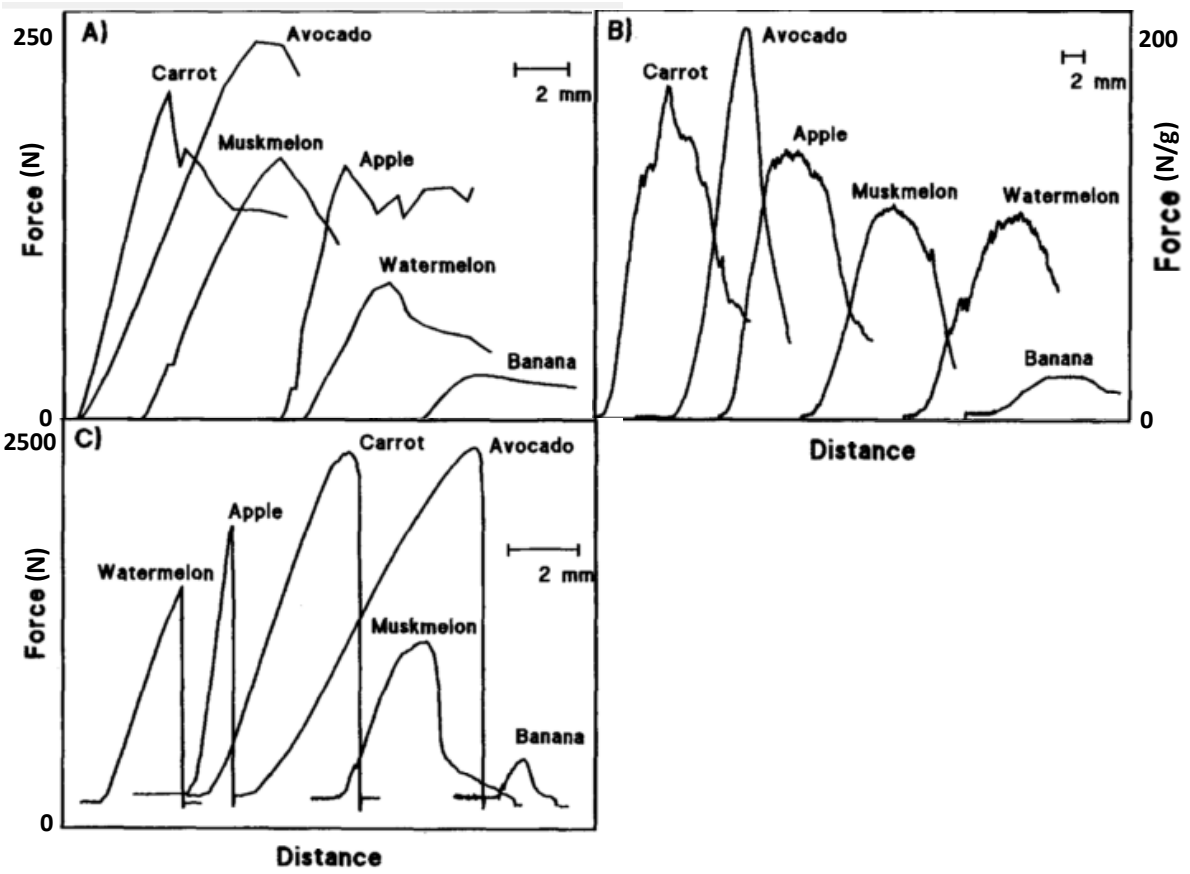

Figure 1-7 : Courbes de la force en fonction de la distance obtenues par des mesures de (A) pénétrométrie, (B) cisaillement, (C) tension, dans le parenchyme de différents fruits extraites de Harker et al. (Harker et al., 1997b)

b. Facteurs influençant les propriétés mécaniques

Les propriétés mécaniques du fruit sont fonction de différents paramètres structuraux. Les principaux sont la pression de turgescence, la rigidité des parois cellulaires et la cohésion de la lamelle moyenne entre les parois (Jackman and Stanley, 1995). L'étude des propriétés mécaniques du parenchyme de la pomme a montré que les tissus vasculaires ont une influence négligeable sur la mesure (Harker et al., 1997b). Entre les cellules, la contribution des propriétés mécaniques de la lamelle moyenne peut aussi être considérée comme négligeable (Harker et al., 1997a): elle transmet les cisaillements et supporte la compression ou la tension.

Dans la paroi, l'ensemble des constituants contribue aux propriétés viscoélastiques. A travers les modifications de la paroi lors de la maturation du fruit, la diffusion des solutés (sucres, ions, produits de dégradation de la paroi…) et l'augmentation de la

fluidité pariétale due à la rupture des polymères de la lamelle moyenne sont susceptibles de conduire à une modification des propriétés visco-élastiques. Différents facteurs interviennent dans la réponse élastique du tissu (Martinez et al., 2007) : si elle est principalement due à la paroi, la présence d'air intercellulaire et la pression de turgescence ont aussi un effet non négligeable sur cette dernière.

D'autres auteurs ont aussi cherché le lien entre la distribution de taille des cellules et la résistance du tissu. Une plus grande proportion de petites cellules augmenterait la résistance globale du tissu (plus grandes valeurs de force de compression) mais réduirait la résistance au niveau microscopique (les seuils de rupture sont plus bas) (Konstankiewicz and Zdunek, 2001). Cependant, les déformations cellulaires ne représentent qu'une partie de la déformation totale du tissu. Les espaces intercellulaires, et en particulier leur structure, ont aussi un impact important sur les propriétés mécaniques du tissu (Ting et al., 2013) : pour des microporosités comparables chez Fuji et Golden Delicious (29.3% et 29.8%, respectivement), la force de rupture (mesurée par pénétrométrie) varie de 28.4N pour Fuji à 14.2N pour Golden Delicious. Cette variation a été attribuée au fait que Fuji possède une multitude de petits espaces intercellulaires alors que Golden Delicious possède des grands espaces en moins grand nombre.

L'eau est un facteur important puisqu'elle influe sur les propriétés mécaniques du fruit, notamment par le biais de la pression de turgescence. La baisse de cette pression et la dégradation de la matrice pectique expliqueraient 25 à 30% du ramollissement du tissu et la baisse du poids moléculaire moyen des hémicelluloses expliquerait 10 à 15% supplémentaires (Jackman and Stanley, 1995). L'augmentation ou la diminution de la pression de turgescence conduit à un module d'élasticité (mesuré par compression et tension) accru ou diminué dans la pomme (Oey et al., 2007). Le test en compression est peu influencé par la pression de turgescence mais plutôt par la structure de la paroi et il en va de même pour le test en extension. Cependant la pression de turgescence agit sur le seuil de rupture des tissus (Cybulska et al., 2011), supposément par le fait qu'une pression plus importante induit une tension plus importante au niveau de la paroi, qui augmente encore quand le tissu est compressé, jusqu'à rupture (Konstankiewicz and Zdunek, 2001).

c. *La période de stockage*

Durant cette période, le fruit est sujet à un processus de ramollissement qui se traduit par une modification des propriétés mécaniques. Ce ramollissement se produit, pour une évolution classique à température ambiante, en trois phases (Johnston et al., 2002) (Figure 1-8). La première phase correspond à la période au cours de laquelle le ramollissement est faible, suivie d'une autre où il est plus rapide et enfin d'une dernière durant laquelle il se stabilise et redevient faible.

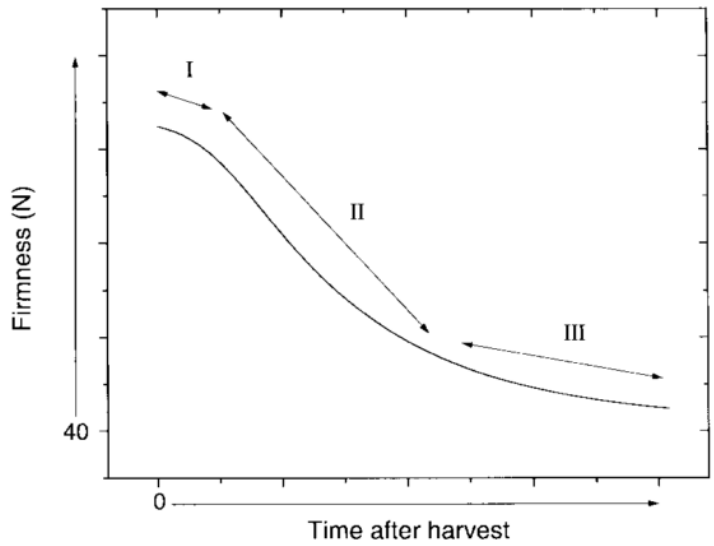

Figure 1-8 : Les trois phases du ramollissement du fruit durant un stockage au froid, graphe extrait de Johnston et al. (Johnston et al., 2002)

Cette cinétique est affectée par la date de récolte ainsi que par les conditions de conservation.

Au niveau structural, les pectines et hémicelluloses de la paroi sont toutes deux affectées par le stockage. Pour les hémicelluloses, plusieurs enzymes modifiant leur structure et plusieurs protéines ont une activité augmentée ou réduite. Par exemple, des glycosidases, la xyloglucane-endotransglycosylase et des expansines ont des activités modifiées qui changent la structure de la paroi cellulaire (Carpita, 2000; Johnston, 2001). Au niveau des pectines, les modifications durant le stockage mettent en évidence une déméthylesterification, une dépolymérisation et une solubilisation (De Vries et al., 1984). Chez la pomme, la dépolymérisation de la pectine est plutôt lente (Yoshioka et al.,

1992), elle s'initie à maturité, après récolte, et a été corrélée avec le ramollissement du tissu. Une augmentation de la quantité de pectines solubles et une décroissance des teneurs en arabinose et en galactose, notamment en chaîne latérale des domaines rhamnogalacturonane I des pectines, ont été reliées à des pertes d'adhésion cellulaires et au ramollissement du fruit (Gwanpua et al., 2014; Knee, 1973; Pena and Carpita, 2004; Yoshioka et al., 1992). Par ailleurs, l'étude *in vitro* de l'évolution de la texture de plusieurs fruits a montré que l'apparition d'une texture fondante et souple est liée à un phénomène de gonflement de la paroi (swelling) (Redgwell et al., 1997). Ce phénomène a été montré en microscopie et s'accompagne d'un afflux d'eau vers la paroi. L'ensemble de ces résultats indique que le ramollissement du tissu ferait intervenir une modification des parois, notamment au niveau des pectines qui pourrait mener à leur hydratation et participerait à la perte d'adhésion cellulaire.

Lors de la perte d'adhésion, les cellules se séparent et deviennent plus sphériques, les espaces intercellulaires augmentent (Brummell, 2006; De Smedt et al., 1998). On peut l'associer à une baisse de la pression de turgescence (Harker and Sutherland, 1993; Tong et al., 1999) probablement due à l'accumulation de soluté osmotique dans l'apoplaste et à la perte d'eau par le fruit. La perte d'eau du tissu du fruit est à rapprocher du stockage : durant ce dernier, la pomme perd de l'eau par transpiration et évaporation (Wu and Guo, 2010). La paroi devient plus relâchée et plus hydratée, elle est moins rigide et le fruit moins ferme. Un objectif pour prolonger la qualité de la pomme est de retarder la deuxième phase de la décroissance de la fermeté (Figure 1-8, Johnston et al., 2002).

Parmi tous les paramètres influençant la texture et les propriétés mécaniques que nous avons vus, beaucoup sont directement liés à l'hydratation de compartiments cellulaires, à la distribution de taille des cellules ou encore à la porosité du tissu. Ces facteurs sont importants pour le signal RMN/IRM où l'on étudie l'eau contenue dans l'échantillon (Hills, 2006).

II. RMN BAS CHAMP, IRM

La Résonance Magnétique Nucléaire (RMN) a été découverte en 1938 par Isidor Isaac Rabi et a depuis entrainé le développement des techniques de mesure et d'imagerie que sont la spectroscopie RMN, la relaxométrie RMN et l'IRM (Imagerie par Résonance Magnétique). Ces différentes techniques permettent l'étude de matériel biologique depuis l'échelle macroscopique jusqu'à l'échelle atomique avec des applications allant de la détection de tissus biologiques malades à l'analyse du repliement et de la séquence d'une protéine.

En biologie, la relaxométrie RMN se focalise majoritairement sur le signal des protons (hydrogènes) de l'eau et des lipides, qui sont prédominants. La RMN permet d'étudier l'eau dans des échantillons hétérogènes de manière non-invasive et non-destructive et donne accès à des paramètres dynamiques en lien avec la structure du milieu. Il a été montré que les événements cellulaires sont liés à l'état de l'eau associée et par conséquent l'étude de l'eau par la RMN de ses protons nous renseigne sur l'état physiologique du tissu (Ishida et al., 2000). La RMN offre donc un moyen efficace d'explorer la structure interne des tissus ; l'extension de cette technique à l'imagerie (IRM) avec P.C. Lauterbur et P. Mansfield se partageant le prix Nobel de médecine en 2003 offre en outre la possibilité de cartographier dans l'espace des signaux RMN.

Les applications, généralement connues pour le domaine médical, présentent aussi un grand intérêt dans l'agroalimentaire.

1) Théorie

La Résonance Magnétique Nucléaire est une technique qui, comme son nom l'indique, utilise des champs magnétiques afin de faire entrer en résonance des noyaux. Cette résonance produit un signal mesurable.

Les noyaux sont composés de neutrons et de protons qui, par un mouvement de rotation, peuvent induire un moment cinétique appelé Spin, aligné sur leur axe de rotation ainsi qu'un moment magnétique colinéaire au Spin. Les noyaux de spin 1/2 possèdent un moment magnétique résultant non nul. Soumis à un champ magnétique B_0

ils vont s'orienter parallèlement ou antiparallèlement à ce champ et entamer un mouvement de précession (dû au fait qu'ils possèdent aussi un moment cinétique angulaire de Spin). L'angle de précession dépend de la direction initiale de l'axe de polarisation du Spin. La fréquence de rotation ω_0 est la *fréquence de Larmor*, donnée sous sa forme angulaire :

$$\omega_0 = -\gamma B_0$$

où γ est le rapport gyromagnétique. L'aimantation résultant d'un ensemble de spins peut être basculée de différents angles par rapport à B_0 grâce à une impulsion de radiofréquence B_1 appliquée à la fréquence de Larmor des protons. Le signal RMN est la mesure de la précession d'une aimantation M_{xy} autour du champ magnétique principal B_0 arbitrairement associé à l'axe z (Torrey, 1956)(Figure 1-9). L'impulsion B_1 permet de basculer l'aimantation M_z sur un plan xy pour une évolution cohérente avec une phase définie nommée φ. Une fois l'impulsion transmise, les noyaux sont dans un état instable et vont relaxer vers leur position d'équilibre, d'une part par échanges d'énergie avec le réservoir environnant, c'est la relaxation spin-réseau ou longitudinale, et d'autre part par une perte de cohérence de phase, c'est la relaxation spin-spin ou transversale. Pour une impulsion de 90° (Figure 1-9), les spins retournent à l'équilibre avec une fréquence de rotation ω_0 telle que définie ci-dessus. Le retour à l'équilibre est caractérisé par deux temps, l'un caractérisant le retour à l'équilibre dans l'axe du champ magnétique z, c'est le temps de relaxation longitudinale (T_1), et l'autre dans le plan perpendiculaire à cet axe, c'est le temps de relaxation transversale (T_2).

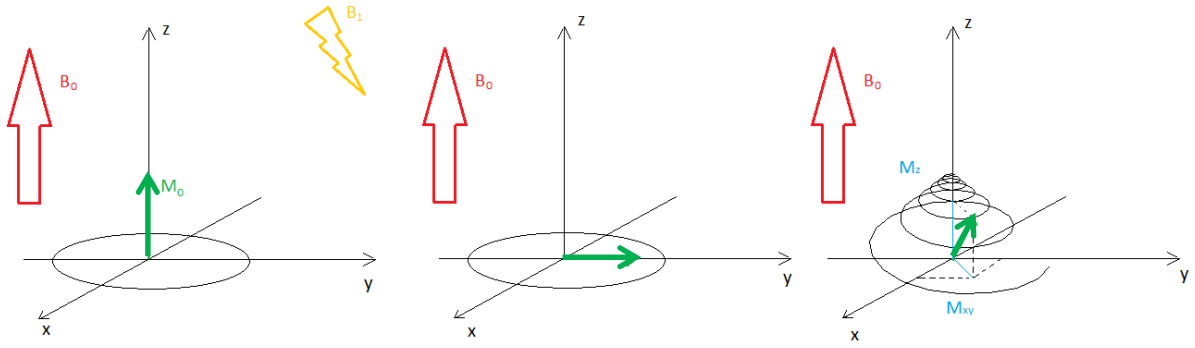

Figure 1-9 : Evolution de l'aimantation M_0 d'un spin sous l'effet d'un champ magnétique B_0 et d'une impulsion RF B_1 présentant le phénomène de relaxation

Les temps de relaxation (respectivement T_1 et T_2) sont caractéristiques de l'environnement des noyaux.

Pour un ensemble de spins on a donc deux équations, suivant l'axe du champ (composante M_z) et suivant le plan perpendiculaire (composante M_{xy}) caractérisant la relaxation :

$$\begin{cases} \frac{dM_z}{dt} = -(M_z - M_0)/T_1 \\ \frac{dM_{x,y}}{dt} = -M_{x,y}/T_2 \end{cases}$$

Avec pour solutions, pour un angle de bascule de 90° de l'aimantation,

$$\begin{cases} M_z(t) = M_z(0) \times (1 - e^{\frac{-t}{T_1}}) \\ M_{x,y}(t) = M_{x,y}(0) e^{\frac{-t}{T_2}} \end{cases}$$

La RMN à haut champ permet de différencier les noyaux en fonction de leur environnement chimique proche : chaque noyau est soumis au champ magnétique extérieur B_0 mais aussi à des champs locaux. L'impact de ces champs locaux sur la fréquence de résonance du noyau est appelé déplacement chimique. Le signal induit par la précession du moment magnétique est détecté par une antenne suivant l'une des directions du plan. Ce signal est constitué d'une sinusoïde décroissante comportant plusieurs fréquences caractéristiques des déplacements chimiques. L'étude des composantes fréquentielles est la spectrométrie RMN (sur la Figure 1-10, les fréquences contenues dans la sinusoïde amortie (en noir)) alors que la relaxométrie va s'intéresser à la courbe « enveloppe » de la décroissance du signal (intensité et temps caractéristique, sur la Figure 1-10, courbe enveloppe en violet).

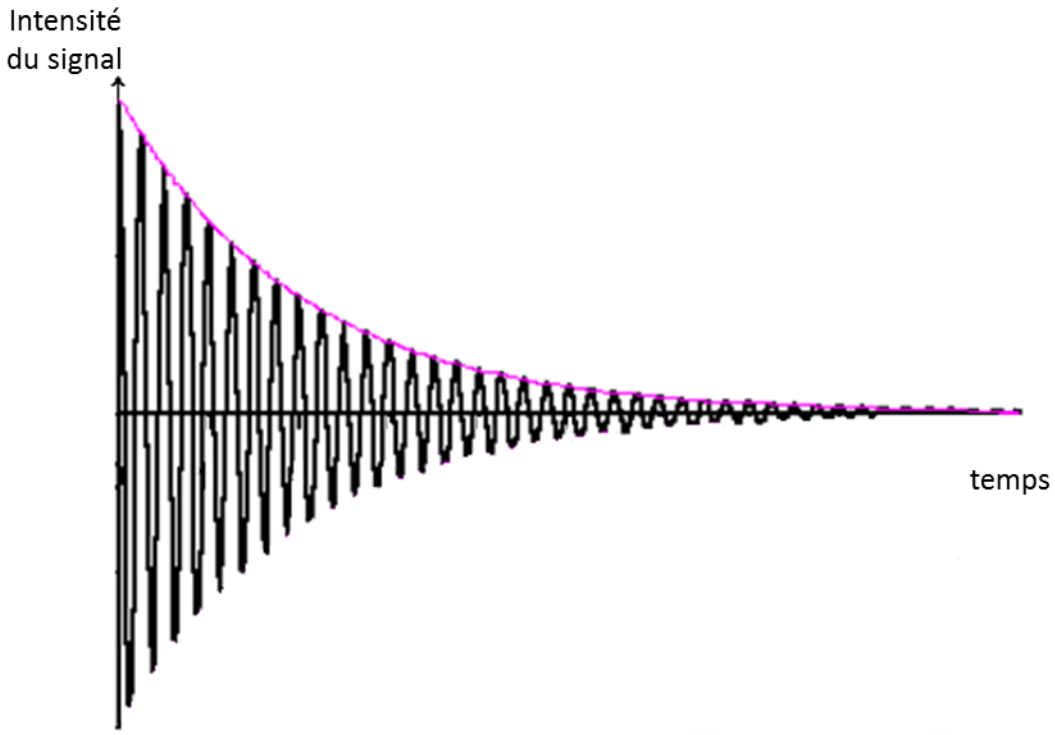

Figure 1-10 : Signal d'induction libre (Free Induction Decay ou FID)

2) Méthodologie

a. Mesures RMN

Plusieurs paramètres influencent le signal de relaxation RMN : en premier lieu la quantité des noyaux (reflétée par l'intensité du signal au temps zéro de bascule de l'aimantation), l'environnement des noyaux (reflété par les temps de relaxation T_1 et T_2), mais aussi les inhomogénéités du champ, les déplacements chimiques et la diffusion des molécules. Aussi, il est important de développer des séquences spécifiques permettant l'accès à un signal indépendant de certaines variables.

Pour la mesure des temps de relaxation, la séquence de base est la séquence écho de spin constituée d'une impulsion $\frac{\pi}{2}$ (cf Figure 1-9) suivie, après un temps τ, d'une impulsion π dans le plan qui va permettre de refocaliser l'angle de phase dû aux déplacements chimiques et à la dispersion en fréquence provoquée par les inhomogénéités du champ magnétique B_0. Les spins des noyaux sont donc à nouveau en

phase après une durée supplémentaire τ, et on obtient un écho à un temps 2τ après la première impulsion. La mesure de l'intensité des échos est ensuite répétée à différents temps et permet d'échantillonner la courbe de décroissance pondérée en T_2, affranchie des déplacements chimiques et inhomogénéités du champ. Toutefois, au fur et à mesure que le délai τ est augmenté, les effets des inhomogénéités ne sont plus négligeables en raison du déplacement par diffusion des molécules. Aussi, plutôt que de répéter la séquence avec des τ variables, Carr et Purcell ont proposé une séquence avec plusieurs impulsions π afin d'échantillonner la courbe de décroissance en une seule excitation (Figure 1-11). Cette séquence permet de limiter les biais dus à la diffusion des molécules dans un champ magnétique inhomogène car le délai τ reste petit et constant et permet donc d'obtenir une meilleure estimation du T_2. Afin d'améliorer le rapport signal sur bruit, le signal peut être moyenné en répétant les séquences après un temps de délai RD (Recovery Delay) permettant le retour de l'aimantation à l'équilibre.

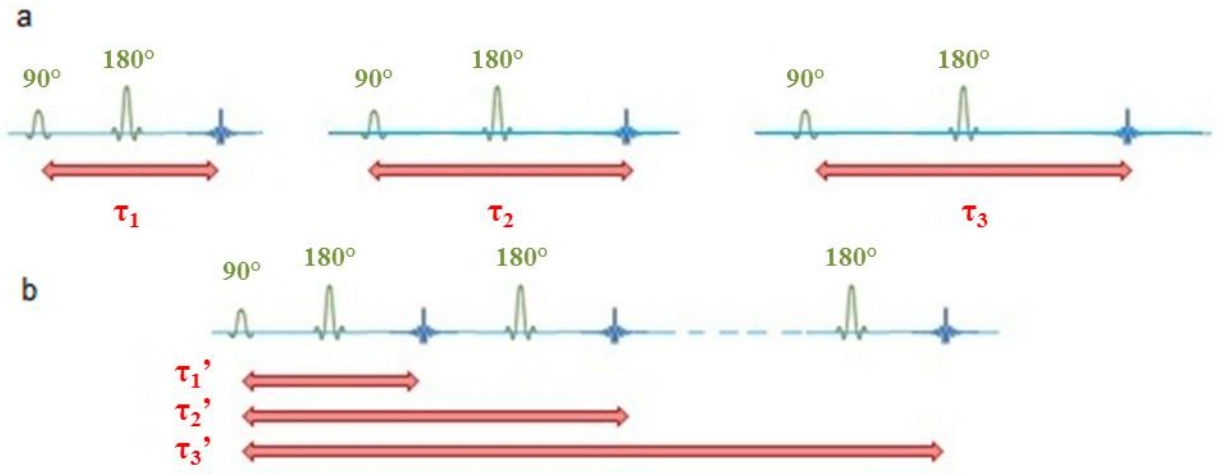

Figure 1-11 : Séquences écho de spin (a) et multi-écho de spin (b) pour trois temps d'échos (τ_1, τ_2 et τ_3). Les impulsions et leurs angles sont indiqués en vert et les échos en bleu.

Il existe un large panel de séquences RMN pour la mesure des temps de relaxation en particulier dans la mesure des T_1 (Callaghan, 1991). Ces séquences ne seront pas abordées dans le cadre de ce travail.

b. *Mesures IRM*

L'IRM offre la possibilité supplémentaire de coder spatialement le signal RMN. On obtient alors une résolution spatiale qui était jusqu'alors inaccessible par la RMN. Cependant, cette technique entraine aussi une baisse de la résolution temporelle de l'échantillonnage du signal : les contraintes de séquence rendent compliqué l'accès à des temps d'écho aussi courts qu'en RMN. Le temps d'écho d'une CPMG en RMN est de l'ordre de 0,1 ms alors qu'en IRM le temps d'écho d'une séquence écho de spin est de plusieurs millisecondes. La courbe de décroissance présente donc moins de points et le couplage des deux techniques présente un intérêt (Mariette, 2004). Le premier usage de l'IRM est l'imagerie médicale puisque l'obtention d'images contrastées en temps de relaxation permet une différenciation des tissus et en cas de pathologies de détecter des tissus endommagés comme dans le cas du tissu tumoral (Dortch et al., 2009). Mais cette technique permet également des approches quantitatives telles que les mesures des temps de relaxation ou de la porosité dont les applications sont nombreuses.

Une première partie du codage spatial consiste à sélectionner une coupe au sein de l'échantillon. Pour ce faire, on applique un gradient de sélection de coupe (GSC, ici en direction z, direction du champ magnétique principal, cf Figure 1-9) qui s'additionne à B_0 au moment de la première impulsion. La relation de Larmor devient alors $\nu_0 = \gamma \frac{B_0+GSC(z)}{2\pi}$ si z est l'axe parallèle au champ, avec la fréquence de Larmor $\nu_0 = \frac{\omega_0}{2\pi}$. L'épaisseur de coupe est déterminée par la largeur de la bande passante de l'impulsion et l'amplitude du GSC. Plus l'amplitude du GSC est grande, plus la coupe est fine ; et parallèlement plus l'impulsion est sélective (bande passante étroite), plus la coupe est fine.

Dans un second temps on réalise un codage de phase dans la direction perpendiculaire à l'axe de lecture qui se trouve suivant l'axe des x (cf. Figure 1-9). Pour ce faire on applique un gradient d'une courte durée qui va accélérer la vitesse de précession de manière variable suivant la position dans le gradient. A l'arrêt du gradient, la vitesse revient à sa valeur initiale et les spins sont plus ou moins déphasés suivant leur position. L'obtention d'une image complète nécessite les données avec plusieurs valeurs de la phase, aussi la séquence est répétée plusieurs fois avec une incrémentation de l'amplitude du gradient (échelle de gradient).

Enfin, on réalise un dernier codage suivant le troisième axe, cette fois encore en fréquence. Ce codage est réalisé au moment de l'acquisition du signal et le gradient appliqué est appelé gradient de lecture. Comme le gradient de sélection de coupe, il modifie la fréquence de rotation des spins en fonction de leur position, cette fois suivant le troisième axe et, puisqu'il est appliqué durant l'acquisition du signal, la fréquence de rotation est mesurée pour chaque élément de volume.

Les données sont stockées dans une matrice et une transformée de Fourier inverse 2D permet de reconstruire l'image. Il est possible d'obtenir des images tridimensionnelles en réalisant un codage de phase dans la troisième dimension de l'espace. L'utilisation de différentes séquences permet de pondérer l'image suivant différents paramètres tout comme en RMN.

Les notations sont différentes en IRM et en RMN. La Figure 1-12 met en exergue les différences : le temps τ en RMN correspond en IRM à $\frac{TE}{2}$, la répétition des séquences se fait après un délai de récupération RD en RMN appelé TR en IRM.

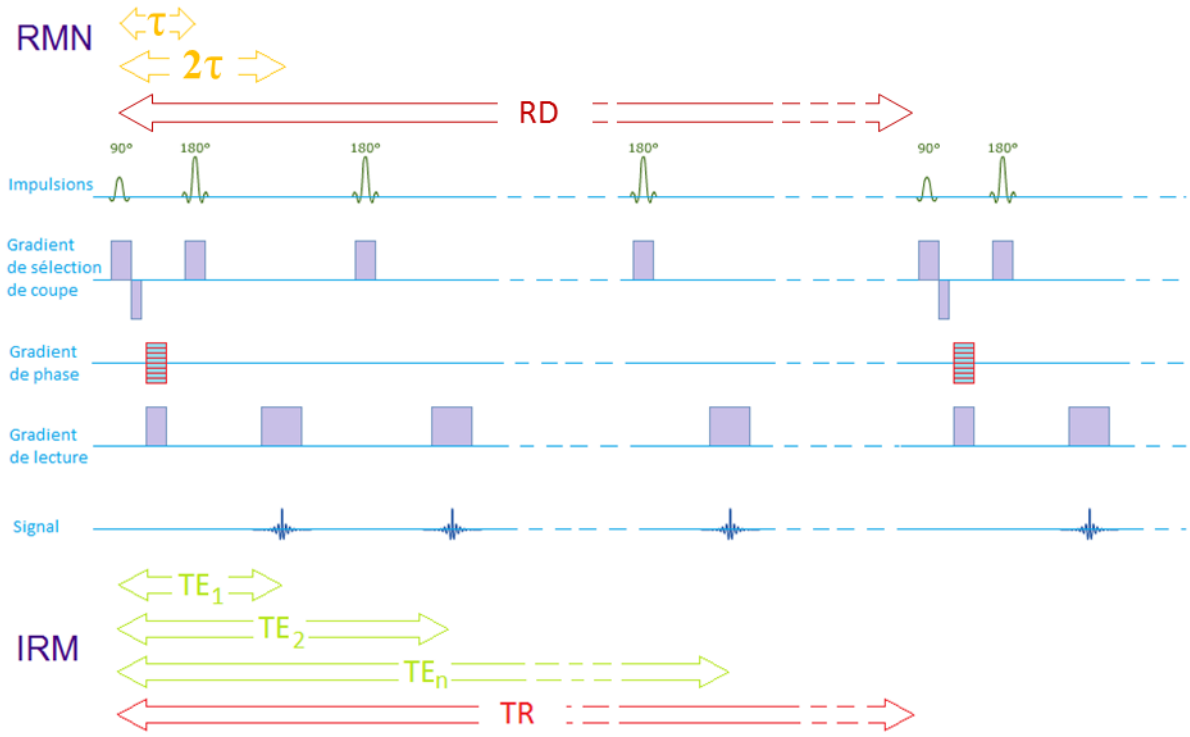

Figure 1-12 : Chronogramme d'une séquence multi-écho de spin, notation RMN (τ, RD) et IRM (TE, TR) pour comparaison.

Une séquence couramment utilisée est la séquence en écho de gradient. Comme pour l'écho de spin, on cherche à refocaliser le signal pour produire un écho. Pour ce faire, un gradient de lecture est imposé durant une durée $\frac{TE}{2}$ puis inversé. On observe alors un écho après un temps TE. Les inhomogénéités de champ ne sont pas compensées avec cette séquence ; le temps de relaxation spin-spin caractéristique obtenu par cette séquence est pour cette raison appelé T_2* et non T_2.

Les séquences écho de spin et écho de gradient peuvent être l'une comme l'autre utilisées afin de créer des échos successifs : dans le cas de l'écho de spin, l'impulsion π est répétée ; pour l'écho de gradient ce sont les gradients de lecture positifs et négatifs qui sont répétés. Ces méthodes permettent un échantillonnage de plusieurs échos avec une seule excitation (durant un même temps TR) avec des délais inter-écho plus courts minimisant les effets dus à la diffusion des molécules étudiés dans le milieu lors de l'acquisition des données (cf. ci-dessus).

c. Inhomogénéités de champ magnétique et mesures de temps de relaxation

Les séquences que nous venons de voir permettent la mesure des temps de relaxation. Ces temps de relaxation sont influencés par les inhomogénéités de champ. En effet, la présence d'interfaces entre des milieux de susceptibilité magnétique différente dans l'échantillon induit des inhomogénéités de champ locales qui vont déphaser les spins. La surface de l'interface entre les milieux et la géométrie de cette surface sont à l'origine des homogénéités de champ. L'effet de ces inhomogénéités sur la mesure dépend de la séquence, du temps d'écho, et du champ magnétique de l'aimant. On peut classer ces inhomogénéités de champ en fonction de leur taille : macroscopiques, mésoscopiques et microscopiques. Les inhomogénéités macroscopiques proviennent d'imperfections de l'aimant ou de larges inclusions supérieures à la taille du voxel et déforment localement le champ (De Guio et al., 2008). A titre d'exemple, les inhomogénéités de champ créées par un cylindre dans un plan perpendiculaire avec un champ magnétique sont présentées dans la Figure 1-13A (De Guio, 2008).

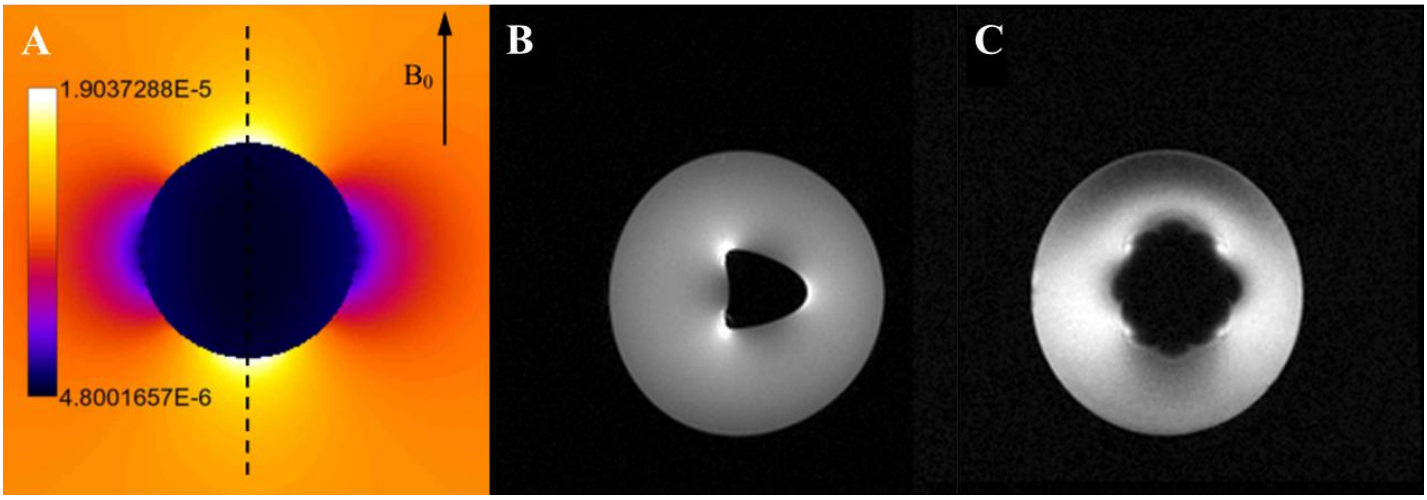

Figure 1-13 : (A) Inhomogénéités de champ induites par un cylindre rempli d'air et entouré d'eau (image extraite de (De Guio, 2008)) et images (B) écho de spin et (C) écho de gradient à 3T d'un cylindre de 12 cm de diamètre rempli d'eau en présence d'un cylindre coaxial de 3,5 cm de diamètre rempli d'air (images extraites de (Bakker and de Roos, 2006))

Ces inclusions induisent une perte de signal en écho de gradient par un déphasage intra-voxel et des distorsions géométriques en écho de spin et en écho de gradient comme illustré sur la Figure 1-13B et C).

Les inclusions mésoscopiques, i.e. dont la taille est plus grande que la longueur caractéristique de diffusion et plus petite que le voxel, vont influencer $T_2^{\#}$ la partie réversible du T_2* lors d'une mesure en écho de gradient (Fernandez-Seara and Wehrli, 2000; Yablonskiy, 1998) (le temps de relaxation transversale en écho de gradient s'écrit communément $\frac{1}{T_2^*} = \frac{1}{T_2} + \frac{1}{T_2^{\#}}$) .

Enfin, les inclusions microscopiques induisent des inhomogénéités de champ aux échelles atomiques et moléculaires. Ces inhomogénéités sont responsables d'une décroissance du signal irréversible caractérisée par le temps de relaxation T_2.

L'influence des effets de susceptibilité magnétique sur le signal de relaxation T_2 et T_2* est fortement dépendante du champ magnétique. La diminution du T_2* observée lorsque le champ augmente s'explique par l'augmentation du déphasage intravoxel avec l'intensité du champ magnétique principal. L'augmentation du champ entraine aussi une augmentation des inhomogénéités de champ local induites par la présence de deux milieux de susceptibilités magnétiques différentes. Par suite, le déphasage dynamique

dû à la diffusion augmente avec le champ et fait diminuer le temps de relaxation T_2 (de Graaf et al., 2006).

d. Modélisation des inhomogénéités de champ

Pour modéliser les effets dûs aux inhomogénéités, Yablonskyi et Haacke (Yablonskiy, 1998; Yablonskiy and Haacke, 1994) développent la théorie du « static dephasing regime » : dans un échantillon où des inclusions induisent des inhomogénéités du champ statique B_0, il existe un temps caractéristique t_c défini par la géométrie des inclusions et la différence des susceptibilités magnétiques qui, s'il est inférieur à un temps caractéristique de diffusion (fonction du coefficient de diffusion des molécules et de la taille des inclusions) permet d'ignorer les effets de la diffusion sur le signal. Le signal de relaxation est alors une fonction linéaire de la fraction volumique d'inclusions, du champ magnétique B_0, de la différence de susceptibilités magnétiques entre les deux milieux, et de la diffusion.

Si les inclusions d'air sont mésoscopiques, en se plaçant dans le « static dephasing regime » et en considérant des inclusions sphériques, on peut établir un lien entre le signal de relaxation et la fraction volumique des inclusions dans le tissu (Donker et al., 1996; Musse et al., 2010b):

$$R_2^{\#} = \frac{2\pi}{9\sqrt{3}} \varepsilon \gamma \Delta\chi B_0$$

où $R_2^{\#} = \frac{1}{T_2^*} - \frac{1}{T_2}$, ε est la porosité, γ est le rapport gyromagnétique du proton et $\Delta\chi$ la différence de susceptibilité entre les deux milieux.

Pour que l'hypothèse du « static dephasing regime » soit vérifiée, le temps caractéristique $t_c = 9\sqrt{3}/(2\pi\gamma\Delta\chi B_0)$ doit être inférieur au temps caractéristique de la diffusion $t_D = R_0^2/D$ où D est le coefficient de diffusion et R_0 le rayon moyen des inclusions. Cette contrainte se traduit sur la géométrie des bulles d'air $R_0^2 \gg 9\sqrt{3}D/(2\pi\gamma\Delta\chi B_0)$ (de l'ordre du micromètre pour des conditions expérimentales de cette thèse). Si la contrainte est respectée, la microporosité peut s'écrire :

$$\varepsilon = \frac{9\sqrt{3}R_2^{\#}}{2\pi\gamma\Delta\chi B_0}$$

Elle peut alors être calculée à partir de mesures de T_2 et de T_2* (séquences spin-écho et gradient-écho, respectivement).

3) Mécanismes de relaxation

De nombreux facteurs interviennent dans le signal RMN de l'eau (Hills et al., 1990; Van As, 2007). C'est la mobilité des molécules, dépendant de leur environnement direct, qui est à l'origine des temps de relaxation. Dans un milieu composé uniquement d'eau, les molécules d'eau interagissent entre elles chimiquement, par échange de protons, et par interactions dipolaires, mais elles présentent toutes le même environnement et donc les mêmes temps de relaxation (T_1 et T_2). Si l'on diminue la mobilité des molécules et/ou si l'on change les interactions, les temps de relaxation s'en trouvent modifiés. Par exemple, si l'on s'intéresse à de la glace pure, les temps de relaxation T_2 sont inférieurs (une dizaine de microseconde) à ceux de l'eau pure (quelques secondes). L'addition d'un soluté dans l'eau diminue la mobilité des molécules d'eau et entraine des interactions dipolaires et chimiques entre eau et soluté, provoquant une baisse des temps de relaxation (Hills, 1992a; Snaar, 2002). Ainsi, plus la teneur en soluté sera élevée, plus le temps de relaxation de l'eau sera faible (Hills, 1992b). Cependant, les différentes dynamiques d'échange ayant lieu au sein du mélange entrainent un signal plus complexe. Ce signal est décrit ci-après.

Dans un mélange binaire avec une molécule non aqueuse (solutés, macromolécules etc), on distingue quatre populations de protons que sont ceux de l'eau dite « libre », ceux de l'eau d'hydratation des solutés, les protons échangeables des solutés et les protons non échangeables du soluté. Les protons non-échangeables des solutés sont les protons de la chaine carbonée (CH, CH_2, CH_3) tandis que les autres protons tels que les hydroxyles, par exemple, sont labiles et donc considérés comme étant échangeables avec les protons de l'eau. Les protons du soluté sont répartis entre deux environnements auxquels correspondent deux temps de relaxation $T_{2,\text{soluté éch}}$ et $T_{2,\text{soluté non éch}}$ pour les pools de protons échangeables et non échangeables respectivement. Pour l'eau, on a de

la même manière deux environnements ; une fraction d'eau qui ne subit pas d'interaction avec le soluté et dont le comportement RMN peut être assimilé à la relaxation de l'eau pure, et une fraction qui correspond à l'eau d'hydratation des solutés. Chacune de ces deux fractions est décrite par un temps de relaxation : $T_{2,eau}$ et $T_{2,eau\ hydr}$. Les protons échangeables et les protons de l'eau sont dans une dynamique d'échange qui conditionne les temps de relaxation mesurés. La description de l'échange suivante se base sur le *modèle à deux sites* de Zimmerman et Brittin (Zimmerman and Brittin, 1957). Deux types d'échanges existent : les échanges chimiques entre eau et soluté et les échanges diffusionnels entre l'eau libre et l'eau d'hydratation. Si toutes les dynamiques d'échange sont lentes devant les temps de relaxation (les temps caractéristiques d'échange chimique et de diffusion sont faibles devant les temps de relaxation), la décroissance a un comportement quadri-exponentiel. Tous les pools de protons ont des relaxations différentes. Le signal de relaxation transversale s'écrit alors :

$$M(t) = M(0)\left(P_{non-ech}e^{-\frac{t}{T_{2,soluté\ non\ éch}}} + P_{ech}e^{-\frac{t}{T_{2,soluté\ éch}}} + P_{eau-libre}e^{-\frac{t}{T_{2,eau}}} + P_{eau-hydr}e^{-\frac{t}{T_{2,eau\ hydr}}}\right)$$

Equation 1-1

où P_i représente les proportions de protons dans les différents pools.

Dans un deuxième cas, les échanges chimiques et diffusionnels peuvent être tous deux rapides. Les protons du soluté échangeables et ceux de l'eau (libre et d'hydratation) sont alors confondus à cause de la rapidité des échanges chimiques et diffusionnels et présentent un seul temps de relaxation. Le signal s'écrit :

$$M(t) = M(0)\left(P_{non-ech} \times e^{-\frac{t}{T_{2,soluté\ non\ éch}}} + \left(P_{eau-\text{libre}} + P_{eau-hydr} + P_{ech}\right)e^{-\frac{t}{T_{2m}}}\right),$$

$$avec\ \frac{1}{T_{2m}} = \frac{P_{eau-libre}}{T_{2,eau}} + \frac{P_{eau-hydr}}{T_{2,eau\ hydr}} + \frac{P_{ech}}{T_{2,soluté\ éch}}$$

Equation 1-2

Si maintenant les échanges diffusionnels sont lents et les échanges chimiques rapides, on distingue trois populations de protons. La première est celle des protons de l'eau qui sont 'éloignés' du soluté et ne peuvent donc pas interagir avec lui. La seconde

correspond aux protons de l'eau et du soluté en échange qui représentent une seule population puisque l'échange chimique est rapide. La dernière reste les protons non-échangeables du soluté. Le signal s'écrit alors :

$$M(t) = M(0)\left(P_{non-ech} \times e^{-\frac{t}{T_{2,soluté\ non\ éch}}} + \left(P_{eau-hydr} + P_{ech}\right)e^{-\frac{t}{T_{2n}}} + P_{eau-libre} \times e^{-\frac{t}{T_{2,eau}}}\right),$$

Equation 1-3

$$avec \quad \frac{1}{T_{2n}} = \frac{P_{eau-hydr}}{T_{2,eau\ hydr}} + \frac{P_{ech}}{T_{2,soluté\ éch}}$$

Modèle milieux poreux/compartimentation

Un milieu poreux est défini par la présence d'inclusions (pores) d'un milieu dans un autre milieu. Dans ce cas, à l'intérieur du pore, les molécules d'eau sont en échange diffusionnel rapide avec l'interface. La relaxation est alors influencée par la présence d'une interface entre les milieux (Mitra et al., 1993; Mitra et al., 1992) qui provoque une chute de l'aimantation caractérisée par un paramètre de relaxation de surface (noté ρ). Il en résulte une modification du temps de relaxation dans le pore qui s'écrit $\frac{1}{T_2} = \frac{1}{T_{2,eau\ libre}} + \rho\frac{S}{V}$ où $\frac{S}{V}$ est le quotient de la surface de restriction sur le volume du pore. Si l'on considère deux pores distincts à l'intérieur desquels les molécules d'eau sont en échange diffusionnel rapide, et entre lesquels il n'y a pas d'échange, le système est compartimenté et l'on obtient un signal de décroissance bi-exponentiel.

4) Relaxation dans les tissus végétaux

Les cellules végétales présentent une structure complexe qu'il est nécessaire de simplifier pour comprendre les mécanismes mis en jeu. Dans le cas de la pomme, la cellule est composée de trois principaux compartiments aqueux : la vacuole, comportant environ 80% de l'eau, le cytoplasme et la paroi (incluant l'eau extracellulaire). La vacuole est séparée du cytoplasme par le tonoplaste, et le cytoplasme est séparé de la

paroi/eau extracellulaire par le plasmalemme (Figure 1-3). L'ensemble de ces compartiments est en interaction de par la perméabilité des membranes et est à l'origine d'un signal multi-exponentiel complexe (Belton and Ratcliffe, 1985; Brownstein and Tarr, 1979). Une attribution simple a été faite dans laquelle les différents pools de protons, correspondants aux différentes composantes de la relaxation T_2 multi-exponentielle, sont attribués aux principaux compartiments cellulaires (Sibgatullin et al., 2007; Snaar and Van as, 1992) : la composante de T_2 plus élevé et de plus forte intensité correspond à la vacuole et les autres composantes sont attribuées au cytoplasme, à l'eau extracellulaire et à l'eau en interaction avec la paroi.

Conformément au modèle des milieux poreux (Mitra et al., 1993; Mitra et al., 1992), il a été démontré que la géométrie des tissus végétaux, et en particulier la taille des cellules, influence le temps de relaxation transversale (Brownstein and Tarr, 1979; Van der Weerd et al., 2001). Le modèle de relaxation T_2 en milieu poreux a été adapté par Van der Weerd et al. (Van der Weerd et al., 2001) aux cellules végétales. Il permet d'exprimer le temps de relaxation transversale mesuré de l'eau ($T_{2,obs}$) confinée dans la vacuole en fonction du T_2 de l'eau pure ($T_{2,bulk}$), des rayons de la vacuole suivant les directions spatiales (R_x, R_y, R_z) et d'une constante H appelée 'sink strengh' qui décrit le taux de perte d'aimantation au contact du tonoplaste :

$$\frac{1}{T_{2,obs}} = H\left(\frac{1}{R_x} + \frac{1}{R_Y} + \frac{1}{R_z}\right) + \frac{1}{T_{2,bulk}}$$

Équation 1-4

H s'exprime en $m.s^{-1}$ et dépend des échanges de molécules d'eau au travers de la membrane avec le compartiment adjacent de T_2 différents et de l'interaction directe avec la membrane qui accélère la relaxation. L'équation ci-dessus a pu être démontrée dans la tige du maïs et du millet grâce à l'importante variation de taille de cellules de ces végétaux, en supposant que le comportement mono-exponentiel de la relaxation reflétait celui de la vacuole.

5) Applications en biologie végétale

a. RMN

Plusieurs études réalisées par Relaxométrie RMN ont eu pour objet d'attribuer les pools de protons reflétés par la décroissance multi-exponentielle. En 1990, Hills et collaborateurs (Hills et al., 1990), étudient le signal RMN de la pomme à 100 MHz : en réhydratant un extrait de parois cellulaires, ils trouvent un temps de relaxation T_2 de 30 ms, indépendant du temps d'écho, expliqué par un échange chimique rapide entre les protons de l'eau et ceux des polysaccharides de la paroi. Parallèlement, la mesure sur le parenchyme du fruit (TE = 0.1 ms) donne un signal bi-exponentiel avec des T_2 d'environ 500 ms et 1000 ms, interprété comme provenant respectivement du cytoplasme et de la vacuole. Par la suite, Snaar et Van As (Snaar and Van as, 1992) étudient l'évolution du signal RMN (20 MHz) de la pomme en fonction de l'imprégnation d'un agent de contraste (Mn^{2+}) afin d'attribuer les composantes du signal et de vérifier le modèle d'interprétation. Un signal tri-exponentiel est obtenu: une composante de T_2 élevé à 1020 ms associée à une amplitude relative de 75.2%, une deuxième composante avec un T_2 intermédiaire de 190 ms et une amplitude relative de 16.4%, et enfin une troisième composante ayant un T_2 court, de 30 ms, associée à une amplitude relative de 8,4%. L'évolution des temps de relaxation et des amplitudes est alors suivie en fonction du temps d'imprégnation de l'agent de contraste (Figure 1-14).

L'agent de contraste diffuse d'abord dans le compartiment extracellulaire (triangles blancs) et le temps de relaxation diminue en conséquence (Figure 1-14A, premières heures), puis il diffuse dans le cytoplasme (triangles noirs) provoquant aussi une baisse du T_2 (Figure 1-14A, à partir d'1,5 heure). Enfin, il diffuse dans la vacuole (cercles) où il entraine une baisse du T_2 (Figure 1-14A, un peu avant 3 heures) et une baisse significative d'amplitude (Figure 1-14B). Cette baisse n'est malheureusement pas commentée et indiquerait un changement dans la répartition de l'eau au sein du tissu.

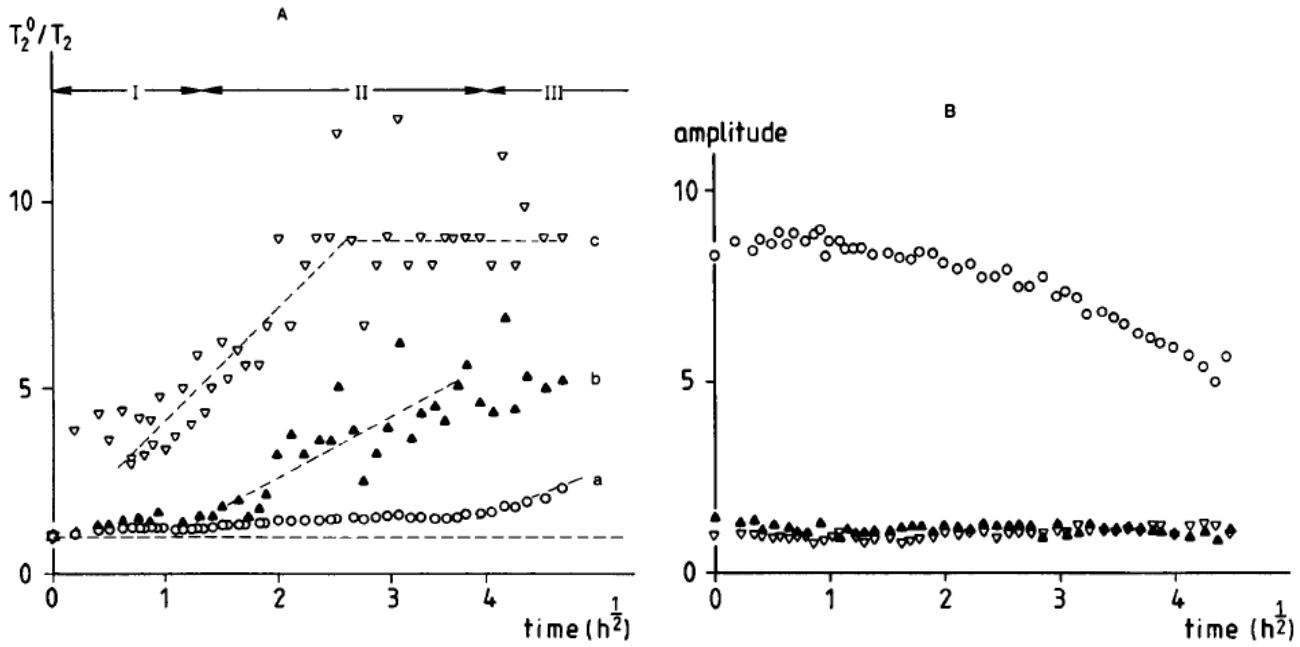

Figure 1-14, extraite de (Snaar and Van as, 1992) : Evolution des temps de relaxation normalisés (A) et des amplitudes correspondantes (B) en fonction de la pénétration de Mn^{2+} dans le tissu. La composante longue correspond aux cercles, la composante intermédiaire aux triangles noirs et la composante courte aux triangles blancs. Un spectromètre de 20 MHz a été utilisé.

Cette attribution du signal de la relaxation transversale dans la pomme est par la suite complétée par des études couplées de relaxation et diffusion. Sibgatullin et collaborateurs (Sibgatullin et al., 2007) montrent ainsi l'existence de quatre composantes dans le signal de relaxation (spectromètre de 30 MHz, TE=0.2 ms). Contrairement à Snaar et collaborateurs (Snaar and Van as, 1992), les auteurs distinguent l'eau de la paroi et l'eau extracellulaire. La plus longue est associée à la vacuole (1250 ms), les composantes intermédiaires sont associées à l'eau du cytoplasme et à l'eau extracellulaire (480 ms et 120 ms) et la composante courte est associée à la paroi (30 ms). Les mêmes auteurs réalisent des mesures de diffusion par DARTS qui permettent de résoudre 3 composantes pour lesquelles, pour des temps de diffusion courts, les restrictions des bords des compartiments ne sont pas ressenties. Pour la composante de T_2 long (1290 ms), le coefficient de diffusion intrinsèque a été estimé à 1.71×10^{-9} m^2/s, à 1.03×10^{-9} m^2/s pour la seconde composante (460 ms) et 0.94×10^{-9} m^2/s pour la troisième (76 ms). Aux temps de diffusion longs, deux composantes sont mesurées (les deux de T_2 plus court) et présentent le même

coefficient de 0.83×10^{-9} m^2/s. A partir de ces mesures, la taille des cellules ainsi que la perméabilité entre la vacuole d'une cellule et celle des cellules avoisinantes (les deux tonoplastes, plasmalemmes et parois) ont été estimées : le rayon moyen des cellules est de 86 µm et la perméabilité de la barrière totale entre les deux vacuoles de $2.9 \times 10^{-6}\ m.s^{-1}$, inférieure d'un ordre de grandeur à la perméabilité du tonoplaste mesurée dans une précédente étude ($2.44 \times 10^{-5}\ m.s^{-1}$) (Snaar and Van as, 1992).

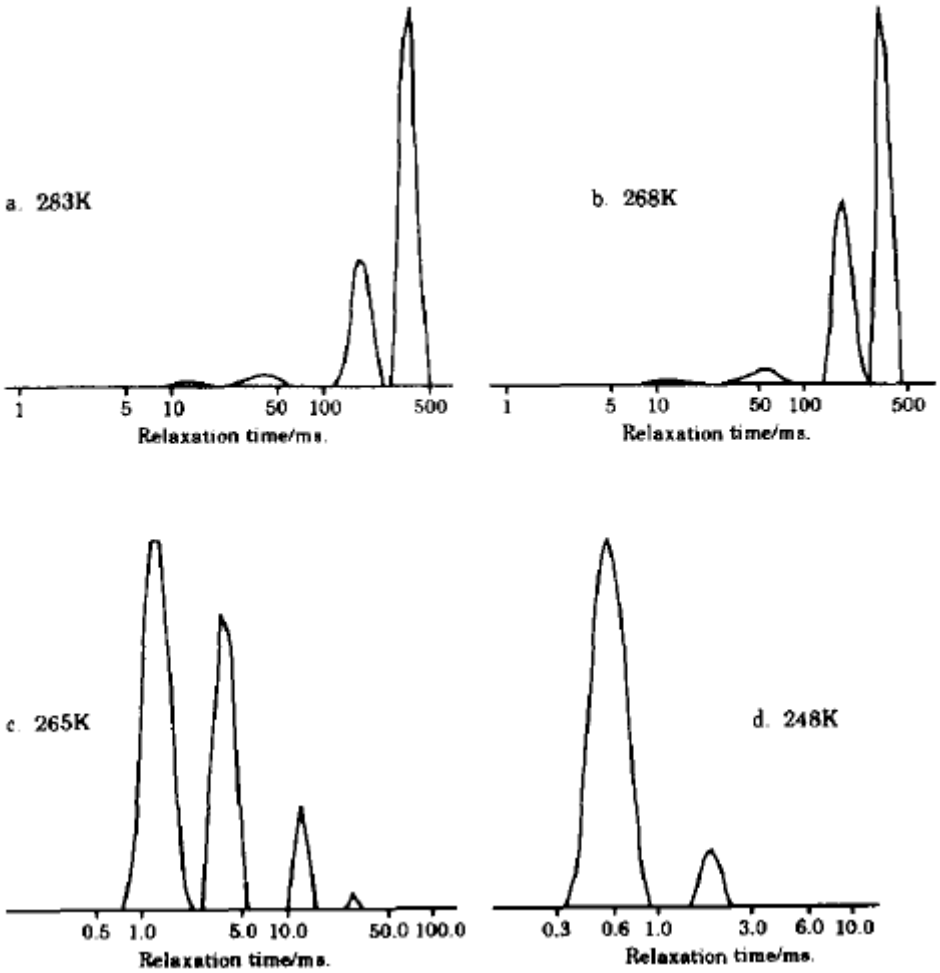

Figure 1-15, extraite de (Hills and Lefloch, 1994) avec un spectromètre de 100 MHz (TE=0.4 ms) : tracé des amplitudes en fonction des temps de relaxation pour des prélèvements de pomme de terre mesurés à différentes températures.

Une attribution similaire est aussi faite dans la pomme de terre par Hills et Le Floch (Hills and Lefloch, 1994) grâce à une congélation progressive (spectromètre de 100 MHz, TE=0.4 ms). En s'aidant des signaux de solutions de granules d'amidons soumises à

un processus de congélation, ils interprètent le spectre de congélation du tissu comme suit.

Le signal comporte quatre pics et la congélation permet d'aider à leur attribution (Figure 1-15). Comme précédemment, à 283 K, le compartiment de T_2 le plus élevé est attribué à la vacuole, le deuxième au cytoplasme (T_2 = 250 ms) et le troisième (T_2 = 50 ms) à la paroi. Le compartiment de T_2 le plus court est attribué aux granules d'amidon. Entre 283 K et 268 K, il n'y a que peu d'évolution du signal. A partir de 266 K, l'eau extracellulaire, celle du cytoplasme et celle des vacuoles gèle et un pic apparaît à 1 ms correspondant à l'eau non gelée associée aux macromolécules. Les pics restants sont attribués aux protons de l'eau dans les granules d'amidon et dans la paroi qui ne sont que partiellement gelées comme le signalent les pics aux alentours de 4 ms et 10 ms. Un refroidissement plus important à 248 K gèle l'eau dans la paroi et dans les granules, et seule une petite quantité d'eau non gelée reste avec un temps de relaxation de 2 ms. Cette étude a aussi permis de montrer l'effet de l'amidon sur le signal de relaxation : une composante supplémentaire est associée à l'eau contenue dans les granules.

L'amidon en solution induit aussi des changements de temps de relaxation : Raffo et collaborateurs (Raffo et al., 2005) montrent chez la banane une augmentation des T_2 multi-exponentiels associés aux trois compartiments (vacuole, cytoplasme, paroi) durant la dégradation de l'amidon dans le fruit (spectromètre de 20 MHz, TE=1 ms). Les auteurs montrent aussi que les effets de concentration en sucre sur les T_2 sont négligeables dans les conditions physiologiques en considérant une concentration de 20% en masse de glucose dans de l'eau : le temps de relaxation transversale T_2 mesuré décroit de 2 s (eau pure) à 1.9 s (Raffo et al., 2005). Cependant, une autre étude indique une baisse importante des temps de relaxation pour une solution eau/glucose : pour une concentration en masse similaire (23%), le temps de relaxation T_2 diminue jusque 893 ms (Desbois, 1992).

D'autres études ont été réalisées sur l'effet des hautes pressions et des variations de température chez l'oignon (Gonzalez et al., 2010) (afin de mimer différents processus de transformation), où les mesures du T_2 et de la diffusion reflètent les dégâts sur la membrane (spectromètre de 30.9 MHz, TE=0.5 ms). La Figure 1-16 présente la distribution des temps de relaxation et leur évolution en fonction de la température.

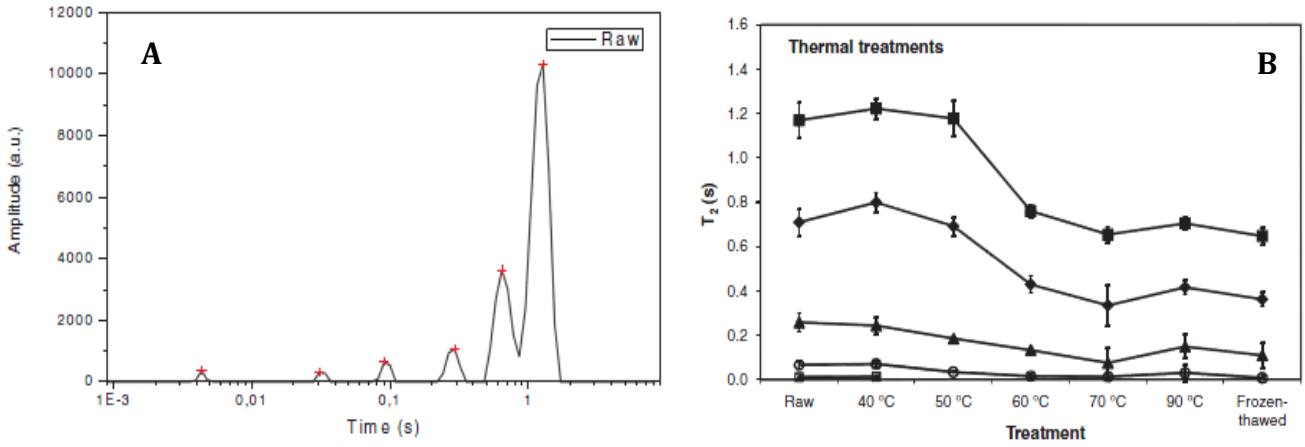

Figure 1-16, extraite de Gonzalez et al., 2010, spectromètre à 30.9 MHz, TE=0.5 ms: (A) distribution des T_2 mesurés chez l'oignon et (B) évolution des T2 en fonction des températures.

Le nombre relativement important de composantes vient du fait que le tissu de l'oignon est beaucoup plus hétérogène que le tissu de la pomme et la multiplicité des composantes reflète les différents types et tailles de cellules. Jusqu'à 70°C, les auteurs observent des comportements différenciés en fonction de la température suivant les composantes. Par exemple, la composante caractérisée par le plus faible temps de relaxation disparait quand la température augmente, la composante relaxant entre 10 et 100 ms a un temps de relaxation qui diminue, et les deux relaxant le plus lentement présentent un plateau suivi d'une diminution. Le tissu congelé-décongelé est pris en référence pour la perte de la compartimentation et la rupture cellulaire due à la formation de cristaux de glace. L'évolution constatée ici serait donc due à la perte d'intégrité cellulaire. Selon les auteurs cette rupture a probablement lieu à partir de 60 °C et l'on observe deux régimes différents en dessous et au-dessus de cette température. Toutefois, la diminution des T_2 avec la température à partir de 50°C n'est pas attendue et traduit plutôt un changement de structure des tissus. Deux modèles différents des temps de relaxation devraient alors s'appliquer de part et d'autre de cette zone de transition pour expliquer les modifications mesurées. Ces résultats sont confirmés par l'infiltration d'un agent de contraste dont la diffusion intracellulaire est plus rapide pour les cellules endommagées. Des résultats similaires ont été observés pour une étude RMN du blé (Maheswari et al., 1999), où jusque 35 °C un déclin des temps de relaxation est observé suivi d'une augmentation jusqu'à un maximum (pic)

marquant l'endommagement des cellules, à partir duquel les temps de relaxation décroissent à nouveau.

Par ailleurs, plusieurs études montrent des dépendances différentes des temps de relaxation en fonction des teneurs en eau : dans certain cas, la baisse de la teneur en eau n'affecte pas les temps de relaxation alors qu'elle les affecte de manière importante dans d'autres cas. Par séchage dans la tomate, une baisse de 5% de la teneur en eau n'altère pas les T_2, tandis que les amplitudes des composantes attribuées à la vacuole et au cytoplasme diminuent fortement et de façon proportionnelle à la perte en eau (Musse et al., 2010a). Dans la pomme, une baisse du T_2 de la composante principale associée à la vacuole est observée après une baisse de 10% de la teneur en eau (Hills and Remigereau, 1997). Dans d'autres cas, un séchage lent dans la pomme (Mariette et al., 1999) (spectromètre de 20 MHz, TE=5.6 ms), faisant passer la teneur en eau de 89% à 80%, entraine une chute de l'ensemble des temps de relaxation (la composante principale diminue de 1200 ms à 550 ms). Ces résultats indiquent qu'une baisse importante de la teneur en eau est nécessaire pour observer un impact sur les T_2 et que cet impact est fonction de la cinétique de séchage : une cinétique lente induirait une décroissance T_2 plus importante pour une même variation de teneur en eau. Des études sur produits présentant une variation naturelle de teneur en eau (sans séchage) ont montré qu'une variation de teneur en eau de 90% à 94% durant la sénescence foliaire correspond à une croissance T_2 de 103 ms à 448 ms (Musse et al., 2013) (spectromètre de 20 MHz, TE=0.2 ms) même si, dans ce cas précis, la variation de la taille de la vacuole interviendrait aussi. La relation teneur en eau/T_2 dépend aussi de la variété (Kaku, 1993) : Kaku et al. ont observé (spectromètre de 20 MHz) des valeurs de T_1 pour différentes espèces d'Azalea qui ne suivaient pas la même relation linéaire avec la teneur en eau. Enfin, une variation de teneur en eau de 5% durant le stockage du kiwi n'entraine pas de variations des T_1 et T_2 (Burdon and Clark, 2001). Les variations des T_2 en fonction de la teneur en eau dans des systèmes végétaux restent donc complexes à élucider.

Des mesures du coefficient de diffusion et des temps de relaxation ont aussi été réalisées dans des tomates de différentes maturités et différentes variétés (Duval et al., 2005) (spectromètre de 20 MHz, TE=0.8 ms). Une attribution similaire à celle de la pomme a été faite pour les trois composantes (vacuole, cytoplasme, paroi/eau

extracellulaire) et a montré une évolution du coefficient de diffusion intrinsèque de la paroi/eau extracellulaire mais pas des autres compartiments. L'étude du mûrissement de la tomate par RMN à 20 MHz (Musse et al., 2009) a aussi montré que le mûrissement s'accompagne d'une baisse des temps de relaxation (T_1 et T_2) dans la majorité des tissus et d'une redistribution des amplitudes des composantes qui a été attribuée à un changement de la répartition de l'eau dans les compartiments cellulaires.

Des mesures couplées des temps de relaxation T_2 et T_1, et des temps de relaxation et diffusion (DARTS) ont aussi été utilisées afin d'aider à l'attribution des compartiments (Marigheto et al., 2007). Les auteurs font aussi des spectres T_2-store-T_2 qui permettent d'aider à identifier les pics sur les spectres T_1-T_2 mais aussi de voir apparaître des pics d'échange entre deux compartiments pour des fréquences d'impulsion CPMG de l'ordre de la durée de l'échange. Une application (spectromètre de 23.4 MHz, TE=0.4 ms) a été réalisée dans l'étude du caractère farineux de la pomme (Marigheto et al., 2008). Cette étude confirme un comportement à quatre composantes et montre qu'il existe des différences de T_1 pour l'eau associée à la paroi entre les fruits farineux et non farineux (T_2 de 11 ms pour les fruits non affectés et affectés, T_1 de 71 ms pour les fruits non affectés et 222 ms pour les fruits farineux). Ces résultats en contredisent d'autres antérieurs, pour lesquels le temps de relaxation transversale associé à la principale composante du signal RMN diminuait quand la farinosité augmentait (Barreiro et al., 2002). L'apport des couplages T_2-T_2, T_2-D, T_1-T_2, etc. (Marigheto et al., 2008) n'a cependant pas permis une interprétation simple des temps de relaxation, les résultats ne permettant pas de conclure avec certitude à un lien direct entre la farinosité et le signal. Des mesures multi-exponentielles de fruits atteints de watercore et de brunissement ont aussi été réalisées sur fruit entiers (le fruit intact est introduit dans l'aimant). Elles montrent une augmentation des intensités attribuées au cytoplasme et à l'eau extracellulaire/paroi alors que celle de la vacuole baisse pour les fruits atteints de brunissement ou de watercore et brunissement combinés (Cho et al., 2008b). Cette variation des intensités est accompagnée d'une augmentation du temps de relaxation attribué à l'eau extracellulaire/paroi.

En général, les mesures RMN de plantes sont réalisées sur des prélèvements, empêchant de faire des suivis sur les mêmes échantillons. Cependant, des développements récents permettent des mesures *in vivo* avec des appareils portatifs

utilisables sur les plantes en extérieur (Capitani et al., 2009; Rokitta et al., 2000; Van as et al., 1994), avec néanmoins des limitations. En particulier, des contrôles de flux d'air et de température sont nécessaires mais compliqués à mettre en œuvre (Ratcliffe et al., 2001; Scheenen et al., 2000; Van der Toorn, 2000). De plus la présence des gradients de champ spécifiques à ces aimants entraine de fortes réductions des temps de relaxation ce qui complique les interprétations.

Les études RMN peuvent être complétées par l'IRM qui apporte une dimension spatiale et permet de suivre des fruits entiers puisque la mesure ne nécessite plus de prélèvements.

b. IRM

Dans le domaine des végétaux, Hinshaw (Hinshaw et al., 1979) montre en 1979 l'applicabilité de la méthode IRM aux fruits. Compte-tenu de son important apport par la résolution spatiale et la mesure non destructive, l'IRM a été utilisée pour identifier et caractériser des fruits et en particulier les défauts qui peuvent apparaître durant leur stockage. En ce qui concerne la pomme, on trouve entre autres des études sur le watercore (Figure 1-17).

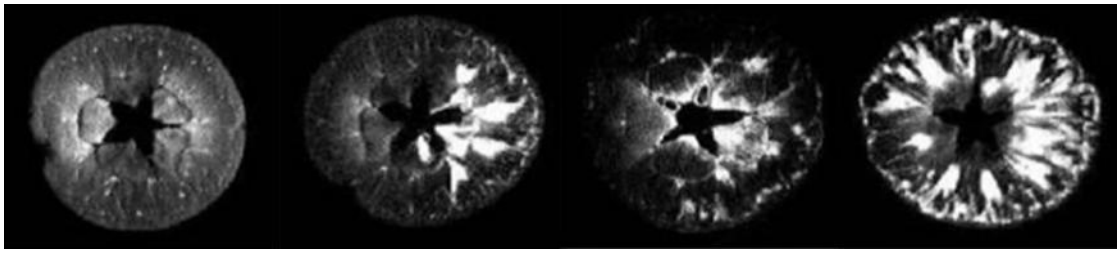

Figure 1-17 (extraite de (Melado et al., 2010)): images IRM en pondération T2 présentant une pomme atteinte de watercore à différents stades : tissu sain (A), stade précoce (B), watercore léger (C), watercore important (D).

L'augmentation du temps de relaxation permet une identification et un suivi de la maladie (Wang et al., 1988). Dans cette étude, des images pondérées T_2 sont utilisées. D'autres travaux ont aussi porté sur le brunissement, visant à une identification rapide de ce défaut par IRM (Gonzalez et al., 2001) pour lesquels un ajustement mono-exponentiel a été réalisé et qui ont montré une augmentation des temps de relaxation et

une modification de la densité de protons dans les tissus lésés : la densité protonique augmente dans un premier temps et diminue ensuite. Selon les auteurs, ces variations pourraient provenir de changements au niveau de l'intégrité cellulaire et des espaces intercellulaires qui modifieraient les inhomogénéités de champs et/ou l'environnement des molécules d'eau. Ultérieurement, une autre étude a confirmé ces observations et les a attribuées à une perte d'intégrité cellulaire provoquant dans un premier l'augmentation de la densité de protons temps puis l'apparition de pores dans le tissu lésé, induisant une diminution de la densité de protons (Defraeye et al., 2013). Le coefficient de diffusion intrinsèque apparaît aussi comme un paramètre adéquat pour la détection du brunissement. Enfin, des recherches ont porté sur la farinosité, toujours par ajustement mono-exponentiel (Barreiro et al., 2000; Barreiro et al., 1999). Néanmoins, il n'a pas pu être établi de changements du T_2 mono-exponentiel qui permette d'identifier simplement les fruits farineux.

Des études ont aussi porté sur la modification des tissus durant le stockage. Une étude sur la tomate (Musse et al., 2009) montre que le mûrissement s'accompagne d'une baisse des temps de relaxation (T_1 et T_2) mono-exponentiels dans la majorité des tissus sauf dans les cavités loculaires. De rares études multi-exponentielles en IRM ont montré une redistribution de l'eau entre deux pools de protons et une baisse des temps de relaxation dans le kiwi durant 65 jours de stockage dont 45 jours au froid (Taglienti et al., 2009). Ces phénomènes ont été rapprochés de la perte de fermeté du fruit mesurée par pénétrométrie durant cette période de mûrissement, sans établir de lien direct entre les paramètres IRM et le changement de texture. L'IRM a aussi été utilisée pour caractériser le tissu sain dans la pomme à l'aide d'un micro-imageur à 11.7T, nécessitant donc de faire des prélèvements dans le fruit (Defraeye et al., 2013). Les auteurs montrent qu'il existe des différences dans le signal mono-exponentiel entre les différentes régions du fruit (cortex et cœur). Mais à cette valeur de B_0 (11.7T), il est très probable que le temps de relaxation soit principalement affecté par la porosité via les effets de susceptibilité.

L'IRM permet en outre de cartographier la distribution de l'eau au sein d'un tissu. Des mesures ont été réalisées dans les tissus du champignon (Donker et al., 1996). Elles ont permis d'extraire les T_2 pour constater que l'influence de la diffusion des molécules d'eau à travers le gradient de lecture et les gradients d'inhomogénéité entraine une

chute des temps de relaxation. Les T_2 ont été modélisés par des courbes de décroissance mono-exponentielles et les auteurs ont constaté que l'utilisation d'appareils à bas champ permettait d'obtenir de meilleurs signaux pour des milieux végétaux poreux en raison d'un effet moindre de la susceptibilité magnétique à bas champ.

La diffusion a aussi été appliquée en IRM avec l'imagerie pondérée en diffusion (Diffusion Weighted Imaging). Ces applications ont permis de cartographier la diffusion, la perméabilité et la taille des cellules dans la carotte (Sibgatullin et al., 2010). Les cartographies nécessitent toutefois de pouvoir considérer un tissu homogène à l'échelle du pixel, ce qui n'est pas toujours le cas, en particulier au niveau des tissus vasculaires (xylème et phloème). De plus une approche T_2-diffusion est compliquée compte tenu du temps de prise de mesure comparé aux phénomènes biologiques mesurés.

Ces différents exemples illustrent la forte sensibilité des temps de relaxation à la structure des tissus et à l'intégrité des cellules. Toutefois, force est de constater que la majorité des travaux sont conduits et interprétés sur la base de mesures du temps de relaxation transversale ou longitudinale à partir d'ajustements mono-exponentiels. Cette démarche ne permet pas d'identifier tous les changements impliqués, en particulier au niveau de la distribution d'eau intracellulaire, comme peut le faire une démarche multi-exponentielle. En effet, une variation du T_2 mono-exponentiel peut refléter soit une variation des amplitudes multi-exponentielles, soit une variation des temps de relaxation, ou encore une variation simultanée des deux paramètres. Suivant le cas de figure, les interprétations seront différentes. Par exemple, une variation des amplitudes sera à rapprocher de changements de la quantité d'eau au sein des compartiments. Au contraire, un changement de temps de relaxation de la vacuole sera explicable par des changements de la structure des membranes ou de la composition de l'extrait sec de la vacuole ou encore de sa taille. De plus, des variations spécifiques de tels ou tels compartiments seront aussi une aide à l'interprétation. Ceci démontre l'intérêt de conduire des mesures sur la base de séquences multi-écho de spin permettant d'accéder à un signal multi-exponentiel (Adriaensen et al., 2013).

III. CONTEXTE ET OBJECTIFS DE L'ETUDE

Nous avons vu que les sources d'influence du fruit sur le signal RMN sont multiples. En premier lieu, au niveau moléculaire, la composition des différents compartiments aqueux en sucres, en ions et en matière sèche va modifier les temps de relaxation. D'autre part, et de manière plus importante, la taille des principaux compartiments de la cellule, et par conséquent la taille des cellules dans le fruit, vont influencer les temps de relaxation. L'influence de ces paramètres sur le signal RMN du fruit n'a jusqu'ici pas été hiérarchisée et présente un enjeu important dans la compréhension des mécanismes impliqués.

Par ailleurs, l'ensemble des études IRM s'est majoritairement focalisé sur l'analyse d'une décroissance mono-exponentielle. Le caractère hétérogène des tissus considérés est une source de variation supplémentaire qui n'a que rarement été étudiée.

Enfin, l'IRM permet des études non destructives du fruit qu'il serait particulièrement intéressant de relier à ses propriétés texturales. Ces dernières sont bien décrites par des mesures mécaniques qui sont très liées à la structure du tissu, et quelques études ont cherché les liens entre les paramètres IRM et les propriétés mécaniques et texturales du fruit (Barreiro et al., 2002; Tu et al., 2007). Cependant, le caractère viscoélastique n'a que rarement été sondé et peu de liens ont été trouvés.

L'idée originale développée dans cette thèse est d'utiliser une approche multi-instrumentale qui permet de contrôler une grande partie des paramètres connus pour intervenir dans le signal de relaxation. En réalisant l'ensemble des mesures sur des fruits contrastés et en fonction du temps, on espère hiérarchiser l'impact des mécanismes intervenant dans le signal de relaxation. Dans un second temps, l'ensemble des paramètres mesurés est rapproché des processus biologiques se produisant dans le fruit et permet une meilleure caractérisation de la pomme et de son évolution au cours du stockage au froid.

Le premier chapitre cherche à identifier les paramètres intervenant dans le signal de relaxation multi-exponentielle mesuré par IRM grâce à une collection de fruits contrastés. Dans la seconde partie, une approche multi-instrumentale est utilisée pour caractériser les différences variétales et les différences dues au stockage au sein du

parenchyme en termes de propriétés mécaniques, de propriétés chimiques et de paramètres IRM. Le troisième chapitre cherche à caractériser par IRM les variations relatives des différents tissus au cours du stockage dans l'ensemble du fruit. Une discussion générale conclura ensuite ce manuscrit. Enfin, une annexe a été ajoutée pour discuter la méthode de mesure IRM.

Chapter 2: MRI investigation of subcellular water compartmentalization and gas distribution in apples

Guillaume Winisdorffer[a,b], Maja Musse[a,b], Stéphane Quellec[a,b], Devaux Marie-Françoise[c], Marc Lahaye[c], François Mariette[a,b]

[a]IRSTEA, UR TERE, 17 avenue de Cucillé, CS 64427, 35044 Rennes, France,

[b]Université européenne de Bretagne, France,

[c]INRA, UR1268 BIA, Rue de la Géraudière, BP 71627 44316 Nantes Cedex 3, France

2. MRI investigation of subcellular water compartmentalization and gas distribution in apples

Abstract

Water status and distribution at subcellular level in whole apple fruit were evaluated by Magnetic Resonance Imaging (MRI) measurement of the multi-exponential transverse (T_2) relaxation of water protons. Apparent microporosity, also estimated by MRI, provided mapping of gas distribution in fruit tissues. Measuring for the first time the multi-exponential relaxation of water and apparent tissue microporosity in whole fruit and combining these with histological measurements provided a more reliable interpretation of the origins of variations in the transverse relaxation time (T_2) and better characterization of the fruit tissue. Measurements were performed on 54 fruit from 3 different cultivars. Fruit of different sizes were selected for each cultivar to provide tissues with cells of different dimensions. Macrovision measurements were carried out on parenchymal tissue from all fruit to investigate the impact of cell morphology and cell size of all samples on T_2 contrast.

The results showed that the MRI transverse relaxation signal is well fitted by a tri-exponential decay curve that reflects cell compartmentalization. Variations in cell size partially explained the different T_2 observed. This study highlighted the heterogeneity of apple tissues in terms of relaxation parameters, apparent microporosity and cell morphology and in relation to specific variations between fruit of different sizes and between cultivars.

I. INTRODUCTION

Apple fruit has been widely studied because of its economic importance. Among the different tissues making up this fleshy fruit (Figure 2-1), the parenchyma is very important as it is the main consumable part. Its texture depends on cellular structure and organization as well as on the biochemical composition of the tissue (Bourne, 1982).

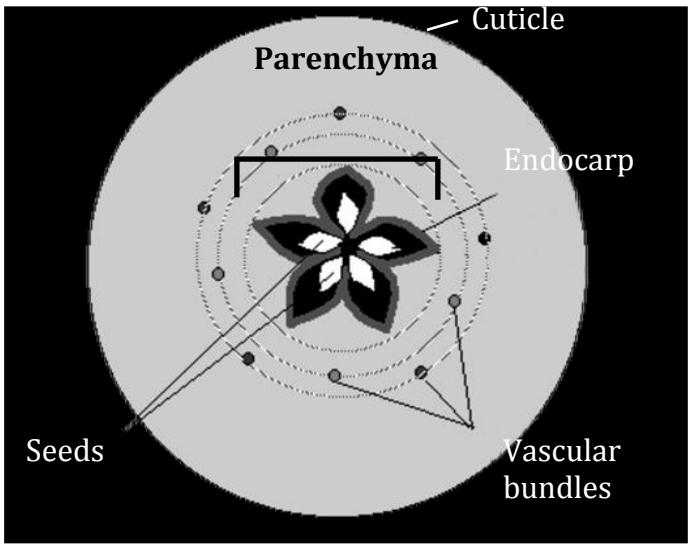

Figure 2-1: Diagram of the equatorial plane of an apple showing the internal structure of the fruit.

The histological features of the apple parenchyma have already been described (Khan and Vincent, 1990; Schotsmans et al., 2004); parenchyma cells situated immediately under the cuticle are relatively small and round. Cells rapidly increase in size in the first millimeters under the cuticle and then elongate with distance from the cuticle. As for many fleshy fruit, the size of the apple fruit depends on cell number and cell size (Harada et al., 2005; Malladi and Hirst, 2010; Volz et al., 2004). In addition to cells, the apple parenchyma contains intercellular spaces that form pores, increasing in occurrence towards the cuticle, except for the region immediately under it (Herremans et al., 2013; Schotsmans et al., 2004). This microporosity increases with fruit size (Volz et al., 2004) though it appears to be related to orchard management (Goffinet et al., 1995).

Nuclear Magnetic Resonance (NMR) relaxation and Magnetic Resonance Imaging (MRI) have been used in several studies to investigate water in plant tissues (Van As and van Duynhoven, 2013). The NMR signal of water is characterized by longitudinal (T_1)

and transverse (T_2) relaxation times that are governed by contributions from different factors (Hills and Duce, 1990; Van As, 2007). First, bulk relaxation is related to the mobility of water and is affected by the chemical exchange of water protons with macromolecules and solid surfaces. Water in different cell compartments thus has different bulk relaxation times due to distinct concentrations and the nature of osmolites. Secondly, relaxation times are modified by diffusional exchange of molecules between compartments through permeable membranes. In the case of slow diffusional exchange, the resulting water relaxation signal is multi-exponential, reflecting water compartmentalization. Three or four components have been obtained in the apple, depending on the NMR protocol. These have been assigned to the vacuole, the cytoplasm and the wall/extracellular water (Hills and Remigereau, 1997; Sibgatullin et al., 2007; Snaar and Van as, 1992). NMR relaxation measurements can be used to estimate the relative proportions and the properties of water in different compartments. T_2 relaxation time is used for plant cell investigations rather than T_1, as differences in T_2 are more pronounced for the different cell compartments (Van As, 2007). Due to the contributions of the different factors described above, compartment size affects T_2 relaxation times (Brownstein and Tarr, 1979; Van der Weerd et al., 2001). According to the NMR relaxation model in porous media adapted by Van Der Weerd et al. to plant cells, the T_2 of water ($T_{2,obs}$) confined in a vacuolar compartment can be defined as a function of the bulk T_2 ($T_{2,bulk}$), the radii of the vacuole along spatial directions (R_x, R_y, R_z) and the sink strength (H) describing the rate of the loss of magnetization at the membrane boundary:

$$\frac{1}{T_{2,obs}} = H\left(\frac{1}{R_x}+\frac{1}{R_y}+\frac{1}{R_z}\right)+\frac{1}{T_{2,bulk}}$$

Equation 2-1

In general, H is affected by the exchange of water with molecules from an adjacent compartment with different T_2 through the permeable membrane, and by direct interaction with the membrane acting as a sink for relaxation. The wide variation in cell size in pearl millet and maize stems allowed the demonstration of Equation 2-1 for plant cells, assuming that the mono-exponential adjustment of the T_2 relaxation curve reflects only the T_2 from the vacuole compartment (Van der Weerd et al., 2001).

In addition to the complexity of the phenomena that affect T_2 values, other mechanisms also modulate the T_2 measured (Edzes et al., 1998). The latter is reduced by diffusion in the presence of random field gradients generated by susceptibility inhomogeneities and, in the case of MRI measurement, by diffusion in the presence of imaging gradients (Donker et al., 1996; Edzes et al., 1998). In fruit, the magnetic susceptibility inhomogeneities originate mainly from gas associated with the microporosity of the sample; this is accentuated at higher magnetic fields and has to be considered in interpretation of the T_2 since considerable reduction in the T_2 has been recorded with increased magnetic field strength (Donker et al., 1996; Musse et al., 2010b).

MRI studies of apples reported in the literature have mainly focused on the development of techniques for detection of metabolic disorders and the non-destructive nature of the method has been particularly highlighted. T_2 has been used as a local marker of tissue modification (Chen et al., 1989; McCarthy et al., 1995) and T_2 weighted images or T_2 maps have therefore been established in apples to study fruit quality and defects and as a probe for defects happening over time. For example, development of watercore (Cho et al., 2008a; Clark et al., 1998b; Melado-Herreros et al., 2013) and internal browning (Cho et al., 2008a; Clark and Burmeister, 1999; Gonzalez et al., 2001), both linked to changes in microstructure implying flooding of intercellular pores (Herremans et al., 2014; Herremans et al., 2013; Suzuki, 2003), collapse of cell wall, and cells for browning disorder (James and Jobling, 2009), were at the origin of changes in T_2. Mealiness was also linked to changes in relaxation times (Barreiro et al., 2002; Barreiro et al., 2000; Barreiro et al., 1999). The use of a T_2 map to study the microstructural heterogeneity of healthy apple parenchyma has been less widely explored. This aspect was recently addressed by Defraeye et al. (Defraeye et al., 2013) in measuring T_2 in regions of interest in cortex and core tissues and showed differences in T_2 between the two tissues. T_2 was also used to extract quantitative information in the recently proposed method for measurements of microporosity (Musse et al., 2010b). This method exploits the susceptibility effects induced by small gas bubbles on the MRI relaxation signal. Using a combination of T_2 and T_2^* maps, Musse et al. showed that a microporosity map can be quantified in fruit.

All MRI T_2 mapping on fruit to date has been limited to the estimation of mono-exponential relaxation. An MRI method allowing assessment of spatially resolved multi-exponential T_2 has recently been proposed (Adriaensen et al., 2013) and applied to apples. Using this MRI method, the multi-exponential T_2 and their relative amplitudes can be directly computed in different regions of interest.

The techniques commonly used for the analysis of fruit tissue structure (i.e. microscopy and X-ray microtomography) have a local character and therefore do not provide a global view of the whole fruit. Additional spatially resolved information on the relative proportions and properties of water in cell compartments and on the microporosity of tissues would therefore increase understanding of fruit microstructure and help to understand factors affecting its texture. The main aim of the study presented here was to evaluate the microstructure of apple parenchyma via spatially resolved multi-exponential T_2 relaxation measurements. As apple tissue is known to be very porous, microporosity maps were computed and considered in the analyses of relaxation parameters. The sensitivity of T_2 to the cell dimensions in the range of cell sizes found in apple parenchyma was investigated to improve our understanding of the MRI signal in fruit. The second aim was to investigate variations in both T_2 and microporosity inside apple fruit, with a focus on the parenchyma tissues. Multi-exponential T_2 and microporosity maps were established in 54 fruit from 3 different cultivars. Fruit of different sizes were selected for each cultivar to provide cells of different dimensions. Macrovision measurements (Devaux et al., 2008) were carried out on all fruit to investigate cell morphology and to estimate the cell size of the samples.

II. MATERIALS AND METHODS

1) Fruit and sampling

Apples were studied from three different cultivars (Fuji, Ariane, Jonagored) harvested at maturity. Their horizontal and vertical circumference (C_h and C_v) were measured with a measuring tape and volumes were estimated as $V = \frac{4}{3}\pi \left(\left(\frac{C_h}{2\pi}\right)^2 \times \frac{C_v}{2\pi}\right)$. All apples were weighed on a digital balance (Testus PFCD 6000, France) and sorted for weight:

1) Fruit from the Fuji cultivar consisted of 9 large (290 ± 23 g), 9 medium (185 ± 21 g) and 9 small (124 ± 27 g) apples (standard deviation corresponds to the dispersion of apple weights).

2) Fruit from the Ariane cultivar consisted of 6 medium (187 ± 12 g) and 3 small (133 ± 3 g) apples.

3) Fruit from the Jonagored cultivar consisted of 7 large (301 g ± 21 g) and 7 small (131 ± 16 g) apples.

Fuji and Ariane apples were grown at an experimental station (INRA, Angers) and were stored at 2°C for two months. Jonagored apples were obtained from a local organic farmer and stored at 2°C for five months.

Three samples were taken from the outer pericarp of 9 Fuji fruit (3 of each size) and 3 Ariane fruit (2 small and 1 medium) to measure water content (WC). WC was expressed as difference in weight after lyophylisation (Cosmos, Cryotec, Saint-Gély-du-Fesc, France).

2) MRI

a. Acquisition

MRI measurements were carried out on a 1.5T MRI scanner (Magnetom, Avanto, Siemens, Erlangen, Germany). Fruit were maintained at a constant temperature (20 ± 0.5°C) during acquisitions. The median planes of fruit (transverse section at middle height of fruit) were imaged with a pixel size of 1.19 mm x 1.19 mm, a slice thickness of

5 mm and a repetition time of 10 s. Two MRI sequences were performed: (i) a multi spin echo (MSE) sequence with non-selective refocusing pulse, inter-echo spacing (ΔTE) of 7.1 ms, bandwidth 260 Hz/pixel, 1 scan and 512 echoes per echo train for estimation of T_2 and (ii) a multi gradient echo (MGE) sequence, with first echo time (TE1) of 2.8 ms and ΔTE 1.6 ms, bandwidth 1096 Hz/pixel, 12 echoes and 2 averages for estimation of T_2*.

The Signal to Noise Ratio (SNR) of the images obtained by the MSE and MGE sequences at the shortest echo time was approximatively 120 and 80, respectively.

b. *Image processing*

The T_2 and T_2* of apple parenchyma were computed by both pixel-by-pixel- and Region of Interest (ROI)- based approaches, as described above. First, a pixel-by-pixel approach was used to calculate T_2 and T_2* maps using Scilab software (Scilab 2012). Prior to fitting, seeds and core tissue around them together with the image background were masked using Otsu's thresholding method (Otsu, 1979). Mono-exponential T_2 maps were generated by performing pixel-to-pixel fitting via the Levenberg-Marquardt algorithm for chi-square minimization according to Equation 2-2 (for i=1).

$$I(t) = \sum_{i=1}^{n} I_{0i} \times e^{-\frac{t}{T_{2i}}} + const$$

Equation 2-2

where t is the time, I_{0i} the amplitude, T_{2_i} the transverse relaxation time of each component of the signal and *const* a value modeling the background offset. T_2* maps were computed as described for T_2 maps by substituting T_2 by T_2* in Equation 2-2. Apparent microporosity maps were then computed from T_2 and T_2* maps according to Musse et al (Musse et al., 2010b). A discussion on microporosity estimation is presented in the appendix of this work.

An ROI-based approach was used for estimation of multi-exponential relaxation parameters as it improved SNR (Adriaensen et al., 2013). ROIs were selected manually

on homogeneous regions of mono-exponential T_2 maps using ImageJ software (Schneider et al., 2012). Regions with homogeneous mono-exponential T_2 were considered to have homogeneous multi-exponential T_2. The outer and inner cortex regions were selected to be close to the cuticle and the core, respectively (Figure 2-2A). Selection of the outer cortex region avoided the first 2 mm region under the cuticle while selection of the inner cortex avoided the principal vascular bundles. The mean ROI signals were computed with ImageJ software for all the MSE images of the series and then fitted via the Levenberg-Marquardt algorithm for chi-square minimization with TableCurve 2D software (Systat, 2007) according to a tri-exponential decay curve (Equation 2-2, i=3).

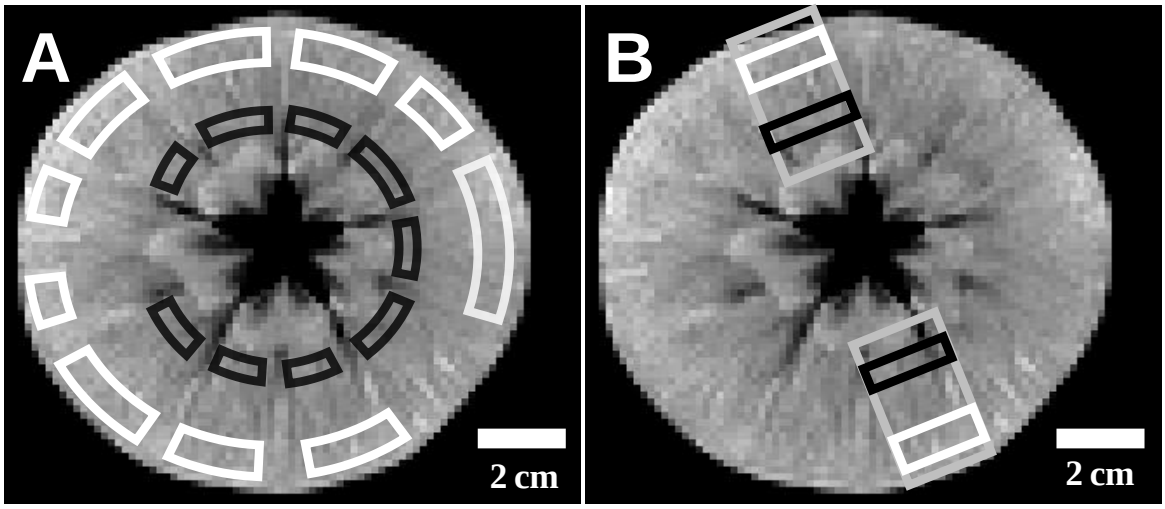

Figure 2-2: MRI T_2-weighted image showing (A) the regions of interest used for MRI multi-exponential fitting corresponding to the outer (white, approximately 350 voxels) and inner (black, approximately 180 voxels) cortex tissue and (B) the region of sampling used for the macrovision imaging (gray) with the outer (white) and inner (black) areas used for granulometric analysis.

Values of the apparent microporosity used for statistics were estimated for the same ROIs as selected for estimation of multi-exponential T_2. In order to improve accuracy, T_2 and T_2* required for microporosity estimation were computed from the mean ROI intensity values rather than on a pixel-to-pixel basis.

More details about MRI measurements and numerical simulations of T_2 and T_2* signals used for estimation of the errors in computing multi-exponential T_2 relaxation parameters and apparent microporosity are given in Appendix.

3) Macro-vision imaging

a. Sampling and acquisition

Two days after MRI measurements, samples were taken from each fruit for macrovision imaging. The sampling protocol consisted of cutting a 1 cm slice, corresponding to twice the MRI virtual slice, at the equator of the fruit. Two 1 cm wide rectangular samples were then taken from the cortex (see Figure 2-2B, gray line) and kept for two months at 4°C in a solution composed of 85:10:5% (v/v) ethanol 96%, formaldehyde 37% solution and acetic acid. Before imaging, tissue was rehydrated by placing the sample in successive ethanol baths (70%, 50% and 30%). Finally, 200 µm thick sections were cut from the middle of each sample using a vibrating blade microtome (MICROM, HM 650V, Microm International GmbH, Walldrof, Germany). They were degassed for 30 s under mild vacuum to remove remaining air bubbles. Sections were then imaged under water using a macro-vision system (Devaux et al., 2008) comprising a CCD camera (Sony XC 8500 CE, Alliance Vision, Montélimar, France) fitted with a 50 mm lens (f 1:1.8 Nikon) and a 20 mm extension tube. Samples were back-lit using a fiber-optic ring-light supplied by Polytec (Pantin, France). The camera and lens were adjusted to observe a 10.7 mm x 14.4 mm area and images were digitized in 1620 x1220 pixels (pixels of 3.6x3.6 μm^2).

b. Image processing

Two to four images per fruit were selected for image analysis. Images were considered for visual texture analysis according to both cell morphology and arrangement as they did not allow segmentation of cells. Image pixels were coded from 0 (black) to 255 (white). Gray level granulometric methods were applied using MatLab software to extract overall information concerning distribution of cell dimensions (Devaux et al., 2008) on ROIs of the inner and outer regions of the cortex (see Figure 2-2B). ROIs were selected (MatLab software) to correspond to MRI ROIs. Outer ROIs began at 1.5 mm from the cuticle and ended at 40% of the image length. Inner ROIs began at 60% of the image length from the cuticle and were 80% of the outer ROI length wide. By applying successive morphological closings on ROIs, dark objects on the image

smaller than the structuring element were filled by the mean pixel value under the mask. A curve V_i was constructed by measuring the sum of gray levels after each closing step versus the size of the structuring element. The raw curve was normalized according to the sum of the initial ($V_{initial}$) and final (V_{final}) gray levels and written as: $g_i = (V_i - V_{i+1})/(V_{initial} - V_{final})$ where g(i) is the percentage of variation in gray level for the i^{st} step. The maximum size of the structuring element was set at 200 pixels, corresponding to 726 µm.

Horizontal and vertical linear structuring elements were applied, allowing analysis of cell dimensions in both directions. To compare the results from the different fruit, granulometric curves of gray levels were summarized for each direction by computing mean gray level sizes as the weighted sums bellow, thus providing the mean cell length (l) in the direction under consideration:

$$l = \exp\left(\sum_{i=1}^{imax} \frac{g(i) * \log(t_i)}{100}\right)$$

Equation 2-3

where t_i is the size of the structuring element in µm and i_{max} the number of closing steps. This mean was considered to emphasize the smallest size.

Cell volume was estimated by considering the cells to be cylinders with the height (h) radial to the cuticle (cells were radially elongated) and the radius (r) parallel to the cuticle: $V = \pi r^2 \times h$.

As they were based on variations in gray level of pixels, granulometric curves did not measure the actual cell dimensions but a combination of cell dimensions and gray levels in which cells and pores could not be distinguished. Cell dimensions and consequently volume were therefore subject to uncertainty.

4) Statistics

MANOVA tests were performed using Statgraphics (Centurion) software to detect significant differences ($p < 0.01$) between measurements. The multifactor MANOVA test was applied to evaluate the differences between fruit sizes (small, medium and large)

and between the inner and outer regions. Fruit size, region and cultivar, taking into account both cultivar and storage period, were used as factors. F-tests were performed on the results to assess the significance of the differences observed.

III. RESULTS AND DISCUSSION

1) Spatial distribution of T_2

Typical mono-exponential T_2 maps of Fuji and Ariane apples of different sizes are shown in Figure 2-3.

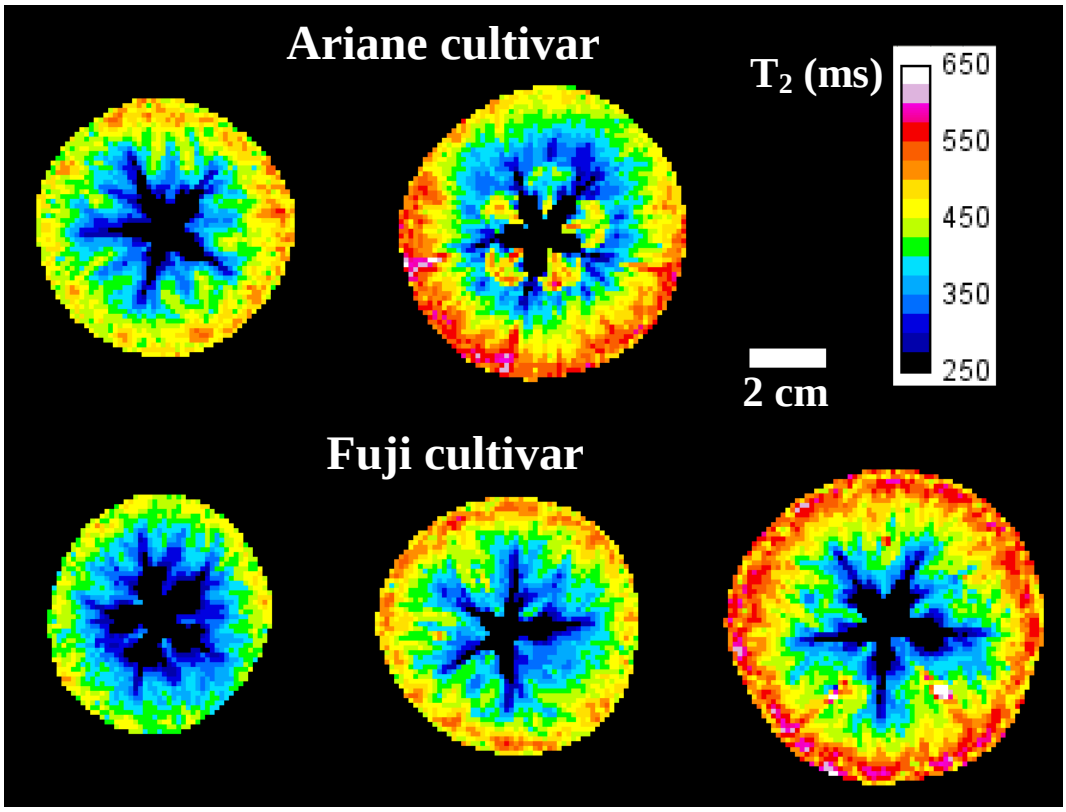

Figure 2-3: Mono-exponential T_2 maps of Ariane and Fuji cultivars of different sizes. The reader is referred to the web version of this article for interpretation of the references to color in this figure legend.

The maps reflect the heterogeneity of the apple tissues. A pattern of radial variation was observed, with a progressive increase in T_2 values from the center of the fruit (~300 ms) to the region near the cuticle (~ 450 to 600 ms). The average T_2 in the inner cortex was about 350 ms, whereas it was about 600 ms in the outer cortex. In some apples,

independently of fruit size or cultivar, the T_2 of the core and of the middle cortex were close and made it possible to distinguish the core from other tissues (e.g. medium Ariane fruit Figure 2-3). The vascular bundles were seen in some Fuji apples as their T_2 values contrasted from the surrounding tissue, the T_2 values being either higher or lower depending on the bundle (large Fuji, Figure 2-3). Vascular bundles are known to be composed of small cells and lignified cell walls. They should thus have lower T_2 values than the surrounding tissues and the contrast should generally emphasize dry bundles. The high T_2 (up to 800 ms) observed in the vascular bundle area was probably due to the lower porosity in the vessel and a higher mobility of water which could be due to water-filled large vessels. In some fruit, differences between fruit sides were observed in the cortex (for example, differences between the top and bottom in the T_2 map for the Ariane cultivar, Figure 2-3). Fruit development conditions such as sun exposure may have been at the origin of these differences between the two sides of the fruit.

Independently of fruit size, T_2 maps showed similar radial T_2 variations. However, when comparing fruit of different sizes, a global increase in T_2 value with fruit size was observed for parenchyma tissues. In particular, T_2 in the outer cortex region were about 450 ms for small fruit and up to 600 ms for large fruit.

The Jonagored cultivar (Supplementary Figure 2-8A) showed a very similar global aspect, in terms of both the T_2 map pattern and the relationship between T_2 and fruit size.

In order to investigate sub-cellular water status and distribution, multi-exponential fitting was performed on the mean signal from the ROIs (Figure 2-2A) corresponding to the outer and inner cortex. The results for all fruit are given in Table 2-1.

Table 2-1: Multi-exponential fit parameters and estimations of microporosity in cortex of apple

Outer Cortex									
Cultivar	Size	I_{01} [%]	T_{21} [ms]	I_{02} [%]	T_{22} [ms]	I_{03} [%]	T_{23} [ms]	T_{2mono} [ms]	Apparent microporosity [%]
Ariane	M	3±0	31±4	17±0	139±9	80±1	531±22	469±23	42±4
	S	3±0	22±2	15±1	129±8	82±1	524±26	469±18	34±2
Fuji	L	3±0	25±2	14±1	136±4	82±1	549±7	494±5	39±2
	M	3±0	23±2	14±1	126±6	83±1	522±24	471±23	39±2
	S	2±1	20±4	14±0	115±11	83±1	482±34	437±30	33±3
Jonagored	L	7±4	65±22	19±1	214±69	74±5	512±30	451±22	34±4
	S	7±4	67±21	14±3	187±41	78±2	465±24	420±24	28±6
Inner Cortex									
Cultivar	Size	I_{01} [%]	T_{21} [ms]	I_{02} [%]	T_{22} [ms]	I_{03} [%]	T_{23} [ms]	T_{2mono} [ms]	Apparent microporosity [%]
Ariane	M	3±0	18±4	21±1	104±5	76±1	407±26	351±24	28±6
	S	3±0	19±4	17±0	107±4	80±0	451±20	401±17	28±2
Fuji	L	3±1	18±4	18±1	113±8	79±1	465±25	410±22	26±3
	M	3±0	18±3	17±1	104±7	80±1	439±26	390±22	28±2
	S	3±1	16±3	16±1	98±6	81±1	410±22	368±20	25±4
Jonagored	L	8±4	57±19	19±2	175±47	72±3	454±21	395±17	25±3
	S	14±4	80±12	14±6	210±50	71±6	414±24	362±24	19±4

Results of the fit using the Levenberg-Marquardt algorithm are presented for outer (A) and inner (B) cortex ROIs of each cultivar.

In all cases, the multi-exponential T_2 parameters consisted of one short T_2 component (< 80 ms) with low relative intensity (< 10 %), an intermediate T_2 component (100 to 220 ms) with 14 to 20% of signal intensity and a long T_2 component (400 to 550 ms) representing 70 to 80% of the signal. For comparison, the mono-exponential value measured on the same ROIs (T_{2mono}) is given in Table 2-1. The standard deviations did not increase between the mono- and the multi-exponential results, indicating there was no degradation of the fit although seven variables were used for fitting instead of three. The relationship between T_{2mono} and T_{23} was

linear, ($y = 1.12 \times x, r^2 = 0.97$) while none was found between T_{22} and T_{2mono} or T_{21} and T_{2mono}, demonstrating that the variations observed with mono-exponential T_2 mainly reflected changes in the vacuole compartment. However, T_{2mono} underestimated the T_2 of the vacuole compartment and did not provide access to other compartments.

Table 2-2 shows the results of the MANOVA test performed on mono- and multi-exponential data, with gray cells corresponding to significant variations.

Table 2-2: Analysis of variance for MRI parameters with position within cortex, size and fruit

	I_{01}		**T_{21}**		**I_{02}**		**T_{22}**		**I_{03}**		**T_{23}**		**T_{2mono}**		**Apparent microporosity**	
	F	P	F	P	F	P	F	P	F	P	F	P	F	P	F	P
Position	3.3	0.07	4.8	0.03	25.2	0.00	11.9	0.00	32.6	0.00	198.6	0.00	230.8	0.00	203.5	0.00
Caliber	2.2	0.11	1.3	0.27	16.3	0.00	0.5	0.60	3.6	0.03	32.8	0.00	24.2	0.00	20.0	0.00
Cultivar	64.2	0.00	166.1	0.00	10.8	0.00	65.9	0.00	77.2	0.00	7.1	0.00	10.9	0.00	12.4	0.00

F-test value (F) and probability for the null hypothesis (P) are presented for each MRI parameter.

The mono-exponential T_2 was found to be discriminating for all parameters studied with a relatively high F-factor for the position (Table 2-2), confirming observations from mono-exponential T_2 maps (Figure 2-3). In the case of the multi-exponential parameters, the most discriminating parameter depended on the variation considered. T_{23} had the most significant variations when comparing different positions, in agreement with the analysis performed on mono-exponential data, and reflecting a change in vacuole water status. The relative intensities of components 3 and 2 (I_{03}, I_{02}) also varied significantly between the inner and outer cortex. According to the attribution of the different T_2 components proposed by Snaar et al. (Snaar and Van as, 1992), this means that the proportion of vacuole water was higher and the proportion of cytoplasm water was lower in cells of the outer cortex than in cells of the inner cortex. Finally, T_{22} was also found to vary significantly between the inner and outer cortex, reflecting changes in the cytoplasm water status in addition to the proportion of water enclosed.

The parameters for fruit size were less affected. Only variations in T_{23} and I_{02} were significant, the relaxation time being lower and proportion of water enclosed in the cytoplasm being greater in the inner cortex.

On the other hand, variations between apple cultivars significantly affected all components of the multi-exponential T_2 signal, with relatively high F-factors which were not observed with the mono-exponential T_2. The parameters associated with the first component varied very significantly between cultivars but not between the outer and inner cortex tissue or between fruit of different sizes, suggesting that the amount of water and the relaxation time attributed to the cell wall were cultivar specific. Besides genetic factors, these differences might also have originated from pre-harvest conditions and storage time before measurement as the Jonagored cultivar was mainly responsible for these differences. Fruit from this cultivar were studied after five-month cold storage whereas the others were analyzed after two-month cold storage.

The water content did not explain variations in T_2 values: it was 82.8 ± 1.3% and 82.1 ± 0.7% in the outer cortex tissue of Fuji and Ariane fruit, respectively, and no significant variations were observed with size differences for the Fuji cultivar. Due to experimental constraints the water content was not measured for the inner cortex tissue but, in light of the T_2 variations observed, very significant changes in water content would be necessary, which were most unlikely (Hills and Remigereau, 1997).

As microporosity is also known to affect T_2, it was calculated to check its influence on the variations in T_2 observed.

2) Apparent microporosity and its impact on T_2

The heterogeneity of the apparent microporosity in apple tissues of Fuji and Ariane cultivars is depicted in Figure 2-4. Vascular bundles were the least porous parts of the fruit and were situated in a low microporosity region, highlighting the border between the core and the cortex tissues. Microporosity increased from this border to the outer cortex region and then decreased near the cuticle. For example, apparent microporosity values were about 15% of gas in the tissue for the core, from about 30 to 40 % for the cortex and about 10% in the vascular bundles of Ariane fruit. The same pattern was observed for the Jonagored cultivar (Supplementary Figure 2-8). The apparent microporosity measurements on ROIs from the outer and inner cortex are presented in Table 2-1 and confirm results from apparent microporosity maps. Indeed, apparent

microporosity in the outer cortex region was higher than in the inner cortex region. The result of a MANOVA-test (Table 2-2) showed this variation to be significant.

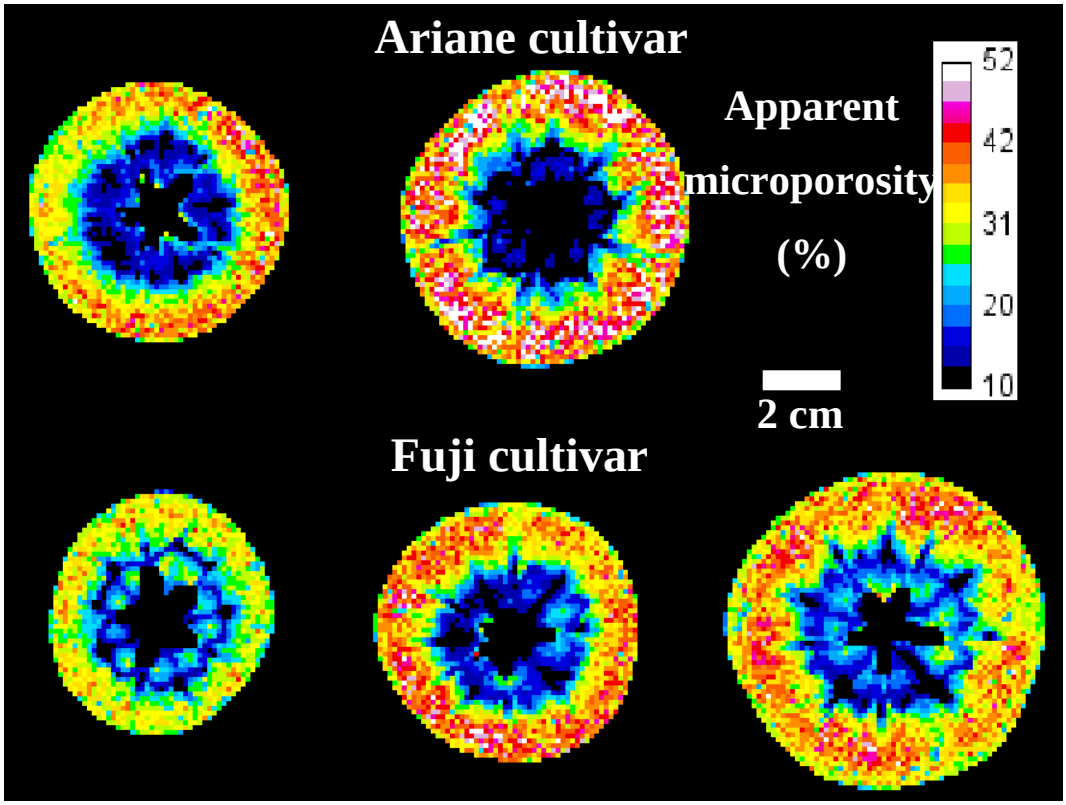

Figure 2-4: Apparent microporosity maps of Ariane and Fuji cultivars of different sizes. The reader is referred to the web version of this article for interpretation of the references to color in this figure legend.

On looking at different fruit sizes, apparent microporosity of the outer cortex increased with the dimensions of fruit for all cultivars (Table 2-2). Microporosity of the inner cortex showed smaller variations with fruit size, in particular for Ariane fruit. In contrast, the greatest variations in the outer cortex were found between small and medium Ariane apples, although these fruit did not vary much in size. The microporosity of Fuji apples increased between the small and medium sizes but not between the medium and large sizes. These results confirmed the increase in apparent microporosity reported with fruit size for Royal Gala apples (Volz et al., 2004) and also highlighted that maximum microporosity can be reached, according to the cultivar. This upper limit may explain the absence of variations in microporosity in Empire apples reported by Goffinet et al. (Goffinet et al., 1995): as fruit thinning had been used to increase fruit size, the different sizes studied may have corresponded to fruit which had already reached a

maximum and constant microporosity. A discussion on the absolute values of apparent microporosity was made in the appendix of this thesis.

Herremans et al. (Herremans et al., 2013) used X-Ray micro-CT to measure microporosity in three regions of Braeburn apples: Region 1, corresponding to a mix of outer cortex and under-cuticle regions as defined in the present paper, Region 2, corresponding to a mix of outer and inner cortex tissue, and Region 3, corresponding to the core tissue. They reported apparent microporosity values of 15, 18 and 19.9% for regions 1 to 3, respectively. Our results are in good agreement with these findings. The core tissues of Ariane, Fuji and Jonagored apples had the lowest microporosity; the low microporosity observed in the under-cuticle region in the three cultivars support the lower microporosity of Region 1 compared to the middle cortex reported in Braeburn apples (Volz et al., 2004). The microporosity of Fuji apples estimated using X-Ray microtomography was 29% for an under-cuticle/outer cortex region (Moller et al., 2013), which was lower than our measurements (39% for outer cortex). However, numerous aspects should be considered when comparing microporosity values calculated from different techniques. First, from a biological point of view : studies on different apple cultivars have shown that microporosity values are cultivar dependent and vary according to pre- and post-harvest conditions and maturity (Goffinet et al., 1995; Herremans et al., 2013; Schotsmans et al., 2004). For example, the microporosity estimated in the middle cortex tissue of Braeburn and Jonica apples was 10 % and 16%, respectively, the former increasing during three-month storage to 18%, the latter decreasing to 14% (Schotsmans et al., 2004). The measurement method is another factor: X-Ray microtomography values depend on the measurement protocol. The microporosity varied between 19 and 29% in parenchyma tissue of Jonagold apples depending on the image resolution and representative elementary volume used for the analysis (Mendoza et al., 2007). Similar variations can be expected for MRI since the apparent microporosity depends on the main magnetic field strength (Donker et al., 1996). Comparison of microporosity values from different experiments is therefore difficult, especially as the regions considered for microporosity quantification differ between studies. To circumvent this last limitation, MRI represents a more suitable approach for the analysis of fruit structure as it allows the measurement of the spatial distribution of microporosity in a whole fruit.

Both apparent microporosity and T_2 maps were characterized by specific radial variations (Figure 2-3 and Figure 2-4) with relatively similar aspects. The T_{23}, T_{22} and microporosity values were higher in the outer than in the inner cortex region (Table 2-1). Since higher microporosity induces lower T_2 (Donker et al., 1996), microporosity was thus not the main factor explaining the variations in T_{22} and T_{23}. However, as microporosity was considerably higher in the outer than in the inner cortex, the T_2 and especially T_{23} value ranges were probably underestimated and differences in relaxation times between the cortex were very probably reduced. Defraeye et al. (Defraeye et al., 2013) used a high field MRI scanner (11.7 T) and an MSE sequence with a 7 ms echo time very close to the echo time we used (7.1 ms). They found relatively low T_2 values (between 25 and 40 ms) that were higher in the inner cortex than in the outer cortex. This discordance with our results is probably due to the effects of microporosity-induced susceptibility inhomogeneities at high field and the relatively long TE used (Adriaensen et al., 2013; Donker et al., 1996). As microporosity was found to have more impact on T_2 in tissue rich in air (Musse et al., 2010b), higher microporosity of the outer cortex shortened T_2 values, resulting in lower T_2 values than for the inner cortex. This explanation is supported by their low T_2 values, as the T_2 of porous fruit was shown to decrease with the increase in the magnitude of the main magnetic field (Musse et al., 2010b). The T_2 values measured by Defraeye et al. therefore seem to reflect changes in microporosity rather than changes in water status.

3) Tissue histology and MRI measurements

Figure 2-5 shows the macrovision images of cortex of Fuji and Ariane cultivars with zooms on the regions corresponding to the ROIs used for MRI analyses in the outer and inner cortex tissue.

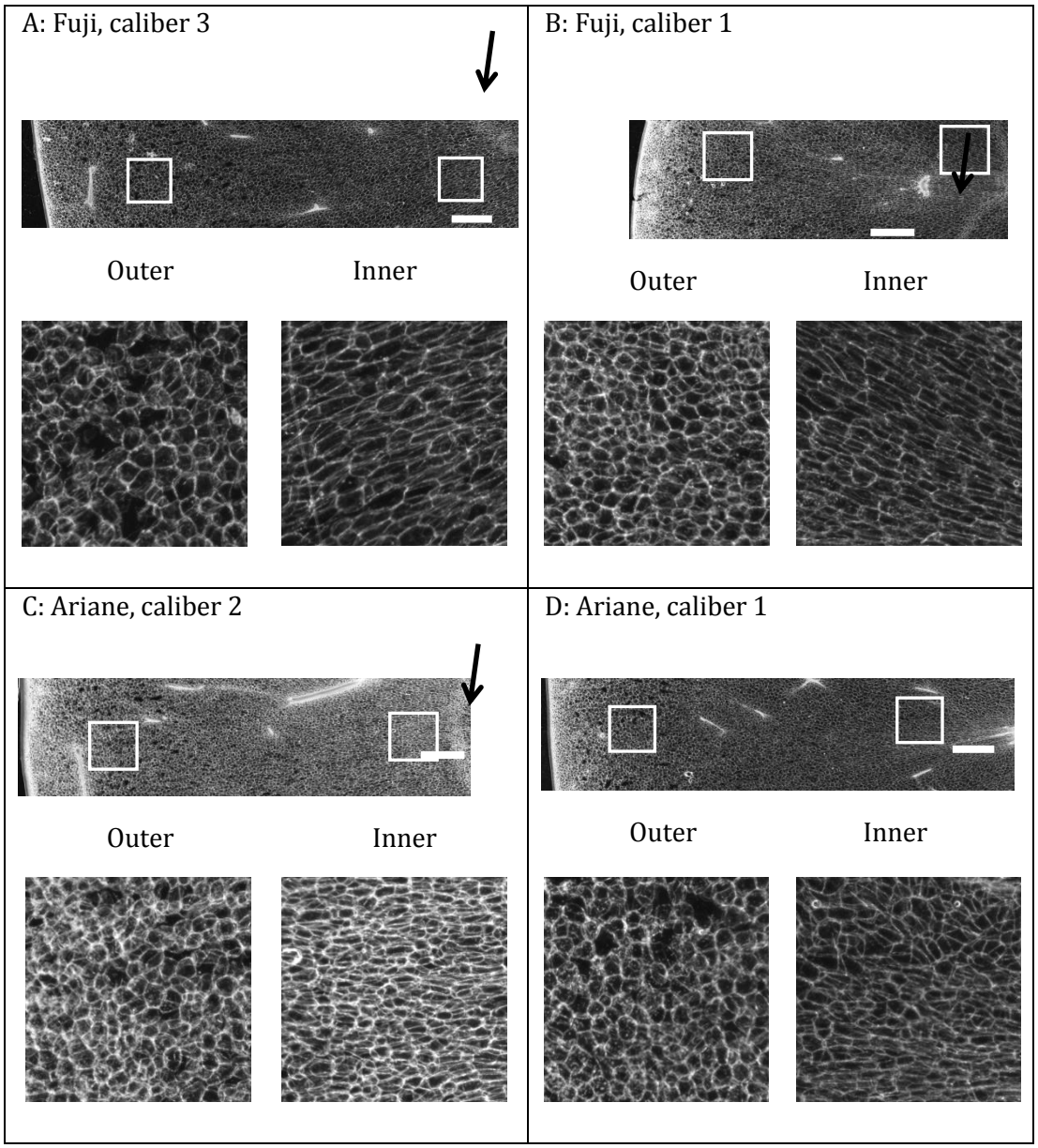

Figure 2-5: Macrovision images of two sizes of Fuji (A-B) and Ariane (C-D) cultivars, corresponding to the whole cortex region, and zoom-in on regions in the inner and outer cortex as analyzed using granulometric methods. Scale bar is 2 mm.

The cortex tissue was heterogeneous in terms both of cell size and shape. Under the cuticle, an approximately 2 mm wide region was composed of small cells with sizes increasing with distance from the cuticle. This region matched the first peripheral pixels of T_2 and microporosity maps (Figure 2-3 and Figure 2-4) characterized by lower apparent microporosity and T_2 values than the rest of the cortex tissue. As the cells were small, there was more light diffusion on the image and the region appears whiter compared to other regions. The outer cortex tissue was characterized by round cells of roughly 180 µm. For most fruit studied, the cells tended to elongate in a direction

perpendicular to the cuticle when the distance from the cuticle increased. Some inner cortex tissues included non-elongated cells (Figure 2-5D). The elongated cells observed close to the vascular bundles were often oriented (Figure 2-5A, B) in the direction of the closest vascular bundle. The border between the cortex and core tissues (Figure 2-5A, B and C, arrows) was a compact tissue with smaller cells, appearing slightly brighter as in mature fruit (Esau, 1977; Fisk, 1962). These findings agreed with previous studies on apple parenchyma histology, showing the tissue cell morphology dependency on location (Bain and Robertson, 1951; Khan and Vincent, 1990; Schotsmans et al., 2004). They highlighted heterogeneity of the higher tissue structure of the inner parenchyma compared to the outer parenchyma tissue for fruit of the same size and cultivar. When comparing fruit of different sizes, large fruit appeared visually to be richer in intercellular spaces in the outer part of the pericarp (Figure 2-5). The cell shape of small fruit tended to be more heterogeneous in the inner parenchyma tissue.

The cell morphology of the Jonagored cultivar was similar and varied in the same way between the outer and inner regions (Supplementary Figure 2-9). The image texture algorithms used to analyze macrovision images yielded size distributions of dark objects, which were used to estimate mean cell sizes, assuming that dark objects were all cells. Cell volume was estimated by computing the estimations of horizontal and vertical cell sizes (Equation 2-3). A MANOVA revealed a significant variation in cell volume between the inner and the outer cortex tissues ($F = 18.40$, $p = 0.000$), the outer cortex cells being larger than the inner cortex cells, and between the outer cortex of fruit of different sizes ($F = 10.17$, $p = 0.000$). The tissue heterogeneity within apple cultivars reduced the differences between the different apple varieties. The heterogeneity was greater in the inner cortex tissue due to cell elongation and the presence of vascular bundles. Further analysis was therefore focused on the outer cortex. As the thickness of the section was 200 µm (although cell size varied), fruit with small cells had more cell layers, which resulted in underestimation of cell size for such fruit (Figure 2-5C). However, underestimation was limited as the granulometric analysis was based on gray levels.

Figure 2-6 depicts cell volume of the outer cortex region of Fuji cultivar as a function of fruit weight. As the relationship between weight (w) and volume (V) was linear

($w = 1.18 \times V, r^2 = 0.93$), fruit weight was used instead of estimation of fruit volume, the measurement of which was less precise.

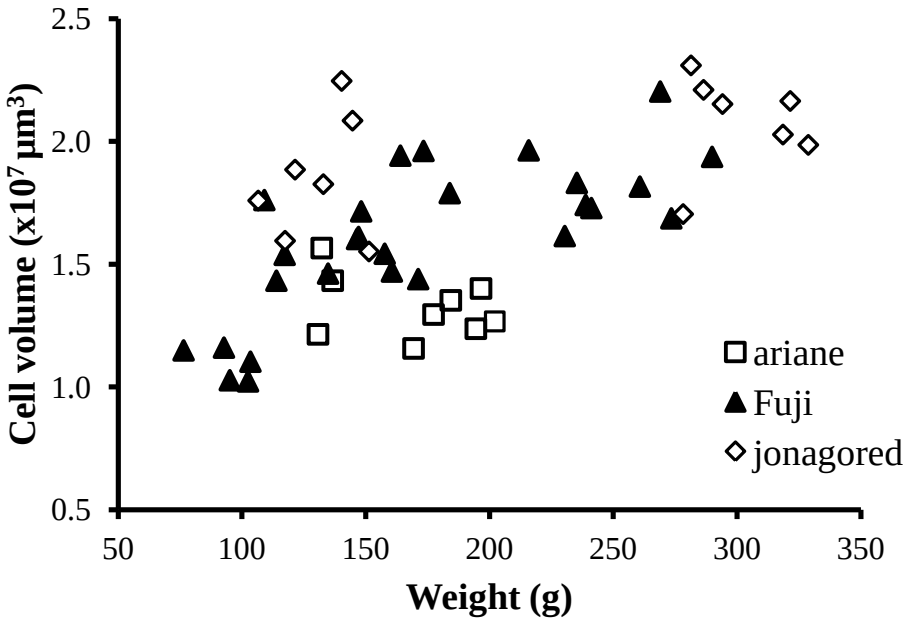

Figure 2-6: Plot of cell volume as a function of fruit weight for the Fuji cultivar.

The relationship between cell size and fruit size depended on the cultivar being studied. Figure 2-6 shows that cell size slightly increased with fruit size only for the Fuji cultivar and in the small and medium fruit range. These results confirm that the size of the fruit can depend on the cell number and size (Harada et al., 2005; Malladi and Hirst, 2010), or on both parameters, and underline the significant dependency of this relationship on cultivars. MANOVA performed only on the Fuji cultivar resulted in an F-value of 20.64, confirming the relationship between cell volume and fruit size. The differences observed could be due different behavior of the cultivars during the stages of division and expansion of cells.

According to Van der Weerd et al. (Van der Weerd et al., 2001) the relaxation rate of the third component ($1/T_{23}$) depends on the vacuole size (Equation 2-1), the latter being approximated by cell size in vacuolated cells. The relationship between $1/T_{23}$ and cell size was investigated for the outer cortex of Fuji cultivar, for which both T_{23} and cell volume differed between apples of different sizes. There was considerable data

dispersion and consequently a relatively weak linear relationship was established ($r^2 = 0.60$). The relatively weak association between $1/T_{23}$ and cell dimensions was at least in part linked to the narrow range of cell sizes found in this study. Indeed, Van der Weerd et al. studied pearl millet and maize stems with approximate cell radii of a few micrometers to a hundred micrometers (factor 20) while the radii of apple cells of this study ranged from 145 µm to 220 µm (factor 1.5). Nevertheless, the intercept of the fitted line in Figure 2-7, corresponding to the bulk T_2 of the vacuole, was about 2.12 s, as expected (T_2 for water at 20°C was 2.08 s) and the slope of the line linked to the magnetization sink strength parameter was $H = 9.0 \times 10^{-5}\, m.s^{-1}$.

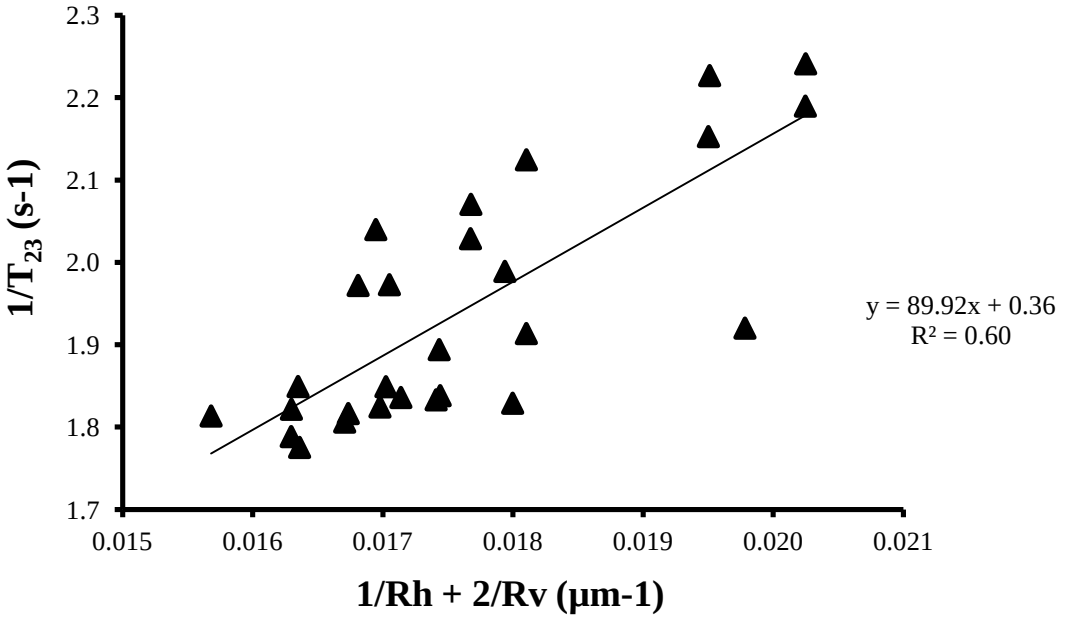

Figure 2-7: Plot of the vacuole compartment-associated T_2 (T_{23}) as a function of cell dimensions for the Fuji cultivar. The linear fit is indicated as a line ($r^2 = 0.60$).

The value of H obtained in this study was higher than the values observed on maize and pearl millet ($2.8 \times 10^{-5}\, m.s^{-1}$ and $4.0 \times 10^{-5}\, m.s^{-1}$, respectively) (Van der Weerd et al., 2001), on Cameron and Quest tomatoes (1.1×10^{-5} and 0.5×10^{-5}, respectively) (Duval et al., 2005) and on Granny Smith cultivar apples (1.0×10^{-5}) (Van As, 2007). However, differences in protocols may be at the origin of these variations. First, Van der Weerd et al. (Van der Weerd et al., 2001) considered the mono-exponential T_2 to be the vacuolar T_2 while the vacuolar T_2 in the present study was

estimated from the multi-exponential relaxation. A T_2 computed with a mono-exponential fit as in Van der Weerd's study resulted in a higher H value ($H_{mono} = 10.0 \times 10^{-5}\, m.s^{-1}$). Furthermore, measurements in the present study were performed on a higher field and with longer TE, thus underestimating T_2 because of the impact of microporosity (Adriaensen et al., 2013; Donker et al., 1996). Using a relationship established between NMR (20 MHz, TE = 0.1 ms) T_2 and MRI T_2 (Adriaensen et al., 2013), new values of H could be approximated: $H_{NMR} = 3.8 \times 10^{-5} \mathrm{m.s^{-1}}$ and $H_{NMR,mono} = 4.0 \times 10^{-5}\, m.s^{-1}$. The latter values are closer to each other than the original values, indicating that the porosity effect on T_2 was corrected. Moreover, the latter values are in the range of H values from previous studies. However, as illustrated by the change in H value between the MRI and NMR methods, it is difficult to compare the values obtained by different methods.

On the other hand, when looking at the whole data set, including both inner and outer cortex data, the relationship between cell dimensions and T_{23} (Equation 2-1) no longer exists even for the Fuji cultivar. This result indicates that variations in T_2 within parenchyma cannot be explained only by changes in cell sizes. Other phenomena may be the causes of these variations (Van As, 2007). For instance, the permeability of cell membranes may vary inside tissues and between cultivars. Further, different plant cell components (sugars, proteins and other macromolecules) may alter relaxation times via chemical exchange (Hills and Duce, 1990). Raffo et al. (Raffo et al., 2005) investigated the relationship between transverse relaxation and changes in chemical composition occurring during ripening of banana fruit. They demonstrated that an increase in T_2 was linked to the decrease in starch concentration, while the increasing sugar concentration produced only minor effects. On the other hand, studies on kiwifruit (Clark et al., 1998a) or Asian persimmon (Clark and MacFall, 2003) did not shown any obvious relationship between the monoexponential T_2 relaxation time and the tested cell solutes. The impact of the chemical composition on the T_2 relaxation has therefore to be elucidated.

IV. CONCLUSION

We demonstrated in this study that a combined quantitative MRI approach based on multi-exponential T_2 and porosity measurements provided better discrimination between tissues than the previous mono-exponential T_2 map approaches. Indeed, multi-exponential fitting allowed investigation of water status and distribution at the subcellular level. Moreover, a reliable interpretation of T_2 was ensured, taking into account tissue porosity. It was also shown that measurements at a relatively low magnetic field (1.5 T) make it more possible to discriminate tissues than measurements performed at a high field where strong effects of magnetic susceptibility prevent reliable T_2 mapping.

Investigating apple fruit on a millimeter scale using mono-exponential T_2 and porosity maps confirmed the heterogeneous structure of apple parenchyma tissue and identified two homogeneous regions in cortex (inner and outer cortex). Differences between the regions were then assessed for all the parameters measured (multi-exponential relaxation times and associated relative amplitudes, apparent microporosity and cell size) for the three cultivars, providing information at the subcellular and tissue level. As relaxation components were linked to cell compartments, these differences were interpreted in terms of modification of the water distribution between the vacuole and the cytoplasm and modification of membrane permeability. Moreover, a difference in the T_2 attributed to the cell wall (T_{21}), observed between cultivars suggests that MRI measurements could be used for the characterization of tissue texture as this might be related to turgor pressure, supported by the cell wall.

Multi-exponential fitting was performed on ROIs in this study. The challenge for better characterization of fruit tissue will be to apply the same approach to individual pixels in order to compute maps corresponding to the T_2 and associated signal intensity of the different components. This would require a higher signal to noise ratio and probably improving the image processing method used.

As mentioned above, specific variations were also observed between cultivars in addition to the relaxation times and porosity distributions inside fruit. The same pre-harvest conditions, maturity at harvest and storage conditions (shown to affect porosity

and relaxation times) for all cultivars would be required to generalize these results. Further investigations will therefore be necessary to assess specific cultivar features.

As T_2 differences were also observed between fruit of different sizes, the results of MRI and histological measurements were compared to investigate the sources of these variations. These showed that variation in cell size might be linked to the vacuole-associated T_2, as correlations were established between cell size and T_{23}. However, compartment size only partially explains the variations in T_2 and several other parameters may be the causes of these variations. Measuring and mapping the diffusion coefficients, as well as measuring concentrations of cell solutes could contribute to the better understanding of the signal.

The MRI mapping of apparent microporosity in this study and determination of the spatially resolved multi-exponential T_2 relaxation demonstrated the high value of these approaches in the non-destructive determination of apple microstructure. These methods will be particularly valuable for the sampling of specific tissues to further investigations into the origins of T_2 contrast and the impact of tissue microstructure on fruit texture.

Acknowledgments: This work was financed in part by the AI-FRUIT Pays de la Loire Research Program. GW was supported in part by a scholarship from the Pays de la Loire and Bretagne regions.

V. SUPPLEMENTARY DATA

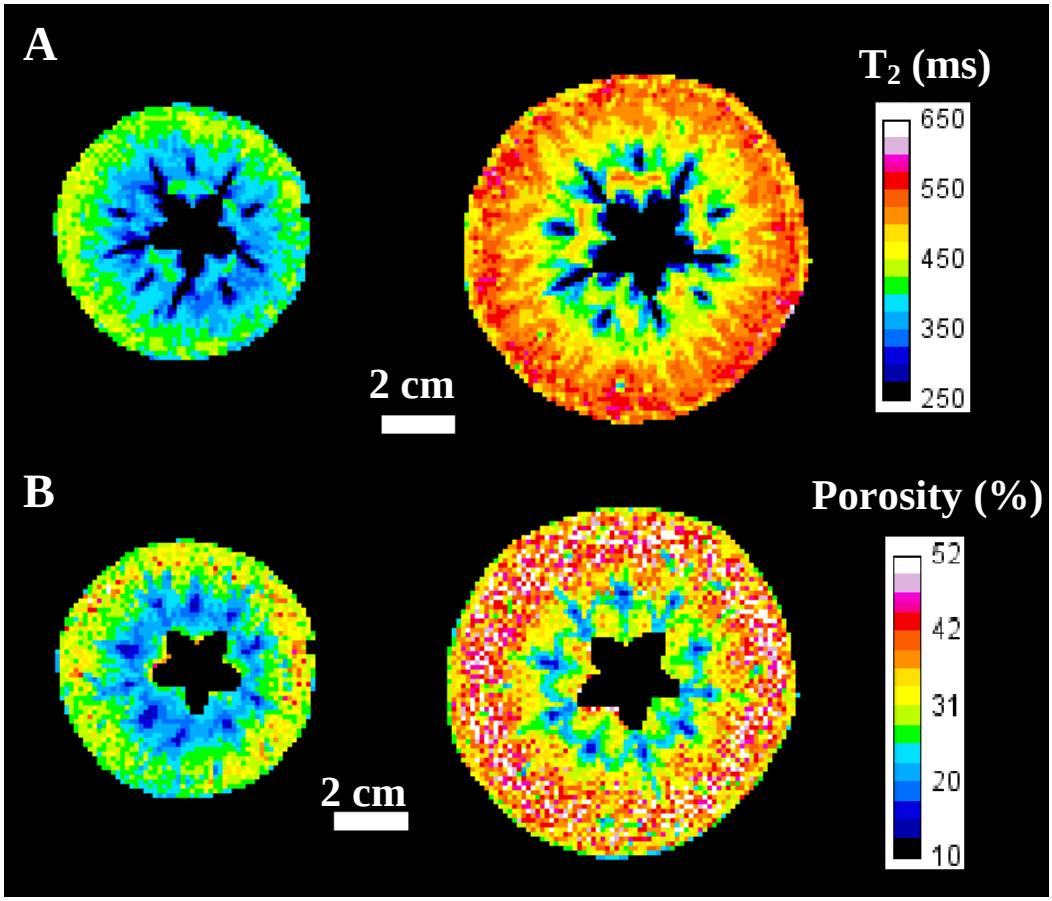

Supplementary Figure 2-8: Monoexponential T_2 (A) and apparent microporosity (B) maps of Jonagored cultivar for the different sizes. The reader is referred to the web version of this article for interpretation of the references to color in this figure legend.

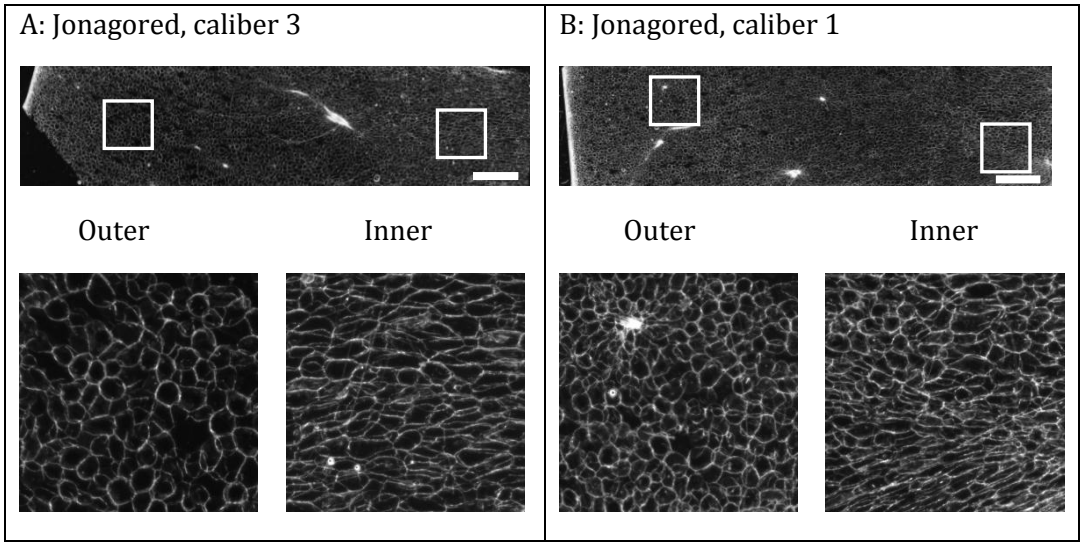

Supplementary Figure 2-9: Macrovision images of two sizes of Jonagored cultivar corresponding to the whole cortex region and zoom-in on regions in the inner and outer cortex as analyzed using granulometric methods. Scale bar is 2 mm.

Chapter 3: Analysis of the dynamic mechanical properties of apple tissue and relationships with the intracellular water status, gas distribution as measured by MRI, histological properties and chemical composition

Guillaume Winisdorffer[a,b], Maja Musse[a,b], Stéphane Quellec[a,b], Adelin Barbacci[b], Sophie Le Gall[c], François Mariette[a,b], Marc Lahaye[c]

[a]IRSTEA, UR TERE, 17 avenue de Cucillé, CS 64427, 35044 Rennes, France,

[b]Université européenne de Bretagne, France,

[c]INRA, UR1268 BIA, Rue de la Géraudière, BP 71627 44316 Nantes Cedex 3, France

3. Analysis of the dynamic mechanical properties of apple tissue and relationships with the intracellular water status, gas distribution as measured by MRI, histological properties and chemical composition

I. INTRODUCTION

The texture of fleshy fruits is of primary concern for the whole production to consumer chain. Texture is defined by several sensory descriptors resulting from the structure of the fruit (Szczesniak, 2002). Apples, the third highest fruit produced in the world (FAO, 2014) have been the subject of many studies focusing on characterizing their texture variations. The fruit softens throughout development (Volz et al., 2003), particularly during ripening and post-harvest storage (Johnston et al., 2002). Moreover, softening and other textural changes vary greatly, depending on storage conditions, the cultivar and harvest date (Brummell, 2006). Flesh juiciness, firmness, crispness and mealiness are the major sensory descriptors of apple texture (Daillant-Spinnler et al., 1996; Jaeger et al., 1998). Several techniques have been proposed to characterize texture, either destructively or non-destructively (Chen and Opara, 2013). In particular, crispness and firmness can be assessed by puncture, compression and tensile tests (Chauvin et al., 2010; Harker et al., 1997a; Mehinagic et al., 2004), and juiciness can be evaluated by a cell integrity test (Harker et al., 1997b). The tissue structure has a significant role as firmness has been linked to apple flesh density (Vincent, 1989) and juiciness to cell size (Harker et al., 1997b). However, correlations between instrumental measurements and sensory descriptors depend on the textural diversity between cultivars; in particular, the links between sensory juiciness and crispness and instrumental juiciness and crispness vary according to cultivar (Brookfield et al., 2011). Mealiness has mainly been assessed by sensory analysis (Harker et al., 2002).

Fleshy fruit have a viscoelastic behavior (Vincent, 2012) that has seldom been studied as such (Abbott, 1999). Dynamic Mechanical Analysis (DMA) is commonly used

to assess the storage and loss moduli characterizing the elastic and viscous behaviors of viscoelastic solids and polymers, respectively, particularly under different temperature conditions (Menard, 1998). DMA has been used to study the impact of temperature on the mechanical behavior of a few plant commodities (Assor et al., 2009; Blahovec and Lahodová, 2012; Blahovec et al., 2013; Wang et al., 2014; Xu and Li, 2014). For example, DMA has been used to investigate the effects of osmotic dehydration and turgor changes in apples and pears (Martinez et al., 2007; Wu and Guo, 2010). Dynamic rheology has been used on potato tubers (Bu-Contreras and Rao, 2002) and apples (Varela et al., 2007). The latter authors used small amplitude oscillatory shear (SAOS) in apples (10 Pa at a frequency of 1 Hz, strain < 0.01%), which was found to complement a compression test (5% strain). Storage (measured by SAOS) and Young's (measured by compression) moduli were correlated and the storage modulus was also correlated with penetrometry, emphasizing the value of such measurement. However, the relationship between properties measured by SAOS and texture remains to be established.

Apple has a very heterogeneous tissue (Herremans et al., 2013; Khan and Vincent, 1990; chapter 2). It is highly porous and its mechanical behavior depends on several factors such as internal turgor pressure, characteristics of water within cell compartments, the mechanical properties and thickness of cell walls, size of cells and pores, and orientation of cells in the tissue (Gao and Pitt, 1991; Konstankiewicz et al., 2001; Oey et al., 2007).

Turgor pressure has been recognized as a fundamental aspect of the mechanical properties of tissue and fruit texture (Bruce, 2003; Lin and Pitt, 1986). This high pressure (about 0.5×10^6 N m^{-2}) is generated by intracellular liquids and is applied to cell membranes and cell walls. High turgor pressure has been linked to elongated cells, resulting in increased bonding between cells and affecting texture. Although the relationship between turgor pressure and the mechanical properties of parenchyma tissue of fleshy fruit depends on the mechanical measurement method (Jackman et al., 1992; Konstankiewicz and Zdunek, 2001; Lin and Pitt, 1986; Oey et al., 2007), an increase in turgor pressure has nevertheless been linked to a higher failure point during mechanical tests (Cybulska et al., 2011; Oey et al., 2007). Despite the link between turgor pressure and cell shape, the impact of turgor pressure on failure strain, failure stress and tissue stiffness has been found to be independent of cell size and shape (Lin

and Pitt, 1986; Oey et al., 2007). Previous studies revealed a link between turgor pressure and apple crispness and juiciness (Oey et al., 2007).

Water status and distribution in plant tissue can be accessed by MRI (Van As and van Duynhoven, 2013). Few studies have looked for correlations between quantitative MRI measurements and mechanical properties of fruit. A combination of compression and juiciness tests was used to assess mealiness in Top Red apples which was found to be related to mono-exponential transverse relaxation time (T_2) (Barreiro et al., 1999). Poor correlations were found between firmness and T_2 in tomatoes (Tu et al., 2007) and apples (Moller et al., 2013), and softening during storage was linked to a change in the distribution of subcellular water in kiwi fruits (Taglienti et al., 2009).

As well as supporting turgor pressure, the cell wall has an important role in the mechanical properties of the tissue. An increase in stiffness of the cell wall results in an increase in stiffness of the tissue (Lin and Pitt, 1986). The mechanical properties of the cell wall rely on its structure and composition (Barbacci et al., 2013; Burgert and Dunlop, 2011). The cell wall of fleshy fruit is composed of three interacting networks of complex polysaccharides (Brummell, 2006; Carpita, 2000; Johnston et al., 2002): cellulose, hemicellulose (matrix glycans) and pectin. Cellulose is organized as stiff hydrogen-bonded microfibrils embedded in a matrix of hemicellulose and pectin. Other macromolecules such as structural proteins and lignin are also present but to a lesser extent. Hemicellulose is typically a neutral sugar backbone with side branches. In particular, the major component is xyloglucan, composed of a glucose backbone with xylose side chains on which galactose and then fucose residues can be linked. Hemicellulose is also called cross-linking glycans due to their function of linking cellulose microfibrils together by establishing hydrogen bonds with them. The pectic matrix in fleshy fruit often represents about 50% of the cell wall (Carpita, 2000) and is located particularly in the middle lamella. It is composed of homogalacturonan (HG), rhamnogalacturonan-I and –II, tied together by their backbone and also linked to hemicellulose according to a current model (Mohnen, 2008). According to the amount and distribution of methylesterification on HG, this structural domain from different chains can dimerize with calcium to create an extended three-dimensional network. The cell wall has to be able to undergo both plastic and elastic deformations during cell growth and life (Burgert and Dunlop, 2011). The functions of pectin, in particular, are

attributed to cell-cell adhesion (Jarvis et al., 2003) and the regulation of cell wall porosity (Fleischer et al., 1999), thus affecting diffusion of solutes in the cell wall. The composition and structure of hemicellulose and pectin are modified during the ripening of fruit. Several hemicellulose-modifying enzymes and proteins such as glucan hydrolase, xyloglucan endotransglucosylase/hydrolase and expansin increase in activity and restructure the hemicellulose-cellulose network (Carpita, 2000). Ripening also involves demethylesterification, depolymerization and solubilization of pectin (De Vries et al., 1984). In fact, an increase in water-soluble pectin content and a decrease in arabinose and galactose content resulting from the debranching of rhamnogalacturonan-I have been found to be linked to fruit softening and cell dissociation (Gwanpua et al., 2014; Knee, 1973; Pena and Carpita, 2004; Yoshioka et al., 1992). Change to a soft melting texture is also associated, in vitro, with a swelling of the cell wall during ripening. Movement of water into cell wall networks accompanies this swelling (Redgwell et al., 1997), the latter highlighting the importance of water and solute distribution between cell compartments.

In addition to cell wall properties and cell water compartmentation linked to turgor pressure and cell wall swelling, the microstructure of the parenchyma of fleshy fruit also affects the mechanical properties of the tissue. The organization and distribution of intercellular spaces between the cells and their number and size contribute to the mechanical properties of apple parenchyma (Ting et al., 2013). These spaces originate from either the breakdown of entire cells or from the separation of cells. They can interconnect and thus their size can increase over time (Esau, 1977) leading to various shapes and sizes of spaces. Firm apples generally have small intercellular spaces whereas larger pores are found in soft fruit (Vincent, 1989). Changes in apparent microporosity, defined as the amount of gas in the tissue in relation to its volume, have also been identified during apple shelf-life (Herremans et al., 2013).

The aim of this study was to characterize the microstructural basis of the viscoelastic mechanical changes in the apple parenchyma on different scales. A multi-instrumental approach was used to assess a number of parameters involved in the mechanical properties of apple tissue. Six contrasting apple cultivars in terms of expected firmness were studied over three to six-month cold storage. MRI was used for measurement of multi-exponential T_2 relaxation parameters characterizing the intracellular water

compartmentation and for estimation of apparent microporosity. Samples of cortex were selected from MRI images and then analyzed by other techniques. Macro-vision imaging was used for histological analysis, the viscoelastic properties of samples were measured by DMA, and chemical analyses were performed to evaluate water content, soluble solid content, cell wall content and cell-wall polysaccharide chemical composition and structure. Parenchyma tissue was selected as main focus because it is the main consumable part of an apple.

II. MATERIALS AND METHODS

1) Fruit

Apples of six different cultivars harvested at maturity (starch test, 7-8 (Vaysse P., 2004)) were studied: three are known to remain firm on storage (Fuji, Ariane, and Granny Smith) and three are known to develop soft or mealy texture (Experimental Cultivar (EC), Florina, and Rome Beauty). All apples were weighed on a digital balance and sorted for weight. The fruit studied comprised twelve Granny Smith, six Ariane, twenty seven Fuji, ten EC, six Florina and three Rome Beauty apples. Three different calibers were differentiated for Fuji (three fruit per caliber, c1, small ~125 g, c2, medium ~185 g, c3, large ~290 g), and the other cultivars were homogeneous in size (Ariane ~185 g, EC ~180 g, Granny Smith ~240 g, Florina ~180 g, Rome Beauty ~220 g).

Measurements were performed at three different times for Fuji, Ariane, EC and Granny Smith apples (one-month (1m), two-month (2m) and three-month (3m) after harvesting). The fruit were stored at 4 °C before and between measurements. For each measurement, three fruit for each cultivar and caliber (apart from Ariane) were scanned by MRI and regions of the outer cortex were selected based on T_2-weighted MRI images Figure 3-1A).

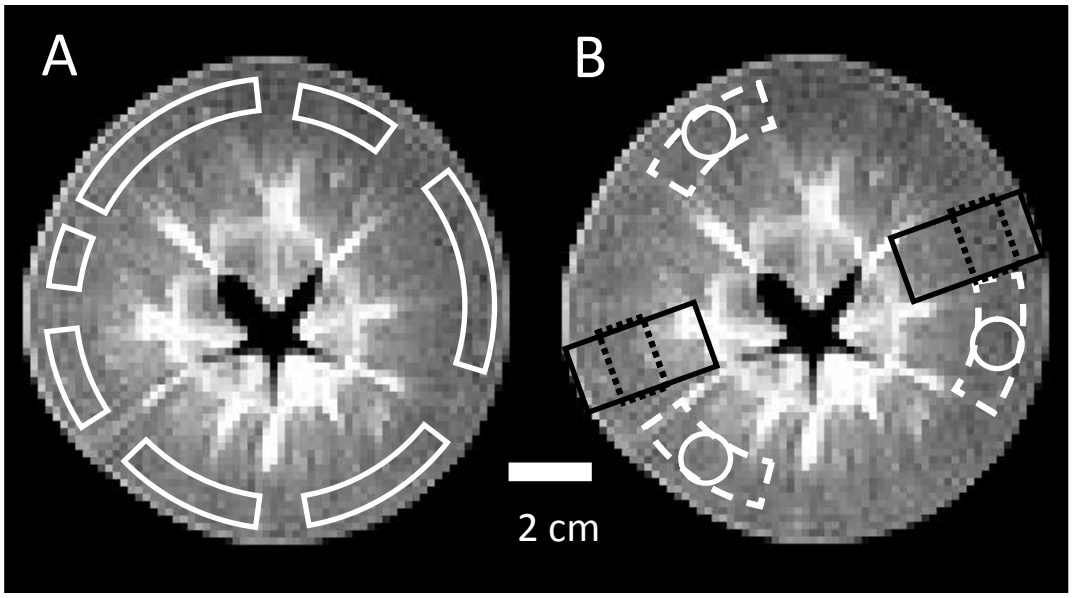

Figure 3-1: MRI T_2 -weighted images at 350 ms showing A) in white the Regions Of Interest (ROIs) in which the mean signal of all voxels (approximately 350) was used for MRI analysis, B) the macro-vision sample (black solid line) and the area analyzed by macro- vision (gray black dotted line), the mechanical sampling areas (white solid line) and the chemical measurement areas (white dotted line).

Measurements for Ariane were performed on one fruit at 1m, two fruit at 2m and three fruit at 3m. In order to ensure analyses on the same tissues, samples were taken from the regions selected on MRI images for mechanical and chemical measurements (Fig. 1B, white solid line for mechanical measurements and white dotted line for chemical measurements), as well as for optical imaging (Fig. 1B, black solid line). To increase the variability of the dataset, supplementary measurements were performed on three Granny Smith apples and one EC apple at six months after harvesting (6m). Moreover, Florina (three fruit) were analyzed at 3m and Florina and Rome Beauty (three fruit each) were analyzed at 6m.

2) MRI

a. Acquisition

MRI measurements were carried out with a 1.5 T MRI scanner (Magnetom, Avanto, Siemens, Erlangen, Germany). The fruit were maintained at a controlled temperature (20 ± 0.5 °C) during acquisitions; they were placed in the Faraday cage of the MRI scanner ten hours before measurement to stabilize the temperature. The median plane

of each fruit (transverse section at middle height of fruit) was imaged with a pixel size of 1.19 mm x 1.19 mm, slice thickness of 5 mm and repetition time of 10 s. The choice of spatial resolution was governed by the trade-off between signal to noise ratio (SNR) of the images and spatial heterogeneity of the apple fruit. Two MRI sequences were performed:

(i) a multi spin echo (MSE) sequence, with the parameters chosen according to (Adriaensen et al., 2013): non-selective refocusing pulse, inter-echo spacing (ΔTE) of 7.1 ms, bandwidth 260 Hz/pixel, 1 scan and 512 echoes per echo train for multi exponential T_2 estimation

(ii) a multi gradient echo (MGE) sequence, with first echo time (TE1) of 2.8 ms and ΔTE of 1.6 ms, bandwidth 1096 Hz/pixel, 12 echoes and 2 scans for T_2* estimation. The parameters were determined in a preliminary study as the trade-off between the shortest echo times (TE1 and ΔTE) and the SNR ratio.

The SNR of the images obtained by the MSE and MGE sequences at the shortest echo time were approximately 120 and 80, respectively.

b. Image processing

The T_2 and T_2* of apple parenchyma were computed on a Region of Interest (ROI, Figure 3-1A) as described above. The ROI-based approach was used as it improved the SNR (Adriaensen et al., 2013). ROIs were selected manually on homogeneous regions of mono-exponential T_2 maps (Figure 3-1A) computed for this purpose using ImageJ software (Schneider et al., 2012). The mean signal over the ROI was computed with TableCurve 2D software (Systat, 2007) for all the MSE images of the series and then fitted according to a tri-exponential decay curve (Equation 2-2, i=3).

$$I(t) = \sum_{i=1}^{n} I_{0i} \times e^{-\frac{t}{T_{2i}}} + const$$

Equation 2-2

where t is the time, I_i the intensity, T_{2_i} the transverse relaxation time of each component of the signal and *const* an offset modeling the background offset. The mono-exponential T_2 of selected ROIs was computed from Equation 2-2 for i=1, and that of T_2* by replacing T_2 by T_2*. Apparent microporosity was then computed from T_2 and T_2* according to Musse et al. (Musse et al., 2010b). The method is based on the fact that differences in magnetic susceptibility between a tissue and air create field inhomogeneities, which induce intravoxel dephasing and associated signal loss in gradient-echo (MGE) images. Signal loss occurring in multi-spin-echoes (MSE) images is drastically lower and can serve as a reference. Indeed, microscopic field fluctuations are responsible for irreversible dephasing characterized by T_2 ($R_2=1/T_2$), and local (mesoscopic) field inhomogeneities contribute to $R_2^{\#}$, the reversible part of R_2* ($R_2^*=R_2+R_2^{\#}=1/T_2^*$). The latter can be used for estimation of apparent microporosity as it originates from internal, tissue-specific sources. T_2 and T_2* are estimated from MSE and MGE sequences, respectively. The error on microporosity due to fitting was about 0.5%. , a discussion on this error is made in the appendix of this work.

More details about MRI measurements and numerical simulations of T_2 and T_2* signals used for estimation of the errors in computing multi-exponential T_2 relaxation parameters and apparent microporosity are given in Appendix.

3) Mechanical measurements

A 1 cm thick slice was cut from each fruit, corresponding to the slightly enlarged MRI slice. For each fruit, three cylindrical samples were taken from the cortex at the same distance from the cuticle as the homogeneous regions on the MRI maps (Figure 3-1B, solid lines). The samples (4 mm in radius (R_0) and 8 mm in height (L_0)) were subjected to DMA (Bose, ElectroForce 3100). Each sample underwent a 1 Hz oscillating displacement between 3% and 7% of its height within the elastic domain. Both the force (F) and the deformation (D) were recorded. The stress, defined as the force exerted by the device per surface unit, was computed by $\sigma=F/(\pi R_0^2)$. The strain, representing the deformation of the sample, was computed by $\varepsilon=D/L_0$

The mechanical strain applied to the sample is written as $\varepsilon = \varepsilon_0 \sin(\omega t)$ where ε_0 is the

maximum strain amplitude and $\omega=2\pi f$ the pulse as a function of the oscillation frequency. The resulting mechanical stress in the sample is written as $\sigma= \sigma_0 \sin(\omega t+\delta)$ where σ_0 is the amplitude of the stress signal and δ the delay between the strain and the stress due to the viscoelastic behavior of the material. The number of compression cycles was automatically optimized by mechanical testing machine software (Bose WinTest) in order to accurately compute dynamical stiffness and damping.

Automated DMA data analysis (Bose DMA Analysis 7) allowed direct computation of the dynamic stiffness of the sample $k = F^*/D^*$ i.e. the ratio between peak-to-peak force amplitude and peak-to-peak displacement. The ratio k was used to express Young's modulus E ($E = k.L_0/\pi R_0^2$). The damping of the material was expressed as tan δ.

The elastic (E) and viscous (tan δ) behaviors are *a priori* independent mechanical parameters. Consequently, they were treated as independent variables in statistical analyses.

4) Macrovision Imaging

a. Image acquisition

The samples taken for optical imaging (Figure 3-1B, black line) were imaged as described in detail in previous chapter (chapter 2): the sampling protocol consisted of cutting a 1 cm slice at the equator of the fruit, corresponding to twice the thickness of the MRI virtual slice. Sections 200 µm thick were cut from the middle of each slice using a vibrating blade microtome (MICROM, HM 650V, Microm International GmbH, Walldrof, Germany) and these were then imaged under water using a macro-vision system (Devaux et al., 2008). The camera and lens were adjusted to observe a 10.7 mm x 14.4 mm area and images were digitized in 1620 x 1220 pixels (pixels of 3.6 µm x 3.6 µm).

b. Image processing

ROIs selected in the parenchyma at the same distance from the cuticle as homogeneous regions on MRI maps (Figure 3-1B, dotted lines, gray) were analyzed visually for texture according to both black objects morphology and arrangement as

explained in detail in previous chapter (chapter 2). Gray level granulometric methods (Devaux et al., 2008) were applied to extract information concerning black objects distribution and dimensions. Granulometric curves of gray levels were constructed by varying the sizes of horizontal and vertical linear structuring elements, allowing analysis of cell dimensions in both directions. As they were based on variations in gray level of pixels, granulometric curves did not measure the actual black objects dimensions but a combination of objects dimensions and gray levels. It should be emphasized that these objects correspond to both cell lumens and intercellular spaces. The image resolution and image analysis algorithm used made the distinction of the two types of structure impossible. Black objects were assumed to be mainly representative of cells and their physical characteristics were used to approximate that of cells. Cell volume was then estimated by considering the black objects observed to be cylinders with the height (h) radial to the cuticle and the radius (r) parallel to the cuticle: $V = \pi r^2 \times h$. With all the above limits in the analyses, dimensions and volumes of objects attributed to cells were therefore subject to uncertainty but provided a convenient mean of estimating the physical characteristics of tissue cellular structures.

5) Chemical analyses

Chemical analyses were performed on the samples as described in the Materials and Methods (Figure 3-1B, white dotted lines).

a. Water Content

Water content (WC) in samples was expressed according to the weight difference between fresh and freeze-dried samples (Cosmos, Cryotec, Saint-Gély-du-Fesc, France).

b. Polysaccharide composition and structure of cell walls

Cell wall preparation

Apple parenchyma cell walls were prepared as Alcohol Insoluble Materials (AIMs) using an automated extraction method with an accelerated solvent extraction unit ASE® 350 (DIONEX, CA, USA). Approximately 500 mg of frozen apple flesh were freeze-dried, and then dried at 40 °C overnight under vacuum over P_2O_5. The dried material was ground into fine powder using a FastPrep-24 instrument (MP Biochemicals, CA) at a speed of 6.5 $m.s^{-1}$ for 60 s. Samples (500 mg) were extracted using 80% ethanol at a flow rate of 2 mL min^{-1} in 22 mL cells of ASE 350. The conditions for the ASE extraction were set at 100 °C with a flow time of 6 min, followed by a rinse with a volume of 150%, and a purge time (N_2) of 30 s. AIMs were dried at 40 °C overnight under vacuum over P_2O_5 before grinding and weighing. Soluble solid content was computed as the difference between freeze-dried apple flesh and AIMs.

Cell wall sugar composition

Identification and quantification of neutral cell wall sugars were performed by gas-liquid chromatography (GC) after degradation in sulfuric acid (Hoebler et al., 1989). AIM were dispersed in 13 M sulfuric acid for 30 min at 30 °C and then hydrolyzed in 1 M sulfuric acid (2 h, 100 °C). Sugars were converted to alditol acetates (Blakeney et al., 1983) using an automated procedure with a SwingXL workstation (Chemspeed® technologies AG) and chromatographed on a DB 225 capillary column (Trace GC Ultra, Thermofisher; temperature 205 °C, carrier gas H_2). Standard sugar solutions and inositol as internal standard were used for calibration. Uronic acids in acid hydrolyzates were quantified using the metahydroxydiphenyl colorimetric acid method (Blumenkrantz and Asboe-Hansen, 1973).

Degree of methyl esterification of uronic acids

The degree of methylesterification (DM) and the acetic acid content of pectins were evaluated by HPLC following the procedure described by Levigne et al. (Levigne et al., 2002) AIM (5 mg) was saponified in 1 mL of 0.5 M NaOH at 4 °C for 1 h. HPLC was carried out on a C18 (4 mm × 250 mm, Lichrospher 100 RP-18e (5 µm), Interchim,

France) column thermostated at 25 °C using a refractometric detector (Waters, 2414). An isocratic elution of 4 mM H_2SO_4 was used at a flow rate of 1.0 mL min^{-1}. The DM was calculated as moles of methanol per mol of galacturonic acid. Standard methanol, acetic acid and isopropanol as internal standard were used for calibration.

Enzymatic profiling of cell wall polysaccharides

Cell wall material (5 mg) was suspended in 1 mL acetate buffer (5 mM, pH 5) or water and degraded by laboratory prepared pectin lyase (0.55 nmol s^{-1}, (Ralet et al., 2012)) or commercial endo-1,4-β-glucanase from *Trichoderma longibrachiatum* (Megazyme, Bray, Ireland; 20U) overnight at 40 °C under agitation. The supernatant solution after centrifugation (10 min, 12000 g) of the hydrolyzates was heated for 10 min in a boiling water-bath to inactivate enzymes. Commercial glucanase is known to contain low activity degrading xylan, (galacto)glucomannan and pectic galactan (Lahaye et al., 2012b).

Oligosaccharides in the hydrolyzates were analyzed by MALDI-TOF MS in the positive mode using an Autoflex III MALDI-TOF/TOF spectrometer (Bruker Daltonics, Bremen, Germany) equipped with a Smartbeam laser (355 nm, 1000 Hz). Samples were mixed with the ionic liquid matrix DMA/DHB, which was prepared and used as previously reported (Ropartz et al., 2011). Three replicates per hydrolysis were prepared. The instrument was externally calibrated using galactomannan oligomers (DP 3-9) of known mass.

Spectra (total of 3 MS replicates) were recorded in the mass range m/z 600-2000. Spectra were exported to Flex Analysis 3.0 software (Bruker) and pre-processed. Mass lists reporting m/z (monoisotopic masses, after deisotoping with the SNAP algorithm, Bruker) and intensities of detected ions were then exported to R software (R Core Team, 2013) for statistical analysis and graphical representation. Ion masses and intensities on the glucanase spectra were normalized to that of the XXXG ion, whereas the peak at m/z 783.191 attributed to DU4m4 (see below for nomenclature) was used for pectin-lyase spectra.

Identification of ions was performed by comparison with the m/z list of theoretical masses of the sodium adduct of different oligosaccharides.

For oligo-uronides released by pectin-lyase, this list took into account the specificity of the enzymes described (Ralet et al., 2012). In particular, because several

oligosaccharide structures have similar m/z values due to substitutions by methyl and acetyl esters and by different ion adduct forms (Na - H on acidic functions and potassium), MS ions were attributed according to methyl esterification per oligosaccharide (i.e. DP3: 1 to 3 methyl esters, DP4: 2 to 4, DP5: 2 to 5, DP6: 3 to 6 and DP7: 4 to 6) and a maximum of 1 to 2 acetyl groups depending on the degree of polymerization (DP3 to 5: 1 acetyl, DP 6 and 7: 2 acetyl groups). The intensity of different adducts for the same oligosaccharides was added.

For oligomers released by the commercial glucanase, ion attribution to xyloglucan structures was performed on the basis of combinations of hexose, methyl-pentose, pentose and acetyl ester substituents.

The oligosaccharide nomenclature used was as follows. For polyuronides the letter U corresponded to uronic acid. The subsequent number referred to the number of residues in the oligomer (i.e. DP). Acetyl and methyl ester substitutions were referred to as a and m, respectively, followed by the number of groups. Unsaturation of the uronic acid at the non-reducing end of the oligomer released by pectin-lyase was referred to as D. According to this nomenclature, DU4m4 refers to an oligo-hexouronide of DP4 fully methyl esterified and unsaturated at the non-reducing end.

The nomenclature of oligomers released by glucanase followed that of Fry et al. (Fry et al., 1993) for xyloglucans. Briefly, bare (1,4)-linked β-D-glucose residues were noted G. Extension of glucose by (1,6)-linked α-D-xylose was noted X. Further extensions on the xylose residues on O-2 by β-D-galactose or α-D-fucosyl-(1->2)-β-D-galactose were noted L and F, respectively. Acetyl-esterification of structures was noted a followed by the number of substituent groups.

6) Statistics

The whole dataset apart from cell wall measurements (cell volume, elongation factor, I_{01}, I_{02}, I_{03}, T_{21}, T_{22}, T_{23}, apparent microporosity, damping factor, Young's modulus, water content, soluble solid content, alcohol insoluble material) was considered for multiple factor analysis of variance (MANOVA). Cultivar and storage time were considered as factors. Statistical analyses were performed with Statgraphics (StatPoint Technologies, 2010).

Principal component analyses (PCA) were also performed on the same data using R (R Core Team, 2013).

III. RESULTS AND DISCUSSION

In order to reduce any bias due to inhomogeneity of apple tissues, the same parenchyma regions selected from MRI images (Figure 3-1) were used for all other measurements performed on Fuji, Ariane, Granny Smith and EC apples at 1m, 2m and 3m.

1) Macro-vision imaging

The mean cell diameter, measured by optical imaging, was about 180 µm. It was within values observed for other apple parenchyma tissue such as Gala, (Malladi and Hirst, 2010), Jonagored (Oey et al., 2007) and apple progenies (Galvez-Lopez et al., 2011). Cell volume, estimated from cell diameter, and elongation factor are presented in Table 3-1A with the statistics regarding cultivar differences.

Table 3-1: Mean values and standard deviations of A) volume and elongation factor calculated from black objects observed on macro-vision images for each cultivar after one-month (1m), two-month (2m) and three-month (3m) storage, B) Young's modulus and damping factor measured for each cultivar after one-month (1m), two-month (2m) and three-month (3m) storage. Results of 99% multiple range tests on each variable for the whole fruit sample are also presented.

A

	Volume ($x10^6$ µm^3)				Elongation factor			
Cultivar	1m	2m	3m	Stat	1m	2m	3m	Stat
Ariane	3.7 ± 0.2	4.2 ± 0.2	4.2 ± 0.3	a	1.04 ± 0.02	1.05 ± 0.00	1.07 ± 0.04	b
Fuji (c1)	3.5 ± 0.2	5.1 ± 0.7	4.4 ± 0.6	a	1.06 ± 0.03	1.05 ± 0.01	1.04 ± 0.03	a,b
Fuji (c2)	5.1 ± 0.6	5.9 ± 0.6	5.1 ± 0.4	b	1.03 ± 0.04	1.01 ± 0.02	1.02 ± 0.02	a,b
Fuji (c3)	6.1 ± 0.9	5.6 ± 0.3	5.7 ± 0.4	b	0.99 ± 0.02	1.03 ± 0.02	1.04 ± 0.03	a
EC	3.9 ± 0.6	3.9 ± 0.7	3.8 ± 0.2	a	1.04 ± 0.02	1.07 ± 0.04	1.05 ± 0.01	a,b
Granny Smith	5.3 ± 1.4	5.0 ± 0.4	5.4 ± 0.3	b	1.04 ± 0.02	1.05 ± 0.02	1.06 ± 0.02	a,b

B

	Young modulus (N × 10^6 N m^{-2})				Damping factor			
Cultivar	1m	2m	3m	Stat	1m	2m	3m	Stat
Ariane	4.47 ± 0.02	4.53 ± 0.24	3.05 ± 0.54	c	0.099 ± 0.002	0.110 ± 0.002	0.118 ± 0.005	a,b
Fuji (c1)	3.55 ± 0.56	3.06 ± 0.70	2.50 ± 0.19	b	0.106 ± 0.003	0.109 ± 0.005	0.113 ± 0.001	a,b
Fuji (c2)	3.48 ± 0.64	3.48 ± 0.15	2.49 ± 0.38	b	0.105 ± 0.004	0.103 ± 0.007	0.105 ± 0.006	a
Fuji (c3)	4.00 ± 0.71	2.77 ± 0.13	3.16 ± 0.10	b,c	0.110 ± 0.002	0.120 ± 0.002	0.113 ± 0.004	b
EC	1.86 ± 0.18	1.58 ± 0.28	1.42 ± 0.05	a	0.120 ± 0.006	0.136 ± 0.014	0.132 ± 0.005	c
Granny Smith	3.25 ± 0.06	2.82 ± 0.16	2.65 ± 0.25	b	0.116 ± 0.003	0.118 ± 0.004	0.112 ± 0.002	b

Variations in volume were high, as it varied between 3.7 and 6.1 x10^6 µm^3, and standard deviations were high (between 5 and 15%). Two groups could be constituted on the basis of the volume at the first measurement time: 1) EC, Ariane and c1 Fuji (small fruit) with objects volume of 3.5 to 3.9 x10^6 µm^3 (Table 3-1A, statistics group a) and 2) c2 and c3 Fuji (medium and large fruit) and Granny Smith with objects volume of 5.1 to 5.7 x10^6 µm^3 (Table 3-1A, statistics group b). These variations could be explained by fruit size as previously reported for Fuji and Royal Gala cultivars (Volz et al., 2004; chapter 2). Indeed, fruit in the first group were of small to medium calibers (100-190 g), while fruit in the second group were of medium to large calibers (150-250 g). The variations over time were not significant for most cultivars except for c1 Fuji, but in this case the variations were probably due to high heterogeneity between samples.

Elongation factors were very close to 1 for all cultivars and did not vary over time. Assuming that these objects represented mostly parenchyma cells, this result is consistent with the fact that the outer cortex is known to have fairly round cells which tend to elongate toward the center of the fruit (Khan and Vincent, 1990). The size distributions of the objects attributed to cells in the sampling areas were thus homogeneous, indicating that the sampling protocol allowed comparison of similar tissue regions in the different cultivars.

2) Mechanical measurements

Mechanical characteristics of apple parenchyma tissue are known to vary with the location and orientation of the flesh sampled likely due in part to histological features (Abbott and Lu, 1996). In the present study, the mean Young's modulus measured on samples taken in the outer cortex area (Figure 3-1) varied between about 1 and 5 × 10^6 N m^{-2}, going from very soft to very firm apples (Table 3-1B).

These results are slightly higher than those reported in a previous study on several cultivars sampled in similar cortex area as ours in which the modulus measured by force displacement on various cultivars ranged from 0.5 to 2 × 10^6 N m^{-2} (Costa et al., 2012) although the minimum modulus was similar. In this study, EC had a significantly lower Young's modulus (Table 3-1B, statistics group a) than the other cultivars, and Ariane had

the highest (Table 3-1B, statistics group c). The Young's modulus and the storage modulus for all cultivars decreased with storage time as previously measured by Small Amplitude Oscillatory Shear on Granny Smith and Golden Delicious cultivars (Costa et al., 2012; Varela et al., 2007). Moreover, previous studies reported a decrease in firmness measured by sensory analysis (Gwanpua et al., 2014; Harker and Hallett, 1992; Johnston et al., 2002). The damping factor (tan δ) was significantly higher for EC (Table 3-1B, statistics group c) than for other fruits (Table 3-1B, statistics groups a and b). Unlike Young's modulus, variations in the damping factor were not significant over the three-month storage. The size of objects estimated by macro-vision and attributed to cells was not correlated with the two dynamic mechanical measurements. This result indicated that the contribution of intercellular spaces in the dark objects dimension likely altered the approximation of cell size that may have otherwise impacted tissue cell density and consequently, Young's modulus (Vincent, 1989). Alternatively, differences in cell turgor pressure and/or cell wall mechanical characteristics between samples may have dominated cellular density effect on Young's modulus.

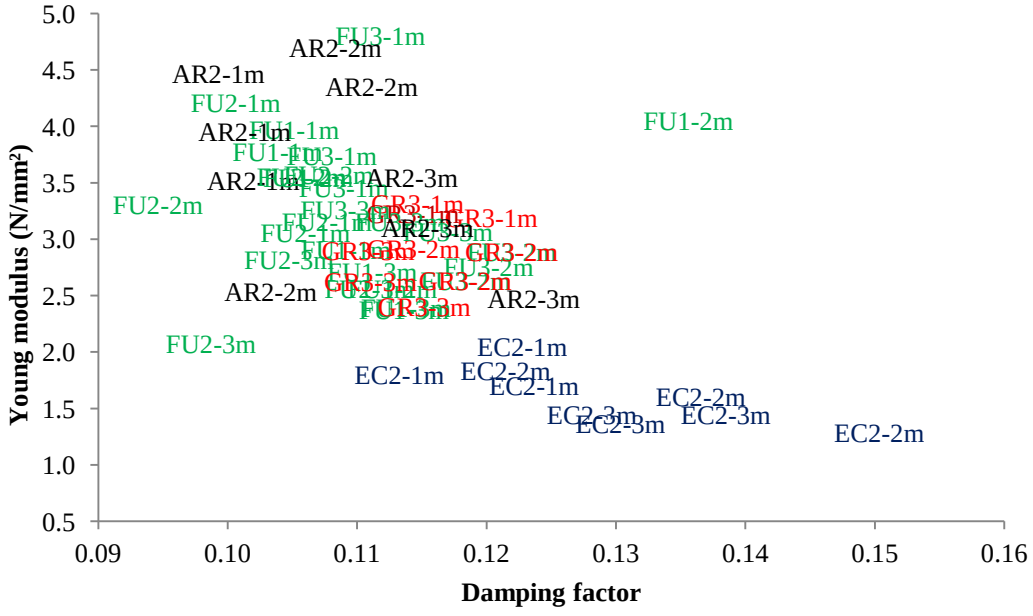

Figure 3-2: Plot of the relationship between Young's modulus and damping factor. Different cultivars are shown in different colors (web version). FU = Fuji cultivar, AR = Ariane, GR = Granny Smith and EC = Experimental Cultivar. The storage time is indicated for each sample as 1m = 1 month, 2m = 2 months, 3m = 3 months.

Figure 3-2 shows a plot of the Young's modulus as a function of the damping factor, demonstrating the relationship between the two measurements with a Pearson correlation coefficient of $r_{E'/\tan(\partial)} = -0.61$: the stiffer the fruit, the less energy lost due to viscous behavior. This correlation between these *a priori* independent parameters has already been reported in wood (Bremaud et al., 2011). This relation likely appears as a specificity of the tissue but awaits a satisfactory molecular explanation. The plot also shows that the correlation comes mainly from cultivar differences and that it is affected by the considerable variability of the mechanical properties of fruit of the same cultivar and by the storage time. For example, after two-month storage, the Young's modulus of Ariane varied between 2.5×10^6 N m^{-2} and 4.5×10^6 N m^{-2} and the damping factor of EC varied between 0.12 and 0.15. These variations may have originated from pre-harvest differences, such as the location of the trees, the position of the fruit on the tree, etc.

3) MRI measurements

a. Apparent microporosity

Variations in apparent microporosity computed from the MRI measurements are presented in Fig 3A. EC had the highest apparent microporosity (about 60%, Figure 3-3A statistics group e), followed by Granny Smith (50%, Figure 3-3statistics group d), while the microporosity of Fuji was the lowest (30 to 45%, Figure 3-3A statistics groups a to c). The slight increase in apparent microporosity with fruit size has already been reported for Fuji (chapter 2). Large data dispersion within cultivars occurred due to pre-harvest and sampling conditions (see above).

Previous studies measuring apparent microporosity by X-ray microtomography or histology reported values from 18 to 28% for Braeburn apples (Herremans et al., 2013; Ting et al., 2013), of 17% for Jonica (Schotsmans et al., 2004), 29% for Fuji and Golden Delicious, and 17% for Jazz (Ting et al., 2013). In the present study, apparent microporosities in outer cortex of small and medium/large Fuji fruit were 32% and 39%, respectively. As discussed in previous study (chapter 2), comparison of microporosity values from different experiments is difficult. First, microporosity values depend on the measurement techniques and the associated data processing method

used (Mendoza et al., 2007; Verboven et al., 2008; chapter 2). Secondly, the physiological status of the fruit and the regions taken into consideration for quantification differ between studies. The highest values of apparent microporosity in this study were surprisingly high compared to the ones obtained in other studies (Herremans et al., 2013; Ting et al., 2013). This could be explained by the measurement method itself (Musse et al., 2010b) that probably reached its limits for these highest microporosities and overestimated the true values. However, although measurements of the highest apparent microporosities are subject to uncertainty, the values reflect nevertheless differences between the different cultivars and storage times.

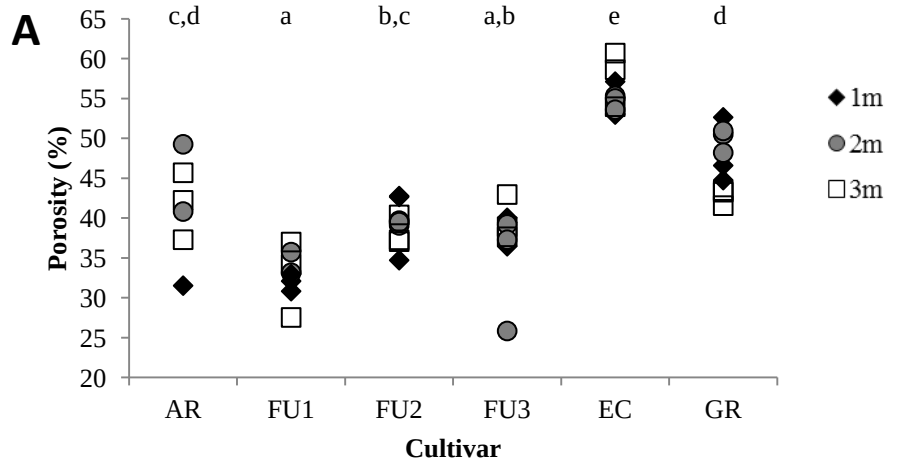
A
c,d
a
b,c
a,b
e
d
Porosity (%)
65
60
55
50
45
40
35
30
25
20
AR
FU1
FU2
FU3
EC
GR
Cultivar
1m
2m
3m

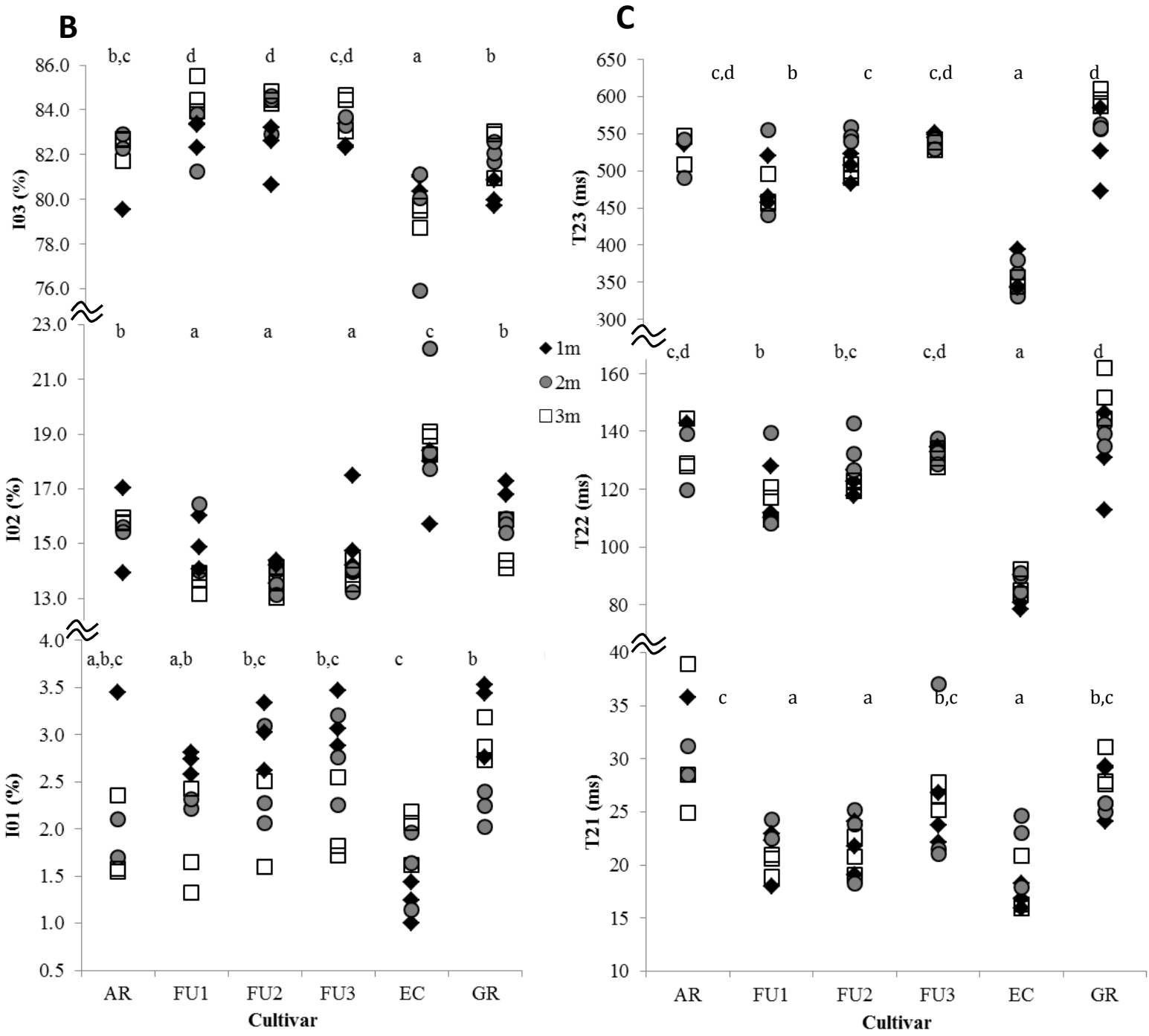
B
C
I03 (%)
I02 (%)
I01 (%)
T23 (ms)
T22 (ms)
T21 (ms)
AR
FU1
FU2
FU3
EC
GR
Cultivar
1m
2m
3m

Figure 3-3 : Plots of A) apparent microporosity in relation to fruit cultivars, B) relative intensities in relation to fruit cultivars, C) relaxation times in relation to fruit cultivars, representing each fruit measured, with results of 99% multiple range test above each value plotted.

b. Relaxation times and associated relative signal intensities

The mean MRI signal intensity measured as a function of the echo time on homogeneous ROIs fitted well with a tri-exponential T_2 decay for all fruit (Figure 3-3). Generally, the first component (about 2.5% of the signal intensity) had a T_{21} relaxation time of about 25 ms. The second component (representing 15-20% of the signal) had a T_{22} relaxation time of about 90-140 ms and the third (about 80% of the intensity) had the highest T_{23} relaxation time of 350-500 ms. The fitting errors were about 4 ms for T_{21}, 3 ms for T_{22} and 1 ms for T_{23}, and about 0.3% for I_{01}, I_{02} and I_{03}. These relaxation times correspond to the previous range of MRI measurements (Adriaensen et al., 2013).

The EC cultivar differed from the other cultivars, the two longest relaxation times being shorter. Indeed, a shorter T_{23} (Figure 3-3C, statistics group a) than other cultivars (358 ± 15 ms versus values over 500 ms for the others, Figure 3-3C, statistics groups b to d) was observed. The same was observed for T_{22} (87 ± 4 versus values over 130 ms). Standard deviations for the variations observed on T_{21} were wide. Ariane had the longest T_{21} (30 ± 5 ms, Figure 3-3C, statistics group c) and Fuji c3 (24 ± 2 ms) as well as Granny Smith (28 ± 2 ms) had intermediate T_{21} values (Figure 3-3C statistics groups b, c). No significant variation in the relaxation times over storage time was observed for any cultivar. On the other hand, the longest relaxation time increased with fruit caliber for Fuji, in accordance with the results of previous studies (Van der Weerd et al., 2001, chapter 2) in which the relationship between cell size and the mono-exponential/ longest relaxation time was demonstrated. The same effect could explain the higher relaxation times of the Granny Smith cultivar. However, the longer relaxation time of the Ariane cultivar could not be explained by the variation in the size of objects attributed to cells from macro-vision and reflected a different cell structure. The shorter relaxation time for EC was not explained by objects' size either and might also reflect a different cell structure or an effect of microporosity.

When calculating relative intensities (Figure 3-3B), a lower I_{03} (80%, Figure 3-3B, statistics group a, versus 82-84%, statistics groups b to d) and a higher I_{02} (19%, Figure 3-3B statistics group c, versus 13-15%, statistics groups a and b) were observed for EC.

I_{03} for Granny Smith (82%, b) and Fuji (84%, c and d) were also significantly different. Variations in relative intensities occurred during storage. For EC, I_{03} decreased while I_{01} increased. For other cultivars, the opposite was observed. There were no significant variations due to fruit caliber for any of the relative intensities.

NMR relaxation times are related to the mobility of water and affected by the chemical exchange of water protons with macromolecules and solid surfaces, and the diffusional exchanges between compartments (Hills and Duce, 1990; Van As, 2007). The transverse relaxation time is used for plant cell investigations as its multi-exponential relaxation makes it possible to monitor changes in the compartmentalization of cells (Van As, 2007). Three or four T_2 components have been obtained by NMR measurements in apples and they have been assigned to the vacuole, cytoplasm and extracellular water/cell wall (Hills and Remigereau, 1997; Snaar and Van as, 1992). The results of the present study are discussed according to this model.

Table 3-2: Pearson correlation coefficients calculated between MRI parameters (I_{01}, I_{02}, I_{03}, T_{21}, T_{22}, T_{23}, apparent microporosity).

	T21	T22	T23	I01	I02	I03	Apparent microporosity
T21	1.00						
T22	0.68	1.00					
T23	0.58	0.98	1.00				
I01	0.41	0.62	0.58	1.00			
I02	-0.13	-0.58	-0.69	-0.21	1.00		
I03	-0.02	0.35	0.48	-0.16	-0.93	1.00	
Apparent microporosity	-0.16	-0.48	-0.52	-0.34	0.77	-0.65	1.00

Considering the Pearson correlation coefficients between MRI data (Table 3-2), a very strong positive correlation ($r_{T22/T23} = 0.98$) was observed between T_{23} and T_{22}, meaning that the two water pools are closely related. The link between the two relaxation times (and thus, according to the model, the two compartments) was independent of the cultivar. Moreover, I_{02} and I_{03} ($r_{I02/I03} = -0.93$) were also strongly correlated, indicating a link between water distribution in the vacuole and in the cytoplasm for all cultivars. This correlation agreed with the hypothesis of water exchange between the two compartments and showed that a higher value of I_{03} led to a

lower value for I_{02}. Correlations were also observed between T_{21} and the other two relaxation times ($r_{T21/T22} = 0.68$ and $r_{T21/T23} = 0.58$), emphasizing that the cell wall also interacted with other compartments. On the other hand, I_{01} was not correlated with other relative intensities, which may be due to the wide dispersion observed (0.5%, see above). Apparent microporosity was positively linked to I_{02} ($r_{porosity/I02} = 0.77$) and negatively to I_{03} ($r_{porosity/I03} = -0.65$), and to a lesser extent to T_{23} attributed to the vacuole ($r_{porosity/T23} = -0.52$). MRI measurement is affected by microporosity as microporosity increases the relaxation rate during measurement (Donker et al., 1996): the higher the microporosity, the greater the effect and the shorter the relaxation time. This effect also depends on the echo time used for the measurement (Adriaensen et al., 2013). The differences between the T_2 observed may thus have been accentuated by a microporosity bias. Intensities are also affected by microporosity, I_{03} being lower and I_{02} higher for high microporosity (Adriaensen et al., 2013) but the microporosity effects remain minor when compared to other effects which were greater on relaxation times (chapter 2): despite wide differences in apparent microporosity, T_2 and intensity ranges were not different. For example, an apparent microporosity of 28% in the Jonagored cultivar corresponded to a T_{23} of 465 ms and a I_{03} of 78% while an apparent microporosity of 42% in the Ariane cultivar corresponded to a T_{23} of 531 ms and a I_{03} of 80%. Nevertheless, for the highest apparent microporosity measured (EC) we suspected an effect of microporosity on T_2 and intensities, as a lower I_{03} and T_{23} and a higher I_{02} were observed.

4) Chemical analyses

Water content (WC), soluble solid content (SSC) and alcohol insoluble material (AIM) in parenchyma samples are reported as a fraction of the fresh weight (Table 3-3).

Table 3-3: Mean values and standard deviations of water content, alcohol insoluble material, and soluble solid content for each cultivar after 1-month (1m), 2-month (2m) and 3-month (3m) storage. Results of 99% multiple range tests on each variable for the whole fruit sample are also presented.

	Water content (WC, %)				Alcohol insoluble material (AIM, %)				Soluble solid content (SSC, %)			
Cultivar	1m	2m	3m	Stat	1m	2m	3m	Stat	1m	2m	3m	Stat
Ariane	81.7 ± 0.0	82.3 ± 1.7	81.4 ± 1.4	a	2.2 ± 0.9	2.6 ± 0.9	2.5 ± 0.5	b	16.4 ± 4.2	18.5 ± 0.6	15.5 ± 1.2	c
Fuji (c1)	83.8 ± 2.3	82.9 ± 1.9	81.8 ± 0.7	a,b	1.4 ± 0.3	1.9 ± 0.4	1.4 ± 0.6	a	12.7 ± 1.6	19.8 ± 1.9	12.8 ± 5.1	a,b,c
Fuji (c2)	81.9 ± 0.5	83.2 ± 0.4	82.6 ± 0.9	a,b	1.6 ± 0.3	1.6 ± 0.1	1.4 ± 0.2	a	14.1 ± 2.1	17.8 ± 0.7	16.1 ± 0.7	b,c
Fuji (c3)	82.8 ± 0.8	82.2 ± 0.8	83.6 ± 0.9	b	1.5 ± 0.3	1.5 ± 0.1	1.5 ± 0.3	a	14.3 ± 0.6	18.7 ± 0.6	15.3 ± 3.9	b,c
EC	85.9 ± 0.9	84.9 ± 1.5	86.6 ± 0.2	c	1.7 ± 0.3	1.3 ± 0.2	1.7 ± 0.2	a	12.1 ± 0.2	15.9 ± 1.3	11.6 ± 0.3	a
Granny Smith	84.1 ± 0.3	84.3 ± 0.5	84.8 ± 0.2	c	2.5 ± 0.4	1.9 ± 0.1	1.9 ± 0.2	b	12.5 ± 1.8	15.5 ± 0.6	13.4 ± 0.2	a,b

The WC ranged between 79% and 87% and was highest for EC (about 85%, Table 3-3, statistics group c) and Granny Smith (about 84.5%, Table 3-3, statistics group c). Fuji and Ariane had similar water content and no significant variations were observed with fruit caliber or storage time. These values were consistent with previous results indicating water content in the range of 83-84% for Golden Delicous apples during cold storage (Fischer and Amadò, 1994), 87% for Fuji and Jazz, 88% for Braeburn and 91% for Golden Delicious (Ting et al., 2013).

The SSC amounted to 15% and was composed of various small molecules and ions soluble in alcohol, with greater heterogeneity within cultivars than the variations between cultivars (mean standard deviation was 1.5%). Ariane and Fuji had a higher SSC (15.5-18.5% and 12.7-19.8%, Table 3, statistics, group c), but close to the other cultivars (11.6-15.9%). The SSC values were consistent with the published values (about 15% for Fuji, 13% for Braeburn and Golden (Mehinagic et al., 2004) and 13% for the Cox cultivar (Harker et al., 2006)). No significant variation was observed between the different calibers. SSC increased at two months and then decreased to its one-month value after three-month storage. This may indicate an increased solubilization of solids at two months, possibly due to an increased degradation of macromolecules such as starch or pectin in the cell wall.

The AIM content was very homogeneous in all cultivars (from 1.3 to 2.6%), with a slightly higher value for Granny Smith and Ariane (1.9-2.5%, Table 3-3, statistics group b). In accordance with previous results, no significant variations in measurements occurred with storage: AIM was reported to remain at 1.8% during storage in Golden

Delicious apples (Fischer and Amadò, 1994). These results indicate increased SSC two months after harvesting did not come from increased cell wall degradation and that another mechanism occurs.

There was a low correlation between WC and SSC ($r = -0.54$). This negative correlation was certainly due to the fact that SSC represents most of the dry material and this was lessened by the variable AIM content.

5) Principal component analysis and overall correlations

Principal component analysis (PCA) was performed to reveal the relationships between the different physical, mechanical, physicochemical and chemical variables measured (Figure 3-4).

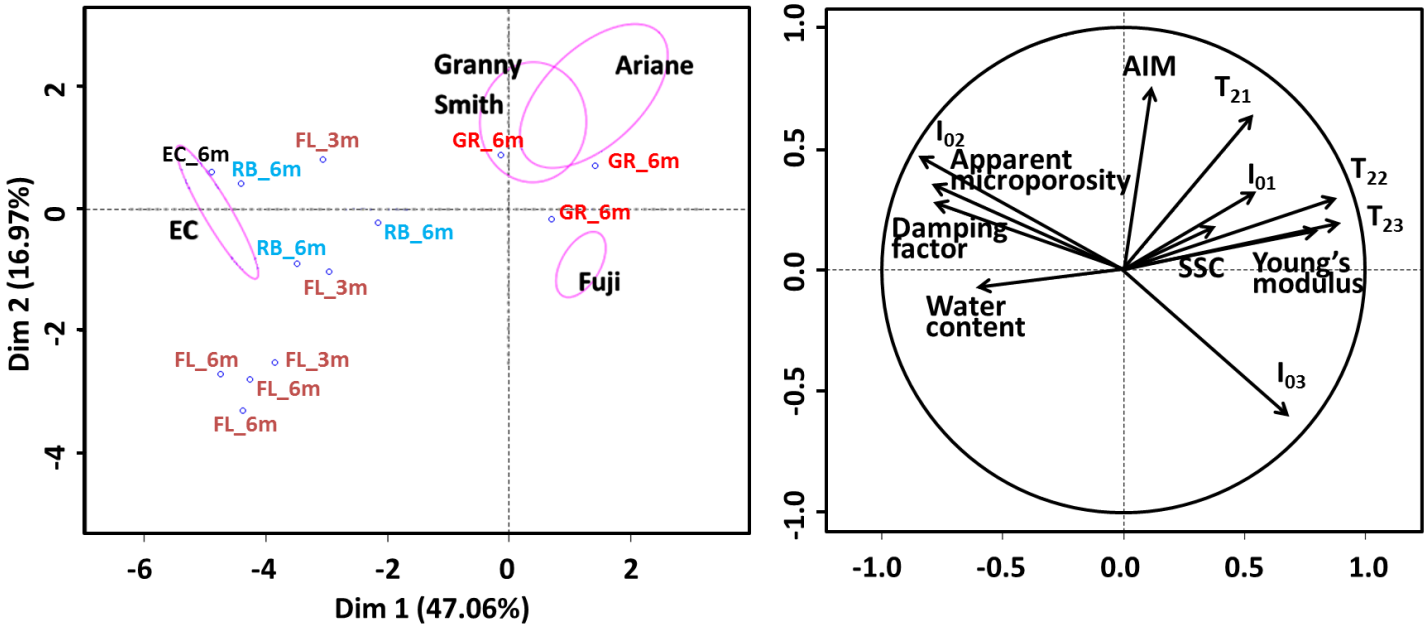

Figure 3-4: Results of principal component analysis performed on multivariate data (I_{01}, I_{02}, I_{03}, T_{21}, T_{22}, T_{23}, apparent microporosity, damping factor, Young's modulus, AIM, SSC, WC) for the four cultivars (Fuji, Ariane, EC, Granny Smith as 99% confidence ellipses) as a score plot for PC1 and PC2 with projected supplementary data (individuals, colors refer to different cultivars, web version) and a loading plot on the factorial plane consisting of PC1 and PC2. AR = Ariane, EC = experimental Cultivar, FL = Florina, FU = Fuji, GR = Granny Smith, RB = Rome Beauty.

Approximated cell volume was not correlated with the mechanical measurements and thus was removed from the dataset. Moreover, additional data from a longer storage time (EC, Granny Smith, six months) and other cultivars (Rome Beauty, Florina, three and six months) were projected on the PCA of Ariane, Granny Smith, Fuji and EC data.

T_{22}, T_{23}, I_{02}, apparent microporosity, damping factor and Young's modulus contributed distinguishing EC from the three other cultivars along the first dimension (47.1% of variance). AIM, T_{21} and I_{03} contributed most to the second dimension (17.0% of variance) and differentiated Granny Smith and Ariane from Fuji. The projection of supplementary individuals positioned EC and Granny Smith after six-month storage very close to their respective individuals after one- to three-months storage. The two new cultivars (Rome Beauty and Florina) were located close to the EC individuals (Figure 3-4). Thus, the variables contributing to the first dimension distinguished cultivars with high values for damping factor, apparent microporosity and I_{02} (EC, Florina, Rome Beauty) from cultivars with a high Young's modulus, and T_{22} and T_{23} values (Granny Smith, Fuji, Ariane).

a. Correlations between T_2 relaxation times and water content

The PCA showed that a poor correlation may exist between relaxation times and water content. T_2 is known to be related to water content and membrane permeability (Van As, 2007). A decrease in water content in gels was linked to a decrease in mono-exponential T_2 and intensity (Hills, 1992a). Few studies have focused on the relationship between relaxation times and water content in plants. Fast drying tomatoes (45 min drying, (Musse et al., 2010a)) led to a 95% to 90% loss of water content without affecting the relaxation times of any of the four T_2 components measured by NMR. Measurements in apple were performed after twenty four hours' equilibration (Hills and Remigereau, 1997). The major component of a tri-exponential fit remained stable (T_2 = 880 ms) for a 10% water content loss but decreased with greater water loss. According to Mariette et al. (Mariette et al., 1999), slow drying of apple samples from 89% WC to 80% WC led to a decrease in all relaxation times (longest component of tri-exponential fit decreased from 1200 ms to 550 ms). These results suggest that significant water loss is necessary to provoke changes in T_2 and that these changes are dependent on the drying kinetics. Slow drying kinetics would induce greater decrease in T_2, contrasting with fast drying kinetics for similar final water content. For example, studies on fresh plant materials with different water content have indicated a decrease in the longest T_2 component: in oilseed rape leaves, a decrease in water content from 94% to 90% during

leaf senescence corresponded to a decrease in relaxation time of the vacuole-associated component from 448 ms to 103 ms (Musse et al., 2013). Note that in this case, the decrease in T_2 was not due only to a water content change but was also strongly impacted by variation in vacuole size. However, this relationship is cultivar dependent (Kaku, 1993). Kaku et al. reported T_1 values (in plant tissue T_1 and T_2 are characterized by similar behavior) for leaves from different Azalea species with different water content, and showed that not all the species followed the same linear relationship. Finally, T_1 and T_2 in the outer pericarp tissue of kiwifruit showed no consistent effect for a water content decrease of about 5% over the storage period examined (Burdon and Clark, 2001). In the present results, the plot of T_{23} as a function of water content (Figure 3-5B) highlighted two different behaviors corresponding to the two groups of fruit: firm fruit had a moderate correlation with water content ($r = 0.58$, 87% to 79% water content corresponded to a reduction of T_2 from 600 to 450 ms) while Rome Beauty, Florina and EC showed no correlation (a stable value of T_{23} of 350 ms was observed). These results demonstrated that the relationship between T_{23} and water content is not straightforward in fresh apple tissues and that other mechanisms such as variation in membrane, cell wall and/or cutin permeabilities cancel out the expected variations in T_2.

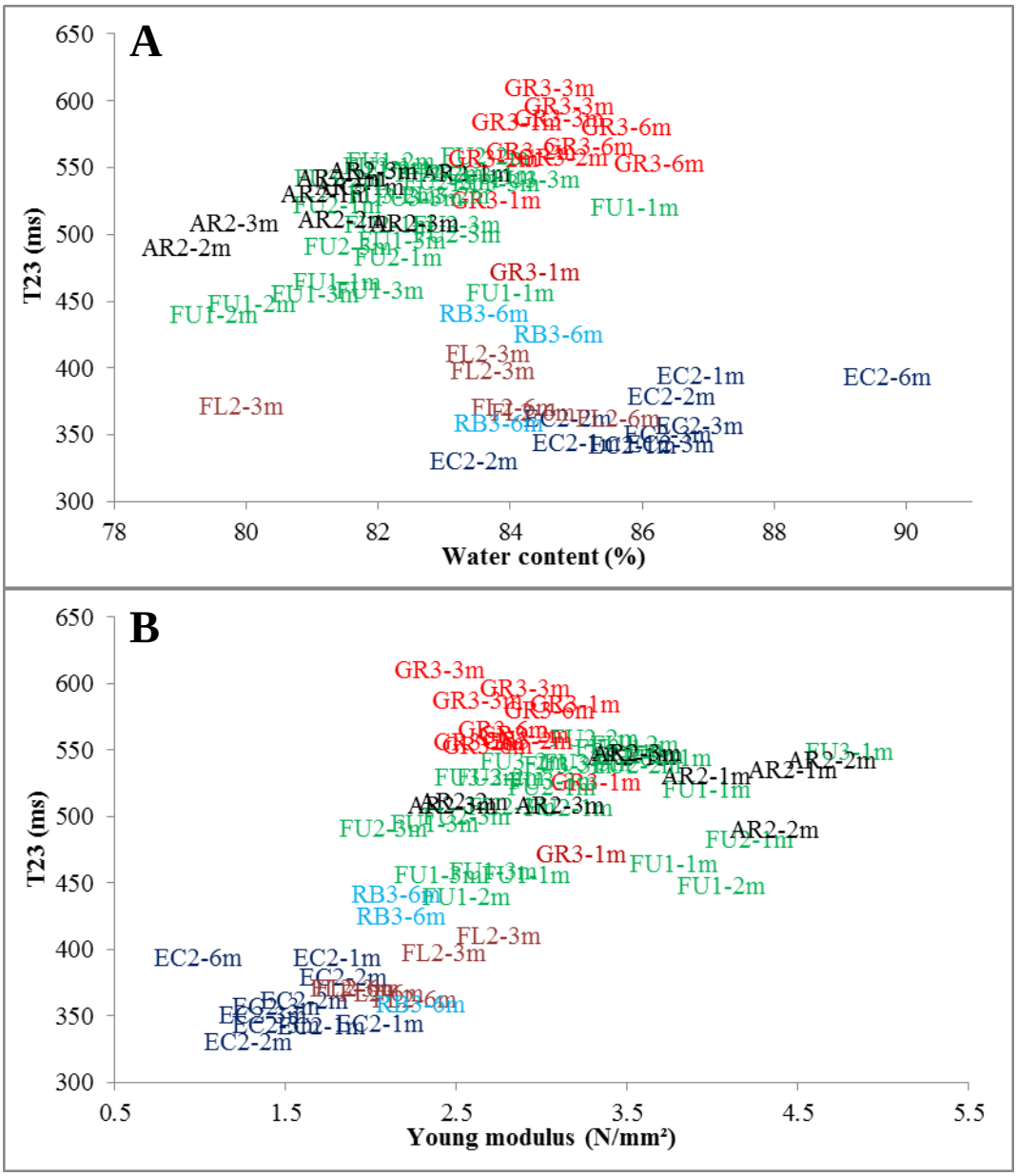

Figure 3-5: Plots of the relationships between A) T_{23} and Water content, B) T_{23} and Young's modulus. Different cultivars are shown in different colors (web version). AR= Ariane, EC = experimental Cultivar, FL = Florina, FU = Fuji, GR = Granny Smith, RB = Rome Beauty. The storage time is indicated for each sample as 1m = 1 month, 2m = 2 months, 3m = 3 months, 6m = 6 months.

b. Correlations between T_2 relaxation times, their associated relative signal intensities and mechanical parameters

Mechanical parameters were correlated with MRI data. For example, a correlation coefficient of $r_{T23/E} = 0.66$ was observed between the storage modulus and T_{23} (Figure 3-5A). The correlation was due to a cultivar effect, as different storage times did not

distinguish between the individuals among the cultivars on the PCA plot. The correlation value increased slightly ($r_{T23/E} = 0.68$) with the supplementary data from six-month storage and Florina cultivar. A positive correlation was reported (Tu et al., 2007) for Roma tomatoes between firmness of the whole fruit (peak force, 10% compression) and the mono-exponential T_2 relaxation time, but the results were not consistent on other sets of varieties and harvest years. Relationships were explored between NMR/MRI relaxation times and mealiness in Top Red and Cox's Orange Pippin apple cultivars (Barreiro et al., 2002; Barreiro et al., 2000; Barreiro et al., 1999). These authors assessed mealiness as a function of firmness, soluble solid content, shear crispness, compression hardness and juiciness. They found that T_{23} was linked to hardness, defined as force to deformation ratio and a significant decrease in T_{23} was associated with an increase in mealiness. The considerable variations in MRI parameters between the cultivars observed in the present study might thus also originate from a mealy behavior, especially as the experimental cultivar (EC), Florina and Rome Beauty were soft (Young's modulus of 2.1 ± 0.2 × 10^6 N m^{-2} and 2.2 ± 0.1 × 10^6 N m^{-2}, respectively), and Rome Beauty is known to develop mealiness on storage (Watada et al., 1980). In contrast, Fuji, Granny Smith and Ariane were firm fruit (at 3m Young's modulus of 2.7 ± 0.4 × 10^6 N m^{-2}, 2.7 ± 0.2 × 10^6 N m^{-2} and 3.05 ± 0.5 × 10^6 N m^{-2}, respectively).

Water distribution within cells was also linked to mechanical properties as I_{02} was correlated with Young's modulus and damping factor ($r_{I02/E} = -0.51$, $r_{I02/tan\partial} = 0.70$). The correlation originated from cultivar variations and also existed with supplementary data ($r_{I02/E} = -0.52$ and $r_{I02/tan\partial} = -0.54$). A trend existed between I_{01} and mechanical properties (Figure 3-6, damping factor $r_{I01/\tan(\partial)} = -0.42$), which increased when supplementary data were added ($r_{I01/\tan(\partial)} = -0.65$) due to cultivar and storage effects.

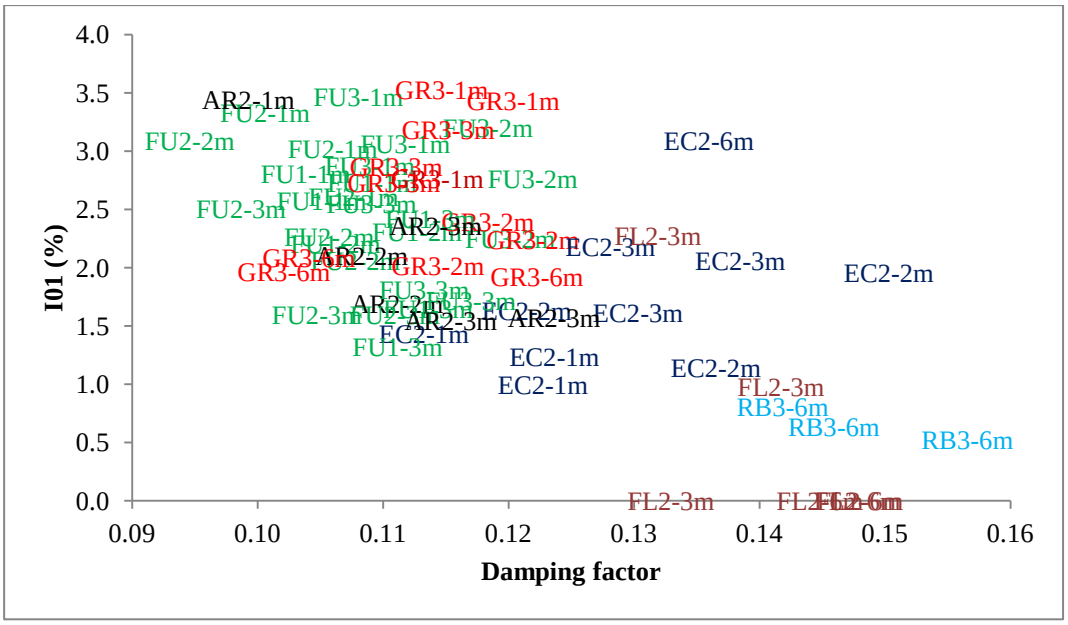

Figure 3-6: Plot of the relationship between I_{01} and Young's modulus. Different cultivars are shown in different colors (web version). AR= Ariane, EC = experimental Cultivar, FL = Florina, FU = Fuji, GR = Granny Smith, RB = Rome Beauty. The storage time is indicated for each sample as 1m = 1 month, 2m = 2 months, 3m = 3 months, 6m = 6 months.

These correlations indicate that water distribution is important for mechanical properties of the tissue and, as for relaxation times, could be linked to fruit mealiness. Long stored fruit tended to have a lower I_{01} and lower modulus, except for EC. For Florina, I_{01} was too low to be calculated accurately after six-month storage, leading to a bi-exponential signal. This change may reflect the merging of I_{01} and I_{02}, the relaxation time of the protons of the former pool increasing to reach that of T_{22}. This hypothesis could be linked to cell wall swelling observed in fruit that ripen to a soft melting texture (Redgwell et al., 1997). Although not observed by the latter authors in ripe Cox and Braeburn apples, the cell wall swelling may be at the origin of the decrease in or disappearance of I_{01} observed in long stored fruit. The short T_{21} is mainly attributed to a fast relaxing water pool interacting with cell wall macromolecules. Changes in cell wall polysaccharide chemistry and particularly pectin in the apple (see below, (Brummell, 2006; Massiot et al., 1996)) may contribute to increased cell wall swelling (MacDougall et al., 2001; Tibbits et al., 1998) and could be linked to the behavior of the first component measured. Studying cell wall composition could thus provide a better understanding of the modifications measured during cold storage.

c. *Correlations between apparent microporosity and mechanical and chemical measurements.*

The mechanical parameters were also correlated with the apparent microporosity (Figure 3-7A, Young's modulus $r_{poro/E} = -0.55$; and not shown damping factor $r_{poro/\tan(\partial)} = 0.65$) and the correlations remained close when supplementary fruit data were added ($r_{poro/E} = -0.56, r_{poro/\tan(\partial)} = 0.57$). These were due to a cultivar effect. Ting et al. (Ting et al., 2013) correlated firmness with low tissue microporosity in four apple cultivars. Our results also showed a trend between apparent microporosity and water content (Figure 3-7B, $r_{poro/WC} = 0.55$). This trend was reduced with the supplementary results ($r_{poro/WC} = 0.42$) due to fruit having extreme water content values (Florina-2m and EC-6m, 80% and 90% WC, respectively) while other fruit matched the previously established relationship, showing the heterogeneity of the sample. Fruit with higher apparent microporosity had higher water content and a correlation was observed between apparent microporosity and I_{02} ($r_{poro/I02} = 0.75$, with supplementary fruit $r_{poro/I02} = 0.74$) indicating that water content and distribution may influence tissue microstructure. It should be noted that the correlations involving apparent microporosity could be emphasized because of the probable overestimation of the highest apparent microporosity values mentioned above.

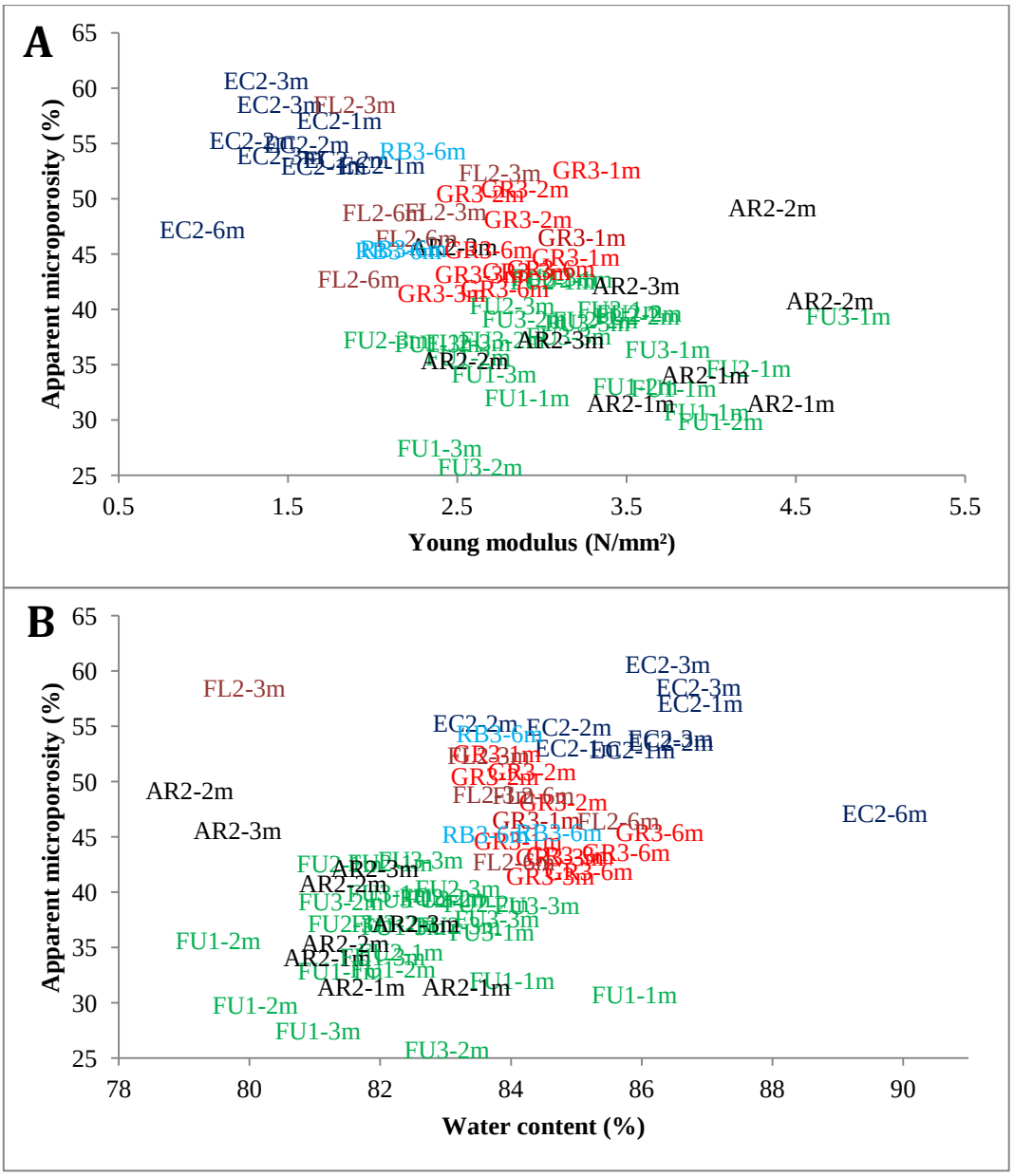

Figure 3-7: Plots of the relationships between A) apparent microporosity and Young's modulus, B) apparent microporosity and water content. Different cultivars are shown in different colors (web version). AR= Ariane, EC = experimental Cultivar, FL = Florina, FU = Fuji, GR = Granny Smith, RB = Rome Beauty. The storage time is indicated for each sample as 1m = 1 month, 2m = 2 months, 3m = 3 months, 6m = 6 months.

d. Correlations between chemical measurements and mechanical parameters

No correlation was observed between soluble solid or AIM content and mechanical or MRI variables (Supplementary Table 3-6).

In particular, a correlation between SSC and Young's modulus was anticipated as firmness was correlated with dry matter content (Palmer et al., 2010) and SSC represents the major part of dry matter. The lack of correlation observed may be the result of the small variation range compared to standard deviations in the fruit studied. This emphasizes the complexity of genetics-dependent factors contributing to the water status in fruit and to its mechanical properties.

6) Cell wall polysaccharide chemistry

As cell walls are important determinants of the mechanical properties of fruit, their composition was characterized in selected AIM prepared from fruit that cover a wide range of mechanical properties, irrespective of cultivar, caliber or storage (Supplementary Figure 3-8).

The range of neutral sugar, uronic acid and acetic acid ester content and of degree of methylesterification is presented in Supplementary Table 2-7.

Table 3-4: Table showing the mean, minimum and maximum values of cell wall measurements for neutral sugars as percentage of fresh weight. Degree of Methylation (DM) is expressed as percentage of Uronic Acid and Acetic Acid content as percentage of fresh weight.

	Uronic Acid (%)	Rhamnose (%)	Fucose (%)	Arabinose (%)	Xylose (%)	Mannose (%)	Galactose (%)	Glucose (%)	DM (%)	Acetic (%)
Mean	0.44	0.03	0.03	0.23	0.17	0.05	0.14	0.72	66	2.03
min	0.28	0.01	0.00	0.08	0.11	0.03	0.06	0.47	50	1.39
max	0.71	0.06	0.06	0.48	0.26	0.08	0.27	1.29	79	2.62

The chemical compositions were in agreement with previous studies, uronic acid, glucose, galactose and arabinose being the major components (Fischer and Amadò, 1994; Galvez-Lopez et al., 2011; Pena and Carpita, 2004). The degree of methylesterification (DM) (Table 3-4) was in the range reported by previous studies: the DM of the Golden Delicious cultivar were 72% and 75% (Billy et al., 2008; Renard et al., 1990), between 69 and 78% for the Judeline cultivar (Massiot et al., 1996), 85% for Jonagold (Gwanpua et al., 2014) and between 69% and 75% for Fuji (Billy et al., 2008). The AIM weight percentage of acetic acid corresponded, when considered in relation to the uronic acid content, to a degree of acetylation between 16.4% and 32.8%, which is in agreement with the degree of acetylation of between 26% and 36% of Golden Delicious

(Fischer and Amadò, 1994; Renard et al., 1990) but higher than the percentages found for Fuji and Golden Delicious in another study (Billy et al., 2008). It should be noted that considering degree of acetylation in relation to galacturonic acid also induces a bias, as apple hemicelluloses are also acetylesterified (Fischer and Amadò, 1994; Ray et al., 2014).

Table 3-5: Table showing the correlations between chemical measurements of cell wall components and mechanical and chemical measurements. Gray color indicates the main correlations.

	AIM	SSC	Young Modulus	Damping factor
UA	0.70	-0.05	0.08	0.28
Rhamnose	0.33	0.03	-0.14	0.52
Fucose	0.40	-0.05	-0.15	0.59
Arabinose	0.69	0.16	0.58	-0.30
Xylose	0.45	0.19	-0.19	0.60
Mannose	0.40	-0.06	-0.14	0.07
Galactose	0.84	0.20	0.27	0.00
Glucose	0.91	-0.01	0.27	0.15
XXG	-0.23	0.19	0.24	-0.41
XLXG	0.14	0.22	-0.12	0.45
XLXGa1	-0.26	0.29	0.17	-0.43
XXXFGa1	-0.42	-0.48	-0.46	0.28
XLFGa1	0.37	-0.20	-0.17	0.54
DU4m3	-0.14	0.24	0.05	0.31
DU5m4	-0.25	0.29	-0.01	0.22
DU6m5	-0.25	0.02	-0.16	-0.07
DM	0.15	0.11	0.17	-0.42
Acetic	-0.07	-0.33	-0.40	0.38

Correlations between cell wall polysaccharide composition (excluding the minor sugars rhamnose, fucose and mannose) and instrumental measurements are presented in Table 3-5. Water content, apparent microporosity and MRI results showed no correlation with any of the cell components measured. Note that the correlation between Young's modulus and the damping factor still existed for the samples studied ($r = 0.58$). Major components of the cell wall (arabinose, galactose, glucose and uronic acids) positively correlated with AIM content (r > 0.70). Arabinose content correlated with the Young's modulus ($r_{ara/E} = 0.58$). Xylose content correlated with the damping factor ($r_{xyl/\tan(\delta)} = 0.60$). Arabinose content has been shown to decrease during storage

in Golden Delicious (Fischer and Amadò, 1994) and to decrease with firmness during storage in Red Delicious, Gala, Firm Gold and Gold Rush (Pena and Carpita, 2004). On the other hand, xylose content is generally reported to increase with storage in most cultivars (Fischer and Amadò, 1994; Pena and Carpita, 2004). This is the first positive correlation between xylose content and the viscous character of apple parenchyma tissue to date. As xylose is a major component of xyloglucan, this relationship may result from the enrichment of cell walls in xyloglucan due to the metabolism of pectin during storage. This enrichment may exacerbate the hemicellulose contribution to the compliance of the cell wall (Chanliaud et al., 2002). No correlations were found between the degree of pectin methylesterification or acetic acid ester content and any mechanical parameters. These results suggest that acetylation and esterification of cell walls does not vary linearly during storage. Previous studies showed that the degree of acetyl esterification in Golden Delicious varied during storage, going from 27% at harvest to over 30% between 9 and 15 weeks and back to 26% after 25 weeks' storage (Fischer and Amadò, 1994). Our results show no significant variations in degree of acetylation over time and a considerable dispersion at each measurement time, which was certainly due to the differences between the fruit selected and the low number of samples. The DM of pectin in AIM showed considerable variations due to the different apple material studied, but on average did not change significantly with storage. Previous studies showed that overall DM does not change during ripening (Billy et al., 2008; De Vries et al., 1981; Gwanpua et al., 2014) but increases in solubilized pectin during storage (Gwanpua et al., 2014; Knee, 1978a, b). No correlations were found between methyl- or acetylesterification and MRI parameters or mechanical measurements, suggesting that mean pectin methylesterification and acetylation are not major determinants of the subcellular state of water or the mechanical properties of fruit.

To assess further the effects of the fine structure of cell wall polysaccharides on the mechanical properties of apple parenchyma, the distribution profile of methylesters and the branching pattern on readily accessible pectic homogalacturonan and xyloglucan were assessed by subjecting AIM to pectin lyase and glucanase degradation, respectively. The MALDI-TOF MS profile of the pectin-lyase hydrolyzate was close to that published for other fleshy fruits (Lahaye et al., 2014; Lahaye et al., 2012a) and composed mainly of unsaturated oligo-galacturonides of degree of polymerization (DP) 4 substituted by 4 and 3 methyl esters (DU4m4, DU4m3), of DP5 with 4 methyl esters

(DU5m4) and of DP6 with 5 methyl esters (DU6m5; Supplementary Figure 3-9). The MS profile of hemicelluloses was in agreement with the known major apple xyloglucan structures XXG, XXXG, XLXG, XLXGal, and XLFGa1 (Supplementary Figure 3-10); (Galvez-Lopez et al., 2011)). When considering the variability of intensity of normalized pectic and xyloglucan ion intensities in the AIM hydrolyzates in relation to the mechanical and MRI parameters, only the XLFGa1 ion intensity correlated with the damping factor ($r = 0.54$). This correlation supports the involvement of xyloglucan in regulating cell wall compliance (Chanliaud et al., 2002), though the relation between its fine structure, its interactions in the cell wall and the resulting mechanical properties remains to be established. To date, alterations in xyloglucan structures were reported in particular cases to only affect plant development (Schultink et al., 2014).

For the soft Florina cultivar, a 20% increase in DU4m3 and DU5m4 content by 20% was observed whereas the DM was reduced by 10% between three months and six months after harvesting as the first MRI component disappeared. This finding, that remains to be repeated on more fruit, suggests that, as in high DM pectin gels, methyl ester distribution (i.e. the degree of blockiness) rather than mean DM may be more pertinent with regard to cell wall rheological properties (Slavov et al., 2009). In the light of the relation between pectin methylesterification and cell wall swelling (MacDougall et al., 2001) and the observation of swollen cell walls in soft textured ripe fruit (Redgwell et al. 1997), subsequent studies should also assess the role of pectin demethylesterification in the development of soft to mealy apples as already reported in peaches (Fruk et al., 2014).

IV. CONCLUSION

The different approaches used in the present study revealed various mechanisms impacting on the mechanical properties of apple tissue.

First, the results confirmed a link between cell wall constituents and the mechanical properties of apple parenchyma tissue. Investigating both the viscous and elastic behavior of the fruit tissue demonstrated that, although the damping factor and Young's modulus were correlated, different components of the cell wall influence viscous and

elastic behavior independently. Indeed, arabinose content was correlated with Young's modulus. Xylose and XLFGa1 were linked to the damping factor, indicating that hemicellulose influences the viscous behavior of apple parenchyma tissue. Sub-cellular water distribution and status estimated non-invasively by MRI were also correlated with the mechanical properties of the sample. The T_{23} attributed to the water in the vacuole was positively correlated with the Young's modulus, and the relative intensity I_{02} attributed to the cytoplasm water compartment was correlated with both the damping factor and the Young modulus. The relative intensity of these two components was highly correlated, demonstrating that water exchange occurs between these two compartments. Moreover, we have shown that the T_{23} variations were not explained by the water content, and thus other phenomena probably predominate in the relaxation mechanism such as membrane permeability, vacuole size and/or solute composition. Modification of the water pool attributed to the extracellular water/cell wall was shown to be involved in softening. Further studies should demonstrate whether the decrease in T_{21} with apple ripening is linked to the swelling of the cell wall involved in the development of soft to mealy texture. Measuring the water diffusion and the ion concentration in parenchyma tissue would probably also improve understanding of the relaxation components.

Both elastic and viscous mechanical characteristics were linked to the apparent microporosity of the tissue, in support of literature data relating the amount of intercellular spaces to the mechanical properties of fruit.

Understanding the mechanical behavior of apple tissue requires a global study of the different determinants that contribute on different scales to its viscoelastic properties. This goal was achieved by adopting for the first time a multi-instrumental approach in which quantitative MRI measurements proved to be invaluable in assessing the contribution of microstructure and water status. To refine and hierarchize determinants contribution to the viscoelastic properties of apple, future studies may consider maximizing the range of mechanical characteristics variations through a selection of fruit and storage conditions. Coupling this approach to sensory analysis may shade new lights on the weighted combination of determinant characteristics of flesh viscoelastic properties responsible for desired texture descriptors.

Acknowledgments: This study was financed in part by the AI-FRUIT Pays de la Loire Research Program. Guillaume Winisdorffer was supported in part by a scholarship from the Pays de la Loire and Bretagne regions. Part of this work (cell wall and MS) was realized using the equipment and resources of INRA-BIBS platform. Authors thank B. Petit and the IRHS team for providing the fruit, MJ Crepeau and L. Hélary from INRA-BIA for pectin methylesterification and macro-vision measurements, respectively, and M. Delaire (IRHS, Angers) and M-F. Devaux (INRA-BIA, Nantes) for scientific discussions.

V. SUPPLEMENTARY DATA

Supplementary Table 3-6: Table showing the Pearson correlation coefficients between water content, alcohol insoluble material and soluble solid content, and MRI and mechanical measurements.

	T_{21}	T_{22}	T_{23}	I_{01}	I_{02}	I_{03}	porosity	module	tandelta	cell_volume	elongation_factor
WC	-0.28	-0.36	-0.36	-0.15	0.44	-0.40	0.55	-0.50	0.37	-0.16	-0.03
MIA	0.41	0.23	0.20	0.04	0.18	-0.20	0.25	0.22	0.06	0.02	0.14
SSC	0.25	0.29	0.29	-0.02	-0.23	0.25	-0.20	0.22	-0.12	0.33	-0.12

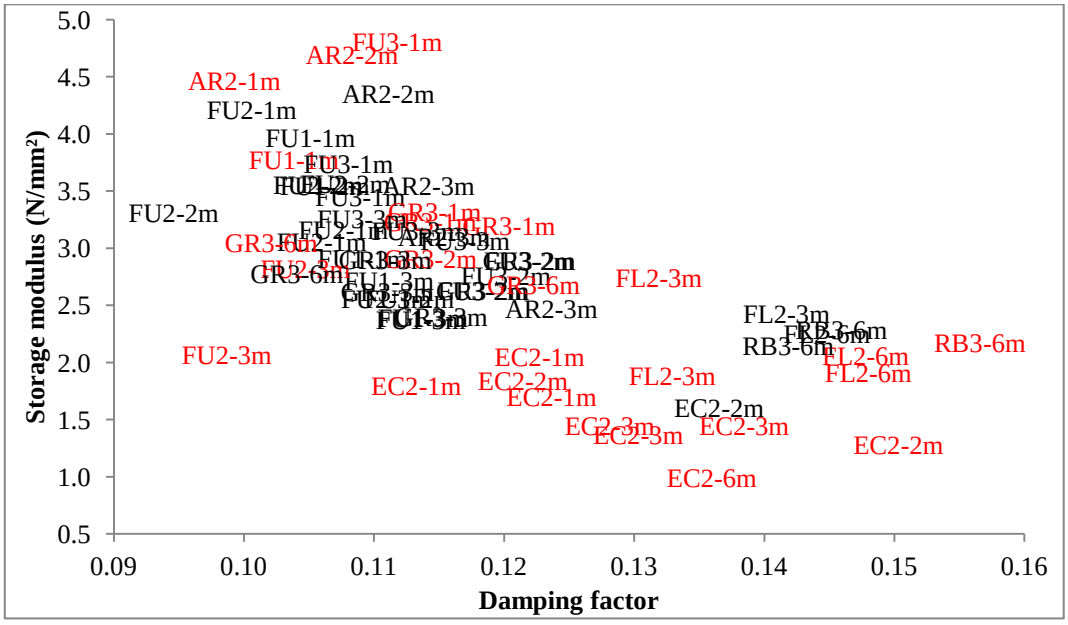

Supplementary Figure 3-8: Plot of the relationship between Young's modulus and damping factor showing the fruit selected for chemical analyses of cell walls in red color. AR= Ariane, EC = experimental Cultivar, FL = Florina, FU = Fuji, GR = Granny Smith, RB = Rome Beauty. The storage time is indicated for each sample as 1m = 1 month, 2m = 2 months, 3m = 3 months, 6m = 6 months. The reader is referred to the web version of this article for interpretation of the references to color in this figure legend.

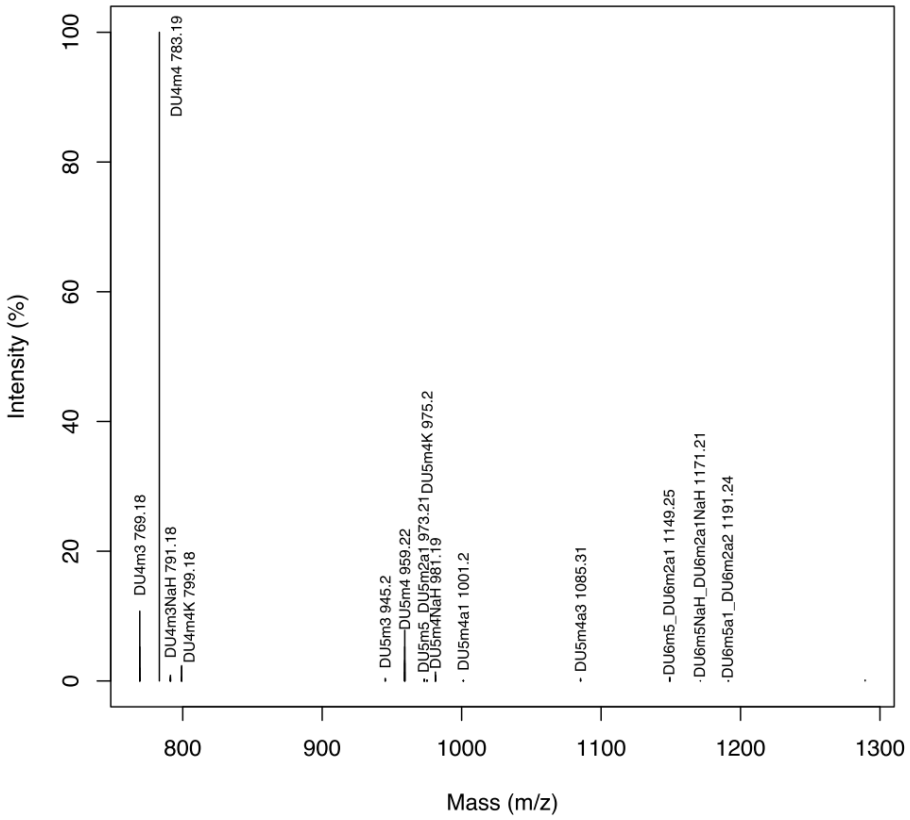

Supplementary Figure 3-9: Mean MALDI-TOF MS spectrum of the pectin-lyase hydrolyzate of cell wall preparations. See text for nomenclature.

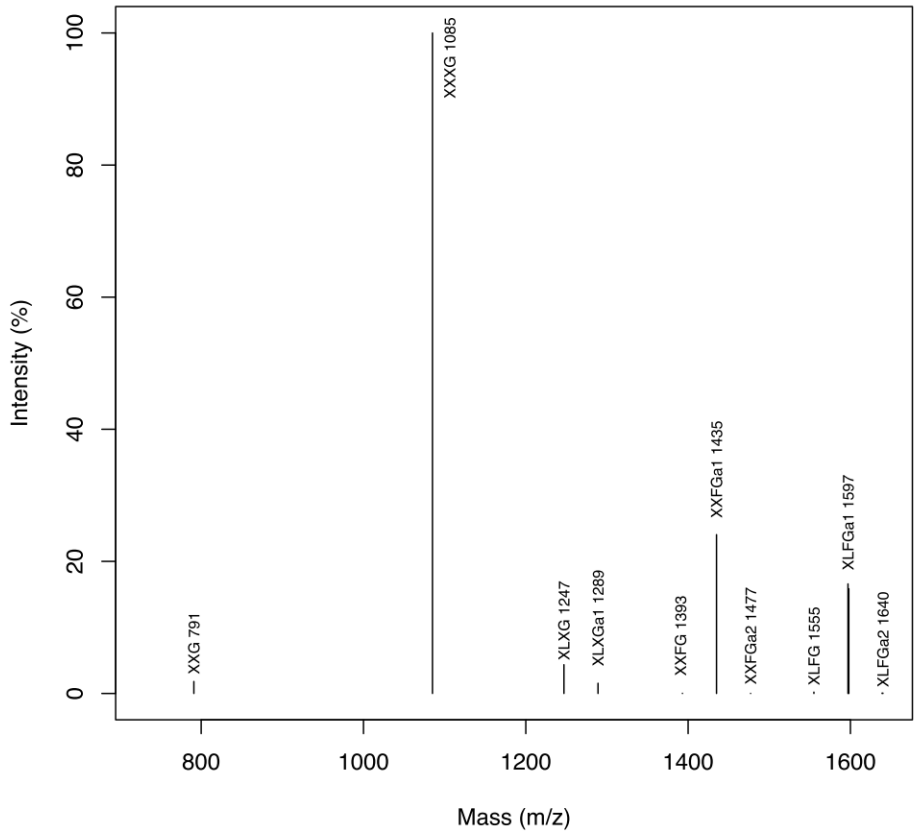

Supplementary Figure 3-10: Mean MALDI-TOF MS profile of hemicelluloses. See text for nomenclature.

Chapter 4: Effect of storage on the NMR signal of the different tissues of apple fruit

4. Effect of storage on the NMR signal of the different tissues of apple fruit

The heterogeneous structure of apple fruit has been reviewed in the first chapter (Figure 1-1) and has been well described with regard to the parenchyma tissue (Khan and Vincent, 1990; Schotsmans et al., 2004; chapter 2). The previous chapters described the variation of the transverse relaxation times in specific regions of interest without taking into account the variations in the whole fruit and the possible interactions between tissues. This chapter focuses on the microstructure and water status of different tissues using quantitative MRI to highlight differential modifications of these tissues during storage.

I. MATERIAL AND METHODS

1) Fruit

Six apples of Granny Smith and EC cultivars were harvested at maturity (starch test, 7-8 (Vaysse P., 2004)). The fruit were stored at 4 °C before measurements. Two measurements were performed: the first at one month and the second six months after harvest. For each measurement, three fruit of each cultivar were scanned by MRI.

2) MRI

a. Acquisition

MRI measurements were carried out with a 1.5T MRI scanner (Magnetom, Avanto, Siemens, Erlangen, Germany). The fruit were equilibrated at 20 ± 0.5 °C for 10 hours in the Faraday cage of the MRI scanner prior to acquisitions; acquisitions were performed at the same temperature. The same protocols as in chapters 1 and 2 were used. The median plane of each fruit (transverse section at middle height of fruit) was imaged with a pixel size of 1.19 mm x 1.19 mm, slice thickness of 5 mm and repetition time of 10 s. Two MRI sequences were performed: (i) a multi spin echo (MSE) sequence, with non-selective refocusing pulse, inter-echo spacing (ΔTE) of 7.1 ms, bandwidth 260 Hz/pixel,

1 scan and 512 echoes per echo train for multi exponential T_2 estimation and (ii) a multi gradient echo (MGE) sequence, with first echo time (TE1) of 2.8 ms and ΔTE of 1.6 ms, bandwidth 1096 Hz/pixel, 12 echoes and 2 scans for T_2* estimation. A discussion on the MRI measurements is presented in the appendix of this work. The SNR of the images obtained by the MSE and MGE sequences on outer cortex tissue at the shortest echo time were approximately 120 and 80, respectively.

b. Image processing

The T_2 and T_2* of apple parenchyma were computed by both pixel-by-pixel- and Region of Interest (ROI)- based approaches. First, a pixel-by-pixel approach was used to calculate T_2 and T_2* maps using Scilab software (Scilab, 2012). Prior to fitting, cuticle tissue, seeds and core tissue close around them together with the image background were masked using Otsu's thresholding method (Otsu, 1979). Mono-exponential T_2 maps were generated by performing pixel-to-pixel fitting via the Levenberg-Marquardt algorithm for chi-square minimization according to Equation 1-2 ($I(t) = \sum_{i=1}^{n} I_{0i} \times e^{\frac{-t}{T_{2i}}} + const$, for i=1). Second, a ROI-based approach was used as it improved the Signal to Noise Ratio (SNR) (Adriaensen et al., 2013). The mean signal over the ROI was computed with TableCurve 2D software (Systat, 2007) for all the MSE images of the series and then fitted according to a tri-exponential decay curve (Equation 1-2, i=3).

The mono-exponential T_2 of selected ROIs was computed from Equation 1-2 for i=1, and that of T_2* by replacing T_2 by T_2*. Apparent microporosity was then computed in the ROIs from T_2 and T_2* according to Musse et al. (Musse et al., 2010b).

Proton density (I_0) maps were extracted from the mono-exponential T_2 fit.

ROIs were selected manually on homogeneous regions of mono-exponential T_2 and T_2* weighted images using ImageJ software (Schneider et al., 2012). These images were chosen to draw the ROIs due to their ponderation in proton density and T_2/T_2*.

For Granny, five homogeneous regions in terms of T_2 and T_2* were selected corresponding to outer core (Figure 4-1A), inner core (Figure 4-1B), vascular bundles

and surrounding tissue (Figure 4-1C) and the two regions previously studied (inner and outer parenchyma; see chapter 2 and Figure 4-1D).

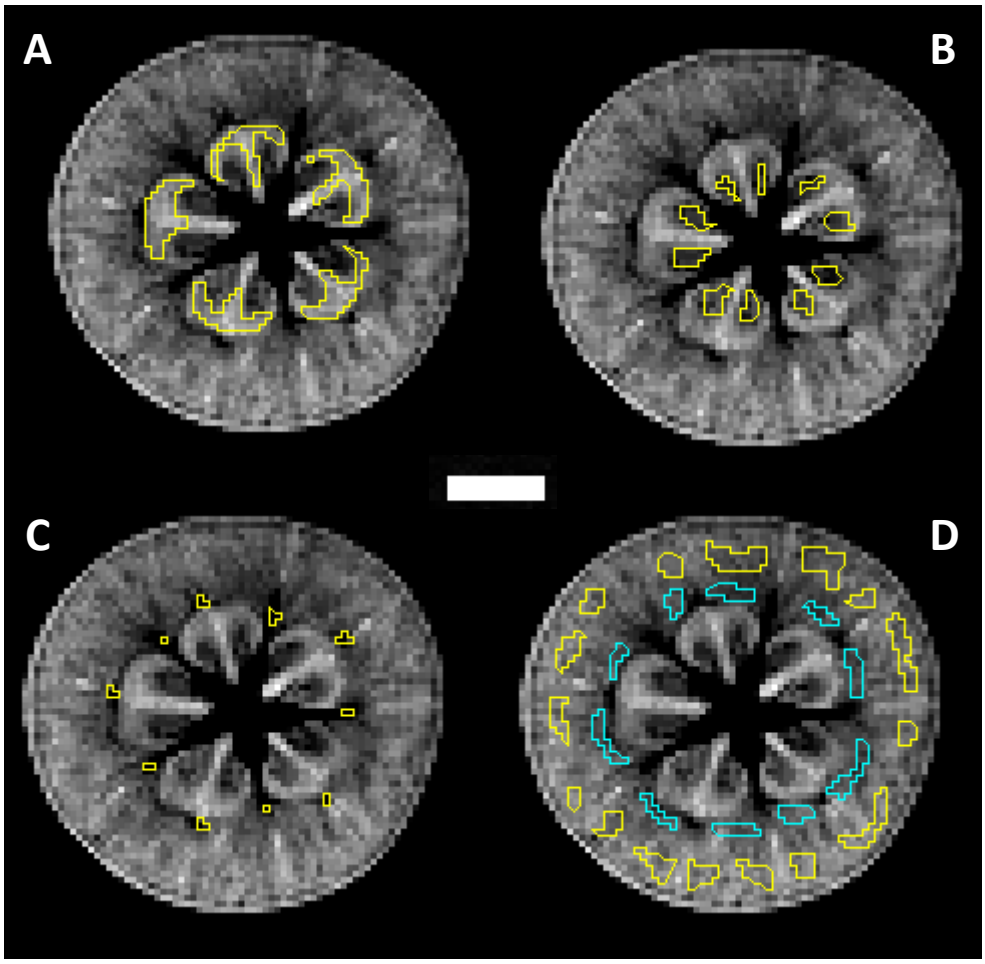

Figure 4-1: Regions of interest shown on T_2-weighted images (MSE sequence, TE=340 ms) of Granny Smith cultivar after one-month storage: (A) outer core region (~350 voxels), (B) inner core region (~150 voxels), (C) vascular bundles (~35 voxels) and (D) outer parenchyma (yellow, ~350 voxels) and inner parenchyma (blue, ~175 voxels). The scale bar is 2 cm.

For EC, the ROIs are shown on six-month storage T_2-weighted images (Figure 4-2) and were, as for Granny Smith apples, selected to consider homogeneous tissue in terms of both T_2 and T_2*. A single core region was selected (Figure 4-2A) due to the specific tissue structure of this cultivar. An under-cuticle region was considered (Figure 4-2B) and the two previously studied regions of the parenchyma (see chapter 1). The region under the cuticle was studied for six-month stored fruit only, as it could not be distinguished from outer parenchyma after one-month storage. At one-month storage time, outer parenchyma and under-cuticle regions were considered to be the same.

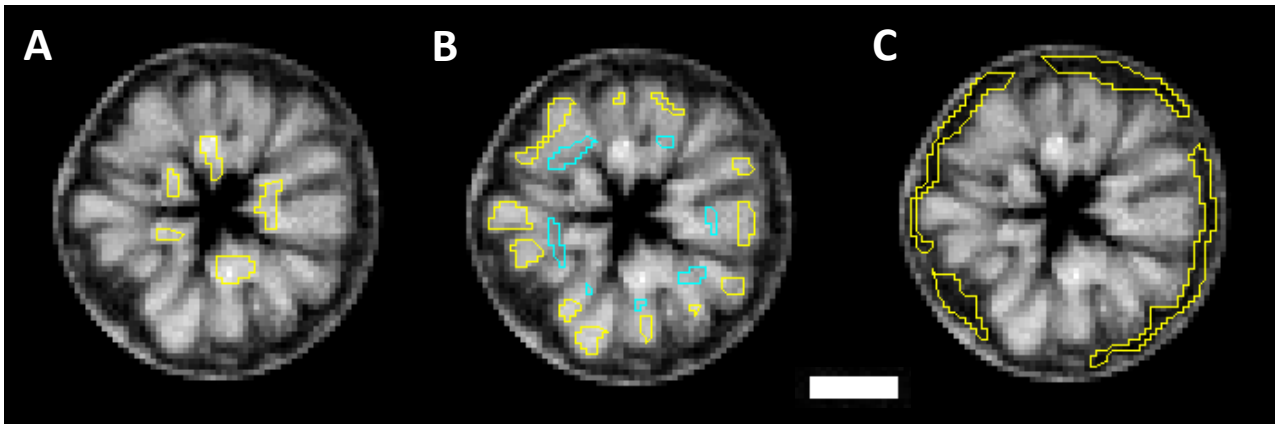

Figure 4-2: Regions of interest shown on T_2 weighted images (MSE sequence, TE=340 ms) of EC cultivar after six months storage: (A) core region (~60 voxels), (B) outer parenchyma (yellow, ~400 voxels) and inner parenchyma (blue, ~200 voxels), (C) under-cuticle region (~350 voxels). The scale bar is 2 cm.

More details about MRI measurements and numerical simulations of T_2 and T_2* signals used for estimation of the errors in computing multi-exponential T_2 relaxation parameters and apparent microporosity are given in Appendix.

II. RESULTS

1) Spatial distribution of monoexponential T_2, proton density and apparent microporosity

Monoexponential T_2 maps of the two cultivars at the two storage times are shown in Figure 4-3. For Granny Smith, two regions were distinguished in the parenchyma defined as outer and inner parenchyma, as shown in Chapter 2. At one-month storage (Figure 4-3A), the outer parenchyma T_2 was about 600-650 ms and inner parenchyma T_2 was about 450 ms. In the core, the outer region had a T_2 of about 500 ms and the inner region a T_2 of about 400 ms. The vascular bundles and surrounding tissue had relatively low T_2 of 250 ms. At one-month storage time, the parenchyma of EC (Figure 4-3B) was more homogeneous than Granny Smith cultivar and the inner and outer regions could not be distinguished. Parenchyma T_2 ranged between 350 and 450 ms. In the core, T_2 was about 250 to 300 ms. Vascular bundles could not be distinguished for EC.

After six-month storage (Figure 4-3C), the T_2 of the inner parenchyma for Granny Smith did not vary while it decreased in the outer parenchyma and in the outer and inner core regions (from 600-650 ms to 500-550 ms in outer parenchyma, from 500 ms to 450 ms in outer core and from 400 ms to 320 ms in inner core). In the outer core, T_2 became closer to that of the inner parenchyma so that the border between the two regions could hardly be distinguished. For EC at six-month storage time (Figure 4-3C and D), a low-T_2 region (250-300 ms) appeared under the cuticle and the core was separated from the parenchyma by a very low T_2 region (less than 200 ms). Between 1- and six-month storage times, the parenchyma T_2 decreased slightly (from 350-450 ms to 300-400 ms) and become very heterogeneous with low T_2 regions while that in the core increased to the same values (300-400 ms). The low T_2 regions seemed to be associated with vascular bundles according to their expected locations.

When compared to each other, the Granny Smith and EC cultivars had very different T_2 values.

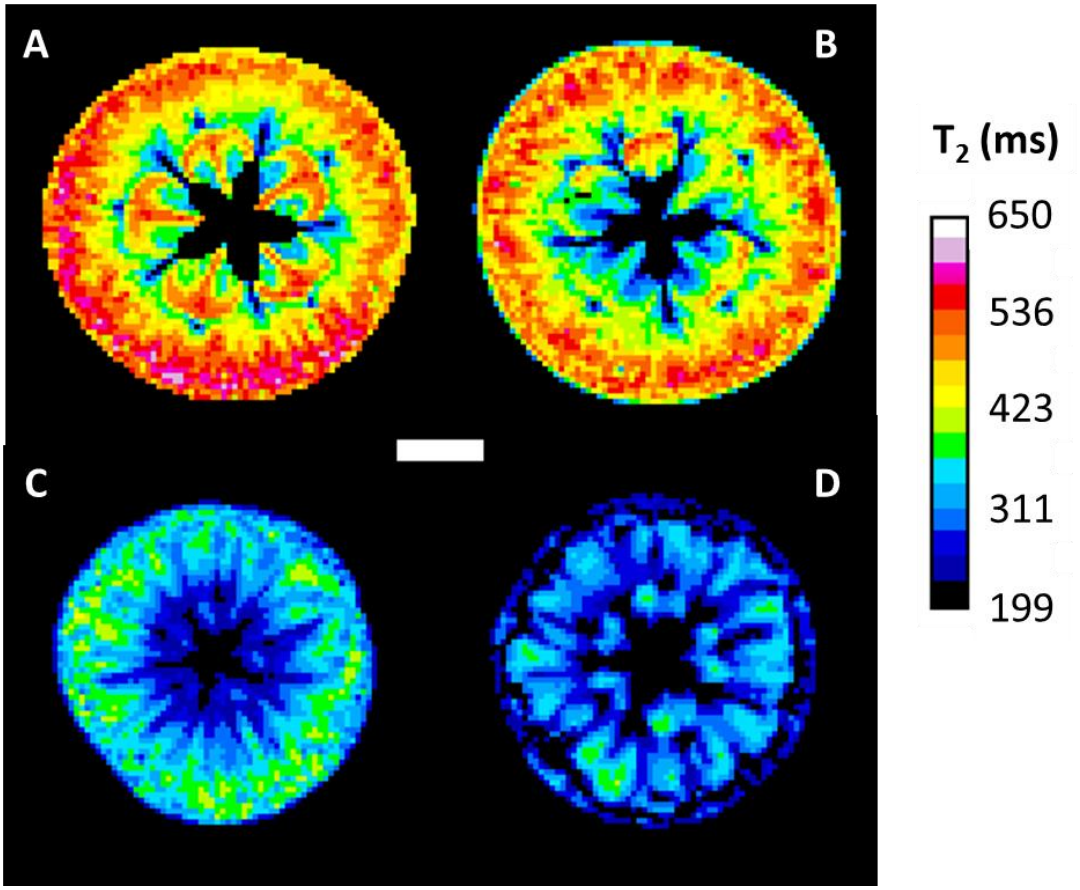

Figure 4-3: Examples of T_2 maps of Granny Smith cultivar one month (A) and six months (B) after harvest and EC one month (C) and six months (D) after harvest. Scale bar is 2 cm.

A spatial variation of proton density (I_0) maps, principally due to the radiofrequency field reception imperfections, was estimated by measuring I_0 (extracted from the mono-exponential T_2 fit) on a water-filled phantom with the same MSE sequence (Figure 4-4A). Profiles plotted along the horizontal axis of the phantom and of apples of both cultivars at both measurement times were drawn (Figure 4-4B). In the region considered, the spatial I_0 variations observed on the phantom image were low compared to variations in apple images and were therefore considered to be insignificant for the following analyses.

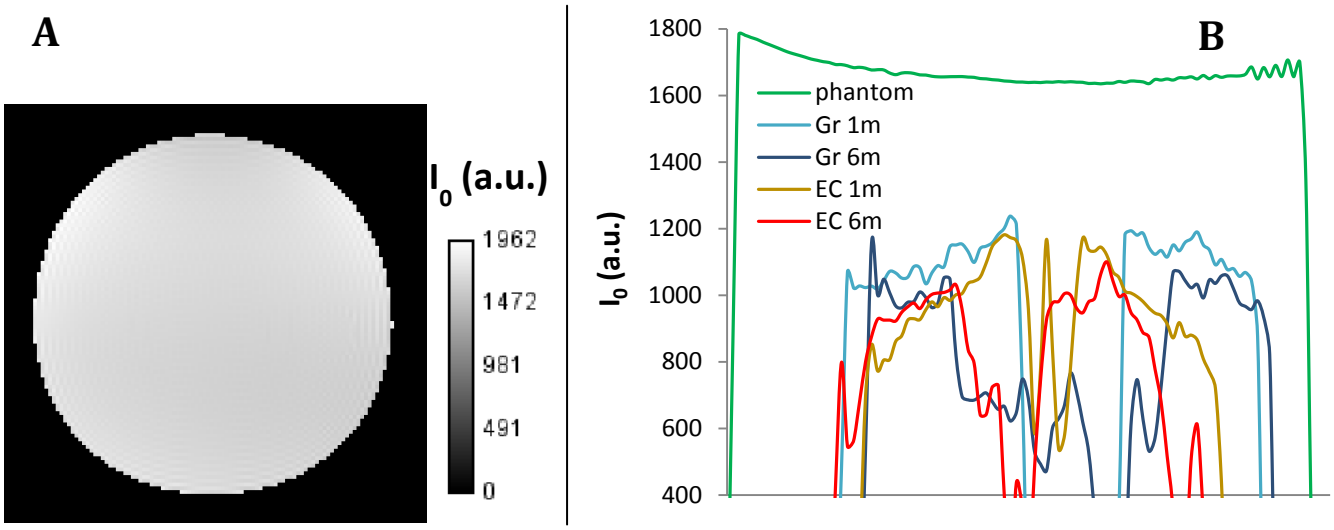

Figure 4-4: M_0-map of a phantom (A) and plots of the profiles from phantom and fruit from each group (B).

Figure 4-5 shows an example of proton density maps.

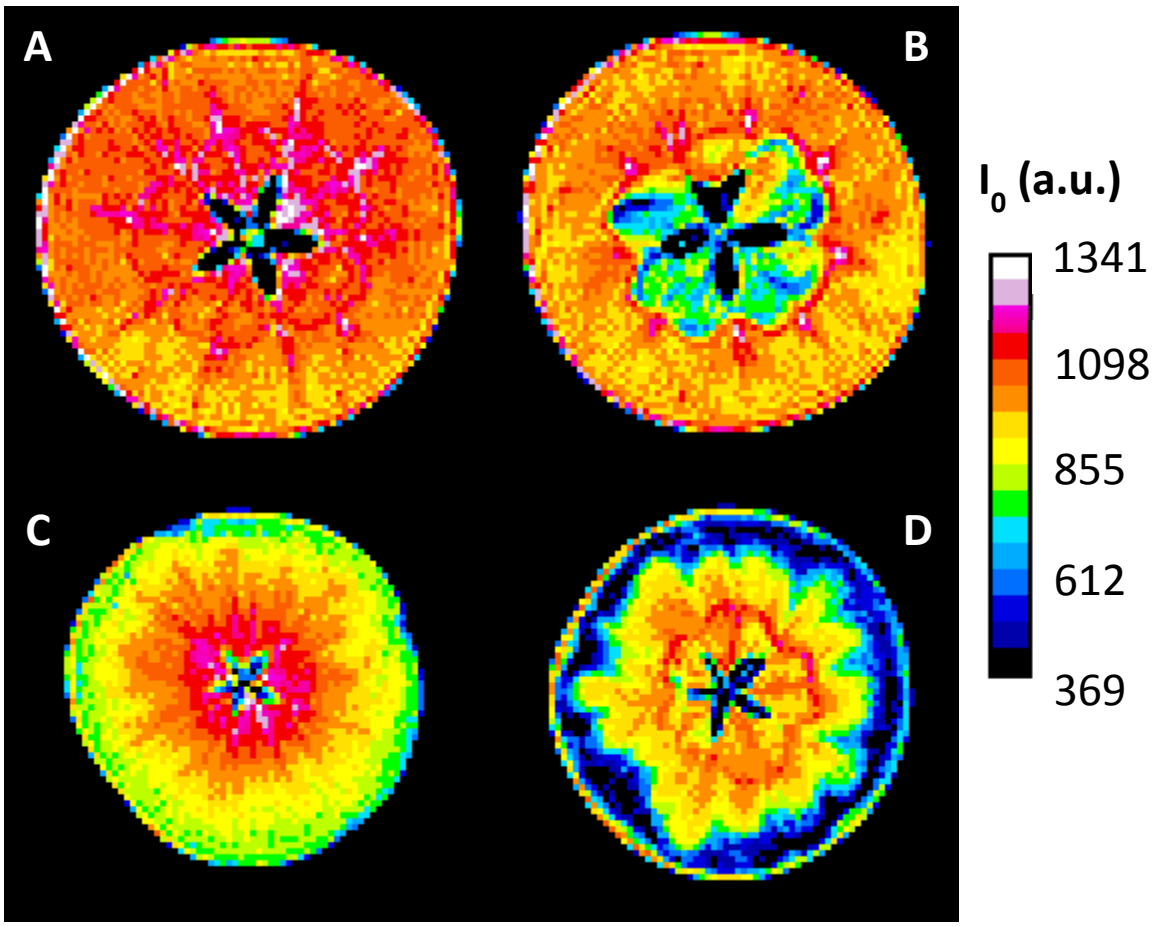

Figure 4-5: Examples of I_0 maps of Granny Smith cultivar one month (A) and six months (B) after harvest and EC one month (C) and six months (D) after harvest. I_0 maps were computed from mono-exponential fit of the T_2 decays. Scale bar is 2 cm.

For Granny Smith, the proton density was the same in core and parenchyma at one-month storage (about 1100 a.u.). The vascular bundles had a slightly higher proton density than other tissues. To the contrary, EC had an important gradient from the cuticle (about 800 a.u.) to the center of the fruit where the proton density was higher (about 1150 a.u.) (Figure 4-5C). After six-month storage, the core tissue of Granny Smith had the lowest intensity of the fruit (650 a.u.). The intensity in the parenchyma did not change much (about 1100 a.u.) and the vascular bundles still had the highest intensity (over 1300 a.u.). For EC, the gradient no longer existed, core tissue lost intensity to reach a value close to the one of the parenchyma, which did not change much for that cultivar either (about 900 a.u.). A border separating core from parenchyma could be distinguished due to its higher intensity (about 1100 a.u.). To the contrary of Granny Smith, the intensity of a region under the cuticle diminished markedly to a value lower than the core of Granny Smith (down to 400 a.u.).

The apparent microporosity maps of the same fruit are shown in Figure 4-6. At one-month storage, apparent microporosity had a similar distribution for the two cultivars with a lower microporosity in the core comparing to the parenchyma. For Granny Smith, parenchyma apparent microporosity was about 50%. In the core, the outer region was less porous than the parenchyma (about 35%) and the inner core apparent microporosity was about 20%. The same value was observed in the vascular bundles and the border between parenchyma and core. For EC, outer parenchyma region was very porous with an apparent microporosity of about 65% or more. In the inner parenchyma this value decreased to 35% close to the core border. In the core the apparent microporosity was low, about 20%. The highest values of apparent microporosity in this study were high compared to the ones obtained in other studies (Herremans et al., 2013; Ting et al., 2013). The measurement method (Musse et al., 2010b) could be responsible by reaching its limits for these highest apparent microporosities and overestimated the true values. The values nevertheless reflect differences between the different cultivars and storage times.

Six months after harvest, the values of T_2^* of highly porous tissue i.e. the core of Granny Smith and under-cuticle region of EC were too low to be accurately fitted for every pixel and resulted in a lack of data for apparent microporosity (Figure 4-6B and D, black regions). Between one and six month storage, the microporosity increased very

slightly in Granny Smith parenchyma (about 5%) and increased markedly in the core (from 35% to over 50% in the voxels in which it was possible to compute apparent microporosity). For EC, the apparent microporosity in the inner parenchyma region did not vary. In the core, it increased and consequently the border between the core and parenchyma could be distinguished with about 20% apparent microporosity. Core region apparent microporosity was about 35%.

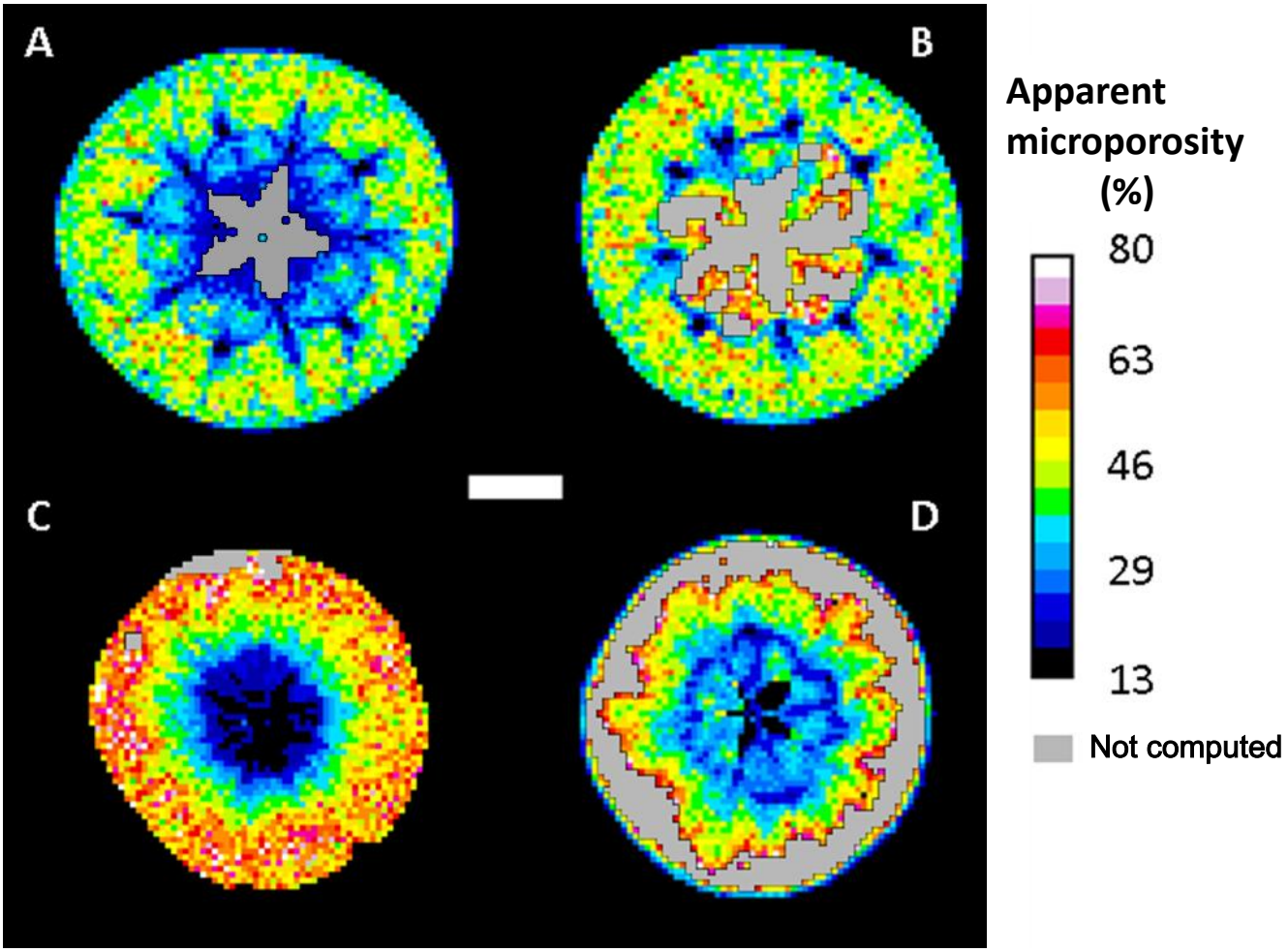

Figure 4-6: Apparent microporosity maps of Granny Smith cultivar one month (A) and six months (B) after harvest and EC one month (C) and six months (D) after harvest. Scale bar is 2 cm.

2) Multi-exponential relaxation and apparent microporosity in specific regions

The results of the multi-exponential T_2 fit, proton density I_0 and apparent microporosity computing on the different ROIs for Granny Smith are shown in Table 4-1:. In the parenchyma, the fitting errors were about 2 ms for T_{21} and T_{22}, and 1 ms for

T_{23} and 0.3% for I_0. The fitting error was slightly superior in the core: about 3 to 6 ms for T_{21} and T_{22}, and 1 ms for T_{23} and 1% for I_{01}, I_{02} and I_{03}. This error may originate from the size of the considered ROIs, which were lower for core tissues, thus lowering the SNR despite the lower apparent microporosity.

Table 4-1: Mean values of multi-exponential fit results, proton density (I_0) and apparent microporosity estimations on ROIs for Granny Smith cultivar one month after harvest

	I_{01} (%)	T_{21} (ms)	I_{02} (%)	T_{22} (ms)	I_{03} (%)	T_{23} (ms)	I_0 (a.u.)	Apparent microporosity (%)
Outer parenchyma	3.2 ± 0.4	27 ± 3	16.6 ± 0.8	130 ± 17	80.2 ± 0.6	528 ± 56	1073 ± 27	48 ± 4
Inner parenchyma	2.7 ± 0.4	24 ± 4	17.6 ± 0.6	108 ± 12	79.7 ± 0.2	458 ± 39	1134 ± 24	46 ± 4
Outer core	4.2 ± 1.4	44 ± 10	16.4 ± 1	137 ± 17	79.4 ± 0.5	544 ± 28	1216 ± 11	29 ± 1
Inner core	5.1 ± 1.2	31 ± 9	26.4 ± 1.9	115 ± 11	68.5 ± 1.3	447 ± 25	1236 ± 3	26 ± 1
Vascular bundles	6.8 ± 0.5	19 ± 4	34.7 ± 2.8	94 ± 5	58.5 ± 3.3	314 ± 18	1369 ± 18	13 ± 1

In the outer core, the T_2 and intensity values were similar to the ones in the outer parenchyma, only T_{21} was different and higher in the outer core (44 ms compared to 27 ms in the outer parenchyma). The apparent microporosity was lower in the outer core (29% compared to 48% in the outer parenchyma). The inner core had T_2 values close to the ones of inner parenchyma but with a higher T_{21}, as in the outer core, and different relative intensities. I_{03} was lower while I_{02} and I_{01} were higher suggesting a different distribution of intracellular water. The vascular bundles had transverse relaxation times and relative intensities very different from the parenchyma. I_{03} represented only 58.5% of the total intensity while I_{02} and I_{01} had consequently higher contributions than in parenchyma (respectively 34.7% and 6.8% in bundles comparing to 16.6% and 3.2% in outer parenchyma). T_{23} (314 ms), T_{22} (94 ms) and T_{21} (19 ms) were lower than in outer parenchyma (528 ms, 130 ms and 27 ms, respectively).

I_0 in vascular bundles was higher than in other tissues, which was expected due to the lower apparent microporosity of the vascular bundles. It was also higher in the core (1216 and 1236 a.u. for outer and inner core, respectively) than in the parenchyma

(1073 and 1064 a.u. in outer and inner parenchyma, respectively) in agreement with the apparent microporosity (29% and 26% apparent microporosity in outer and inner core versus 48% and 46% for outer and inner parenchyma).

Table 4-2: Mean values of multi-exponential fit results, proton density (I_0) and apparent microporosity estimations on ROIs for EC one month after harvest

	I_{01} (%)	T_{21} (ms)	I_{02} (%)	T_{22} (ms)	I_{03} (%)	T_{23} (ms)	I_0 (a.u.)	Microporosity (%)
Outer parenchyma	1.2 ± 0.2	17 ± 1.2	18.0 ± 0.5	83 ± 6	80.8 ± 0.4	360 ± 29	908 ± 28	54 ± 2
Inner parenchyma	2.8 ± 0.9	23 ± 16	21.8 ± 2.5	87 ± 8	75.4 ± 2.0	331 ± 26	1151 ± 46	35 ± 5
Core	3.2 ± 0.4	16 ± 3	26.1 ± 0.7	88 ± 4	70.7 ± 0.9	335 ± 18	1292 ± 28	19 ± 3

At one month after harvest, the core of EC had T_2 values corresponding to those measured in the inner parenchyma. I_{02} was higher and I_{03} was lower in the core than in the parenchyma and the apparent microporosity was lower (Table 4-2).

As for Granny Smith, I_0 was higher in the core (1292 a.u.) than in the parenchyma (908 a.u. and 1151 a.u. for outer and inner parenchyma, respectively) in accordance with the values of the apparent microporosities measured in these tissues (19%, 54% and 35% in core and in outer and inner parenchyma, respectively): the lesser amount of the water in the tissue, the lower the intensity.

Evolution of the relaxation signal during storage

Table 4-3 shows the MRI T_2 relaxation parameter values six months after harvest for Granny Smith. As for one-month storage, three components were extracted from the signal. A Student t test was performed to assess the significance of the variations between the two measurement times. The main changes occurred in the outer core tissue, for which all the relaxation times decreased (T_{21} -28 ms, T_{22} -33 ms and T_{23} -90 ms) together with I_0 (-326 a.u.), while apparent microporosity increased (+19%). Variations were also observed in vascular bundles for I_{03} and I_0 (+6.4% and -86 a.u., respectively) and in outer parenchyma for I_{03} (+2.5%).

Table 4-3: Mean values of multi-exponential fit results, proton density (I_0) and apparent microporosity estimations on ROIs for Granny Smith cultivar six months after harvest. * and ** indicate significant variations between one and six months after harvest ($p<0.05$ and $p<0.01$, respectively).

	I_{01} (%)	T_{21} (ms)	I_{02} (%)	T_{22} (ms)	I_{03} (%)	T_{23} (ms)	I_0 (a.u.)	Apparent microporosity (%)
Outer parenchyma	2.0 ± 0.1	36 ± 7	15.3 ± 0.4	143 ± 4	82.7 ± 0.3 *	566 ± 14	1050 ± 4	44 ± 2
Inner parenchyma	2.5 ± 0.4	37 ± 15	16.1 ± 1.3	117 ± 2	81.5 ± 1.0	474 ± 17	1103 ± 9	39 ± 1
Outer core	2.2 ± 0.6	16 ± 5 **	17.4 ± 1.7	104 ± 10 *	80.3 ± 2.1	453 ± 37 *	890 ± 64 **	48 ± 6 **
Inner core	2.4 ± 1.5	15 ± 13	21.7 ± 2.7	87 ± 34	75.8 ± 4.1	382 ± 63	1030 ± 217	38 ± 16
Vascular bundles	5.0 ± 1.0	17 ± 3	30.1 ± 2.3	107 ± 6	64.9 ± 3.2 *	341 ± 18	1283 ± 10 *	14 ± 1

Different variations were observed for EC. Table 4-4 shows the MRI T_2 relaxation parameters and their variations; the variations for under-cuticle region were computed comparing to the parameters of the outer parenchyma measurement at one month after harvest.

Table 4-4: Mean values of multi-exponential fit results, proton density (I_0) and apparent microporosity estimations on ROIs for EC six months after harvest. * and ** indicate significant variations between one and six months after harvest ($p<0.05$ and $p<0.01$, respectively)

	I_{01} (%)	T_{21} (ms)	I_{02} (%)	T_{22} (ms)	I_{03} (%)	T_{23} (ms)	I_0 (a.u.)	Apparent microporosity (%)
Parenchyma (outer)	3.7 ± 0.9 *	17 ± 1	18.7 ± 0.3	98 ± 3	77.6 ± 1.2	379 ± 20	835 ± 164	49 ± 3
Parenchyma (inner)	3.9 ± 0.6	22 ± 4	22.1 ± 0.4	97 ± 4	74.0 ± 0.2	331 ± 2	1009 ± 99	34 ± 1
Under-cuticle	NA	NA	21.2 ± 8.3	41 ± 1 **	78.8 ± 8.3	241 ± 45 **	490 ± 24 **	68 ± 1 **
Core	4.4 ± 2.9	21 ± 3	23.8 ± 7.6	96 ± 1 *	71.8 ± 10.5	345 ± 33	1057 ± 43 **	31 ± 2 **

The data corresponding to the under-cuticle region were better fitted by a two-exponential T_2 decay than by a tri-exponential fit used in other analyses. The region

considered here had moreover relatively short T_{22} and T_{23} (41 ms and 241 ms, respectively), which decreased markedly as well as I_0 when compared to the outer parenchyma region at one month after harvest (-42 ms and -119 ms, -421 a.u., respectively). Apparent microporosity increased for the same storage time difference (+14%). This region behaved like the outer core in Granny Smith cultivar. On the other hand, the other regions of the fruit showed only little variations between one- and six-month storage except for an increase in apparent microporosity and a loss of I_0 within the core (+12% and -234 a.u., respectively).

III. Discussion

In the experimental conditions of the present study (no T_1 weighting and no solid proton contribution), the variation of I_0 computed from the MSE sequence would be explained by a variation of the water content or/and a variation of the apparent microporosity in the tissue. Figure 4-7 showed the relationship between I_0 and apparent microporosity. In the present case, a strong linear correlation ($R^2 = 0.811$) was observed between I_0 and apparent microporosity for all data, except the three points corresponding to under-cuticle region of EC apples six months after harvest. This correlation shows that the variation of I_0 is mainly explained by a variation of microporosity. The exceptions were the three under-cuticle samples, where microporosity alone cannot explain the results which could thus be explained by both microporosity and water content effects. This hypothesis is supported by the fact this region shrank during storage, probably due to a loss of water. Another important factor could be that due to the high value of microporosity, the hypotheses for the calculus (low microporosity, spherical inclusions) no longer hold, thus inducing a bias in the computation. These results validate the implementation of a combined MRI approach for the determination of the water content from proton density image. Indeed, the apparent microporosity map can be used to correct the proton density map from microporosity variation, in order to extract the water variation only.

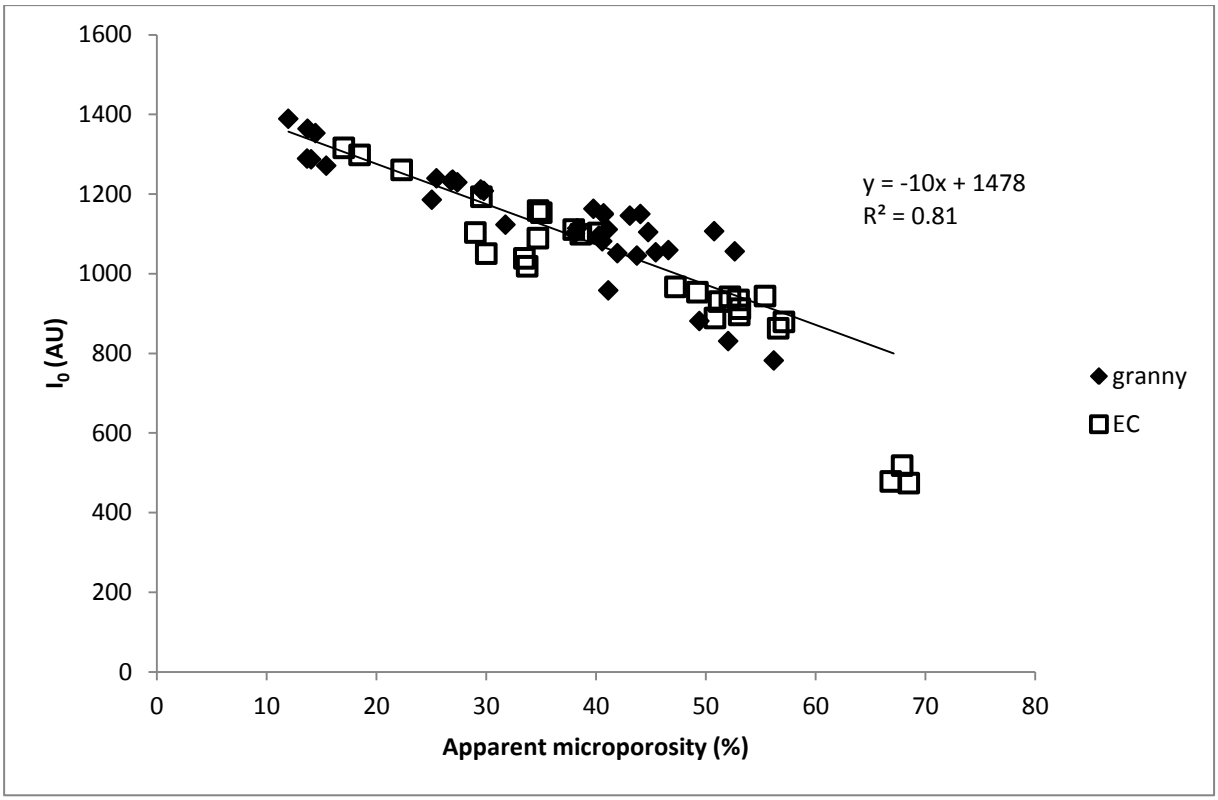

Figure 4-7: Graph showing the relation between I_0 fitted from tri-exponential relaxation decay and apparent microporosity for the two cultivars.

Water contents of EC in outer and inner parenchyma measured at one month after harvest were the same (85.9 ± 0.9 and 86.4 ± 1.0) despite the different porosity values. This observation and the linear relationship between I_0 and apparent microporosity suggest that all the samples except the under-cuticle region from EC at six-month storage had a similar water content. So considering the sample with the same I_0 (and therefore water content) and same apparent microporosity, we observed however variation of the relaxation times. For example, in Granny Smith at one month after harvest (Table 4-1), apparent microporosity and I_0 of inner and outer parenchyma were similar (48 ± 4% and 46 ± 4%, 1073 ± 27 a.u. and 1134 ± 24 a.u.), while T_{23} decreased (528 ± 4% 56 ms and 458 ± 39 ms) and T_{22} increased (108 ± 12 ms and 137 ± 17 ms) from the outer parenchyma to the parenchyma. An opposite phenomenon was observed for the core with a low apparent microporosity but the same range of the T_{22} and T_{23} for outer core and outer paramenchyma and intra core and intra parachenchyma tissue. in EC at one month after harvest (Table 4-2) a constant relaxation times from inner parenchyma to core tissues (T_{23}, 331 ± 26 ms and 335 ± 18 ms, T_{22} 87 ± 8 ms and 88 ± 4

ms), was also observed while the apparent microporosity decreased markedly (35 ± 5% and 19 ± 3%) and I_0 increased (1151 ± 46 a.u. and 1292 ± 28 a.u.). As intensity is often linked to water content, this study highlights the important influence of microporosity changes which have to be taken into account.

Concerning relative signal intensities, it has been demonstrated in the literature (Adriaensen et al., 2013) that an increase in microporosity tends to decrease a relative signal intensity of longer T_2-components. In our measurements, I_{03} and I_{02} of 79.7 ± 0.2% and 17.6 ± 0.6% in inner parenchyma of Granny Smith at one month after harvest corresponded to an apparent microporosity of 46 ± 4% while I_{03} and I_{02} of 68.5 ± 1.3% and 26.4 ± 1.9% in inner core of Granny Smith at one month after harvest corresponded to an apparent microporosity of 26 ± 1%). These results indicate microporosity was not responsible for the signal variations observed. The relaxation time and relative intensity variations observed did thus not originate from changes in apparent microporosity or water content but from a change in tissue/cell structure, such as changes in membrane permeabilities, or chemical content. In chapter 2 a strong correlation has been observed between the relative intensity I_{02} and I_{03} for parenchyma tissue from different apple cultivars. This correlation was also observed in the core and the parenchyma for EC and Granny apples and confirms that a water exchange mechanism between two water pools could be generalized, as expected from the vacuole and cytoplasm attribution.

The vascular bundles had a particularly low T_2. They are known to have a particular structure with heterogeneous cells (phloem cells, surrounded on one side by sclerenchyma cells and on the other side by xylem cells) which sizes range from a few micrometer to about 30 µm. They are embedded in parenchyma cells of increasing size with the distance to the bundle (Albersheim et al., 2010b). If the T_2 value of the bundles-associated ROIs was explained by cell size only, considering the model previously used linking T_2 to cell size (Van der Weerd et al., 2001; chapter 2), a longest relaxation time (T_{23}) of 314 ms measured would correspond to a mean cell size over the three dimensions of 95 µm. The lower T_{23} would thus be due to a change in cell size. The increase in I_{02} and the decrease in I_{03} are coherent with previous observations in parenchyma and core.

During storage, the most important changes happened in outer core for Granny Smith and under-cuticle region for EC, which had the similar behavior, i.e. I_0 decreased,

porosity increased and relaxation times decreased. These observations suggest a loss of water in the two tissues (and to a lesser extent in the core of EC). As the relative intensities did not vary, this change did not affect cell structure and the relationships between water pools. Two different drying processes may thus occur for the two fruit. Granny Smith lost water from the outer core, certainly via the vascular bundles as outer core is the closest tissue to these bundles, whereas EC lost water through cuticle. Cuticle is known to change during storage and particularly to have a role in regulating water loss, chemical attacks, mechanical injuries and microbial infections (Lara et al., 2014). In particular, water diffusion coefficients have been studied in this tissue to understand the fruit dehydration (Veraverbeke et al., 2003a) and a model of moisture loss during storage was established (Veraverbeke et al., 2003b, c). These studies showed that the wax layer had the lower water diffusion coefficient and was responsible for limiting water loss. Important differences in the wax layer according to cultivar and storage times were observed together with a structural reorganization in the whole cuticle. Moisture loss was also linked to changes in the mechanical properties of the fruit and turgor pressure (reviewed in (Lara et al., 2014)). In our study, browning was observed for EC after six months harvest in the same region water loss presumably occurred (under-cuticle layer). Both phenomena suggest a permeability of cuticle which may be caused by cracks as reported for grape berry and tomato (Becker and Knoche, 2012; Matas et al., 2005) leading to moisture loss and hypothetically infections. During or as a consequence of the process, a decrease of T_{23} and T_{22} relaxation times was observed. The fact this decrease is observed in both compartments suggests exchanges occur and supports the attribution to vacuole and cytoplasm. It also is in agreement with previous study in which slow drying was applied to apples (Mariette et al., 1999) and resulted in a lowering of all relaxation times. On the other hand, the shortest component of the MRI signal disappeared so that a bi-exponential relaxation was obtained. This disappearing of the shortest T_2 component in apples at six-month storage times was also observed for Florina fruit (chapter 2) and was linked to a cell structural change leading to an increase in relaxation time of the shortest T_2 component merging with medium T_2 components. This change could be an increase in apoplast water content (see chapter 2).

IV. CONCLUSION

The results in this study showed the two main proton pools relaxation times and intensities were strongly linked, supporting the hypothesis of exchanges occurring and their attribution to vacuole and cytoplasm.

MRI allowed a good characterization of the different tissues. Different relaxation times and water distribution were observed in parenchyma, core and vascular bundles regions reflecting different structures and/or chemical compositions. From the cuticle to the core, a gradient in relative intensities was observed, I_{02} intensity increasing and I_{03} decreasing reflecting a progressive structural change: cytoplasm represents a more important fraction of cell water in the core than in the outer tissue.

During storage, the two cultivars studied lost water and their tissue structure was affected: apparent microporosity increased and I_0 decreased. The drying process did not alter the structure (relative intensities did not vary) but lowered the relaxation times. Two different parts of the fruit were affected: for Granny Smith, the modifications happened in the core while it was mainly in the under-cuticle region for EC. These different behaviors are postulated to be due to different cuticle structures.

I_0 was demonstrated to be affected by microporosity. I_0 mapping thus does not reflect only water content but the later could be accessed by measuring apparent microporosity and I_0, which is of particular interest for non-destructive quality assessment in fruit.

General discussion and perspectives

5. General discussion and perspectives

MRI multi-exponential relaxation time measurements were for the first time applied to apple fruit to characterize the spatial heterogeneity of its parenchyma in terms of water status and subcellular distribution. Three T_2-components were extracted from the CPMG decay curve. Microporosity of apple fruit was also investigated using the method described in the literature (Musse et al., 2010b). The spatial resolution of the MRI images allowed selecting homogeneous regions in the parenchyma and to study the effect of cell size and microporosity on the relaxation time T_2 distribution. Moreover, by applying a multi-instrumental approach, links between mechanical properties, MRI multi-exponential relaxation parameters, microstructure (microporosity, cell size) and chemical composition (soluble solid content, cell wall composition) were shown. Finally, studying the evolution of the different apple fruit tissues revealed cultivar-dependent phenomena linked to a loss of water in the fruit during storage and a general behavior of the relaxation time. However, these studies raised several questions that merit to be addressed to improve our understanding of apple physiology in relation with qualitative characteristics depending on water status and tissue microstructure.

In the first part of this chapter, methodological aspects of MRI measurements in fruit will be discussed. A second part will focus on the model used to interpret relaxation times and intensities distributions and on the different biochemical and physiological parameters which induce modifications of these T_2 distributions. The last part of this chapter will concern perspectives regarding microstructural and water status characteristics gained by quantitative MRI in relation with apple physiology and related tissue mechanical properties.

I. MRI MEASUREMENTS AND DATA ANALYSIS

By applying a multi-exponential MRI approach, a better characterization of the different tissues of apple fruit was achieved. In fact, tissues with close mono-exponential relaxation times (e.g. EC inner parenchyma and core, see Chapter 4) were shown to differ in relative intensities and thus in subcellular structure.

In this study, all multi-exponential fittings were performed with the Levenberg-Marquardt algorithm. The latter is the most commonly non-linear regression method used for fitting exponential decays. The main critics to this method are the need to have an a priori on the number of exponential functions and that it may be sensitive to parameter initialization. Improvement of this fitting can be achieved using a more robust algorithm. More sophisticated methods that do not require a priori knowledge of the number of exponential term have been proposed (Mariette et al., 1996; Song et al., 2002). For example, the maximum entropy method used in NMR relaxometry (Duval et al., 2005), provide a continuous distribution of the relaxation times (Figure 5-1). This method could be used to improve the fitting in quantitative MRI taking into account the demanding high signal to noise ratio. Comparing this method with the Levenberg-Marquardt fitting method which was used in this work resulted in very similar estimations for Granny Smith outer cortex region as illustrated on Figure 5-1.

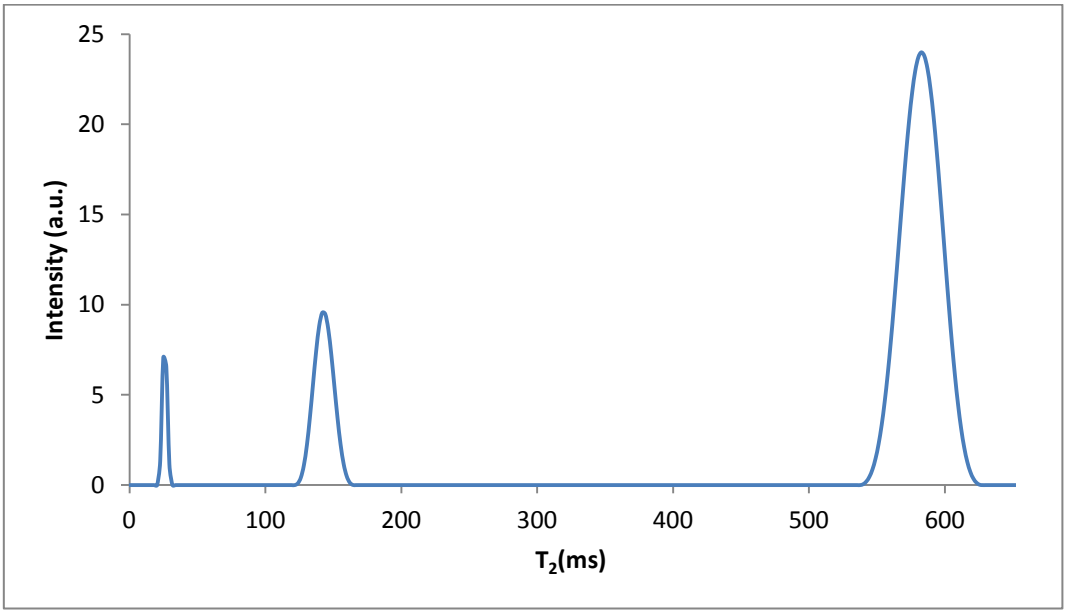

	I_{01} (a.u.)	I_{01} (%)	T_{21} (ms)	I_{02} (a.u.)	I_{02} (%)	T_{22} (ms)	I_{03} (a.u.)	I_{03} (%)	T_{23} (ms)
MEM	36.2	3.3	22.5	174	15.7	139	894	80.9	580
Marquardt	38.2	3.5	29	174	15.7	146	892	80.8	584

Figure 5-1: Example of the results of Maximum Entropy Method applied to the MRI decay of the outer parenchyma of Granny Smith apple and Levenberg-Marquardt fitting results on the same data, SNR/pixel on shortest echo was 118 and the ROI consisted of 339 voxels.

A better characterization of the heterogeneity of the fruit could also be achieved by obtaining multi-exponential relaxations on voxels rather than on ROIs. In particular, for heterogeneous regions in terms of cell size and structure like vascular bundles and surrounding tissues, a mean value over the region does not allow identifying the origins of the relaxation variation (see chapter 3). To achieve a multi-exponential mapping, a better signal to noise ratio (SNR) is necessary. Different solutions exist, for example, by applying de-noising filters to the signal. Reducing the echo time could also improve the robustness of the fitting due to a more frequent refocusing but this solution requires higher gradients and shorter excitation pulses. Increasing the number of scans registered during measurements and thus decreasing the noise is another option to improve SNR. In this study, the measurement time was one hour per fruit because of the long repetition time required for multi-exponential T_2 measurements (10 s). Preliminary assays with increased repetitions showed that for accurate T_2 maps, the measurement time had to be increased up to few hours per fruit, which can hardly be considered for applications. Using higher field MRI scanners could improve the SNR and allow a multi-exponential T_2 mapping but microporosity would then have a greater effect on relaxation times. More sensitive emitter/receiver coils could improve the SNR (Black et al., 1993). Reducing temperature can also increase the signal intensity because of Curie's law. It can also decrease the T_1 and thus allow shortening measurement time. The only limitation to consider is the effect of temperature on T_2. If the shortest T_2 becomes too small with a same echo time, its determination will become difficult.

Microporosity was shown to affect (mono-exponential and multi-exponential) relaxation times and relative intensities (MRI I_{03} is overestimated and I_{02} underestimated when compared to NMR intensities (Adriaensen et al., 2013)). In this study, the influence of other parameters on T_2 relaxation predominated (see chapter 1). To estimate the precise influence of microporosity on the signal, a perspective would be measuring the same fruit with varying porosities at different magnetic fields, as magnetic field is known to affect microporosity estimation (Musse et al., 2010b).
Additionally, knowing the exact contribution of microporosity to I_0 could allow accessing the water content from I_0 measurements (see chapter 3).

From a theoretical point of view, apparent microporosity estimation is based on the assumption of spherical pores (Musse et al., 2010b). This is clearly not the case in

apple, in particular near the core. A solution could then be to consider other geometries like ellipsoids (Sukstanskii and Yablonskiy, 2003).

Finally, the multi-exponential MRI fit did not led to a 4-component relaxation as often reported in NMR relaxometry (Adriaensen et al., 2013; Marigheto et al., 2008; Sibgatullin et al., 2007). In fact, the minimum echo time (TE) used in the MRI experiment was 7.1 ms. The shortest transverse relaxing component measured by NMR is between 10 and 30 ms, representing only 2-5 % of the total signal intensity (Adriaensen et al., 2013; Marigheto et al., 2008; Sibgatullin et al., 2007), would correspond to a MRI relaxation time between 5 and 13 ms according to Adriaensen et al. (Adriaensen et al., 2013). This component characterized by short relaxation times and low signal could not be accessed with the experimental conditions of the present study; TE of the imaging sequence would have to be lowered.

In lights of the present results, the ideal case would be to be able to measure fruit at lower temperatures with a better receive coil at low-field with a MRI system equipped with high gradients, in accordance with previous studies (Van As, 2007).

To summarize, the challenge is to lower the field in order to limit the effect of microporosity on T_2 measurements but also to keep a high enough SNR for accurate multi-exponential T_2 fitting and for apparent microporosity estimation.

II. RELAXATION MECHANISM IN APPLE

MRI studies in literature mainly focused on mono-exponential T_2 measurements and identification of tissue defects (Barreiro et al., 2002; Cho et al., 2008b; Melado-Herreros et al., 2013). By applying a multi-exponential relaxation, the cell water distribution was accessed. The NMR relaxation model used for the interpretation of the relaxation data in the present work was based on previous studies which associated the longest relaxation component (T_{23}) to the vacuole, the second relaxation time (T_{22}) to the cytoplasm and the shortest one (T_{21}) to the cell wall/extracellular water.

In this study, the longest T_2 component (350-600 ms) represented roughly 75 to 85% of the signal and thus of the cell water amount. Its MRI relaxation time was 350-

600 ms corresponding to 850-1450 ms in NMR (Adriaensen et al., 2013). These observations were in agreement with the attribution of the longest relaxing component to the vacuole as previous works usually estimated its intensity to about 75-81% of the signal and a relaxation time of 1000-1250 ms (Adriaensen et al., 2013; Hills and Remigereau, 1997; Sibgatullin et al., 2007; Snaar and Van as, 1992). The second most important T_2 component in terms of intensity and relaxation time represented in this study 13-19% of the signal with a relaxation time of 80-140 ms, which corresponded with a T_2 around 190-350 ms in NMR (Adriaensen et al., 2013; Hills and Remigereau, 1997; Sibgatullin et al., 2007; Snaar and Van as, 1992), in agreement with previous studies (intensity of 10-15% and relaxation time of 190-400 ms) (Adriaensen et al., 2013; Hills and Remigereau, 1997; Sibgatullin et al., 2007; Snaar and Van as, 1992). This component is generally attributed to the cytoplasm as its lower relaxation time than the vacuole water could be due to its crowding by many organelles and high amount of proteins (Figure 1-3). The present results showed a strong correlation between the two longer T_2 components (Chapter 3) supporting their attribution to the vacuole and the cytoplasm water, which interact through the tonoplast membrane. On the other hand, as the cytoplasm contains many organelles, it is also possible that different relaxation times exist in that compartment associated to organelles that would contribute to faster relaxation times. The third component obtained in this study (1-4% of the signal) had the shortest relaxation time (15-30 ms in MRI, corresponding to 35-70 ms in NMR (Adriaensen et al., 2013; Hills and Remigereau, 1997; Sibgatullin et al., 2007; Snaar and Van as, 1992)). In previous works, the intensity of the third component was slightly higher (6-9%) and its relaxation times ranged between 30 and 105 ms (Hills and Remigereau, 1997; Sibgatullin et al., 2007; Snaar and Van as, 1992). In this discussion, extracellular water will qualify water in the apoplast, as opposed to water in the cell wall. In NMR studies, a fourth component is often identified (Adriaensen et al., 2013; Marigheto et al., 2008; Sibgatullin et al., 2007) with a relaxation time of between 10 and 30 ms (which would correspond to a relaxation time of 4-13 ms in MRI) and an intensity of 2-5 % and was attributed to water closely interacting with the cell wall (Marigheto et al., 2008; Sibgatullin et al., 2007) as it also corresponded to the mono-exponential relaxation time of apple rehydrated cell wall (Hills and Duce, 1990). Preliminary NMR results on the effect of temperature on multi-exponential relaxation times showed a good correlation between the relaxation times of the two shortest components,

supporting their attribution to the water in cell wall and the apoplast which are two water pools in strong interaction (Figure 5-2). Diffusion between compartments or neighboring cells (via plasmodesmata) also complicates attributions as it mixes the magnetization depending on cell compartment geometry and membrane permeability.

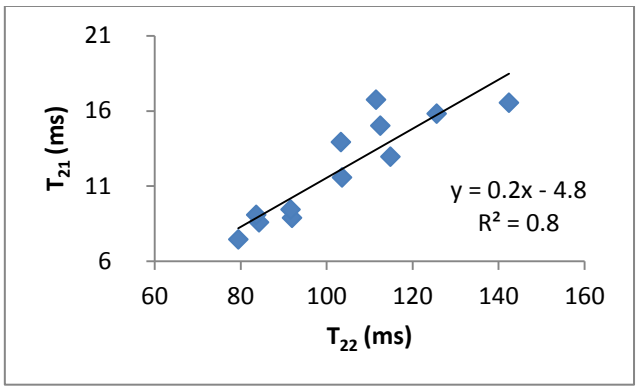

Figure 5-2: Plot of T_{21} as a function of T_{22}, results from a 4-component multi-exponential fit on NMR data (Bruker Miniscpec 20 Mhz, τ=0.5 ms) of two samples of Jonagored apple parenchyma at different temperatures from 5°C to 40°C

Cell wall of ripening fruit were shown by photonic microscopy to swell depending on species (Redgwell et al., 1997). Our results showed that the shortest MRI component lost intensity when the tissue damping factor increased (chapter 2) and this phenomenon was also linked to a change in tissue firmness. A four-component multi-exponential study of the relaxation times of ripening fruit combined with photonic microscopy could thus provide information about the components of water in cell wall and apoplast and eventually establish links between these compartments and the mechanical behavior of the tissue (see chapter 2).

Until now, the interpretation of the multi-exponential T_2 times generally considered only the cell structure and did not take into account the variation of the cell size or the tissue structure itself inside the sample. However, it was recently demonstrated that the multi-exponential behavior of the relaxation in leaf can be explained by the different cell size in the tissue sample (Musse et al., 2013). So at the voxel scale, the heterogeneity of the cells in the voxel could also complicate the signal due to different cell structure and/or size, as can be observed for example in the vascular tissue. The same compartment in different cells could thus contribute to

different components (if some cells are not vacuolated for example). To characterize this effect, the signal could be studied by varying voxel size.

The validity of the relaxation time components attribution to the cell compartments will now be considered taking into account the different potential variable factors: cell size, chemical composition and temperature.

1) Cell size

Cell size was found to influence the relaxation times although cell size variations were small in apple fruit. The link between T_2 and cell size was demonstrated for the Fuji cultivar. This relationship allowed estimating the magnetization sink strength parameter, which was found to be slightly higher than in previous studies (see chapter 1). A better characterization of this phenomenon would require widening the range of cell sizes studied. For example, studying fruit during the growing period, in which cell size increases or genotypes with smaller fruit, would be a solution (assuming similar chemical composition, which is not likely to be true). The relationships between cell size and T_2 could also be improved by the accuracy of the cell size measurement. Indeed, different ways of improvements can be suggested. First the microscopic technique itself: due to the different cell sizes, the macro-vision images of samples sometimes showed overlaying cells (see Figure 5-3, EC and Granny Smith had overlaying cells to the contrary of Fuji caliber). To have a better cell size estimation, confocal microscopy could be used. Results on tomato (Legland et al., 2012) showed the gain of resolution by this technique but also showed its limits as only small regions are imaged and the measurements are time-consuming on the contrary of macro-vision, which is fast and provided large field of view images of tissues. Second, as the regions considered in the parenchyma are known to be homogeneous (Khan and Vincent, 1990; chapter 2), the model attributing vacuole to the longest relaxation time is likely to be correct. Precisely measuring the size of the vacuole compartment instead of the whole cell would thus allow a more accurate study of the relationship between compartment size and relaxation time. Light microscopy would allow such measurement, as has been done in senescing oilseed rape leaves (Musse et al., 2013). Finally, image analysis on apples could not differentiate cells from intercellular spaces. Although a differentiation

between them was made in tomato (Devaux et al., 2008), it was not possible to apply it on apple images due to the large various intercellular spaces sizes that can be of the size of cells.

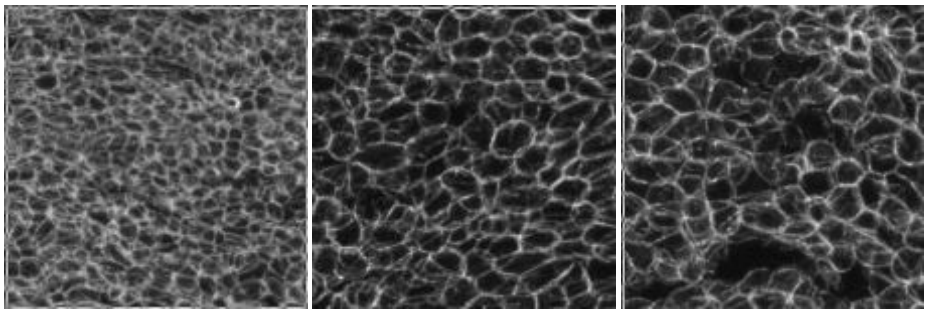

Figure 5-3: Macrovision images of 2.1 mm^2 from EC, Fuji (caliber 1) and Granny fruit respectively

2) Chemical composition

The chemical composition of samples is a parameter affecting the relaxation signal. Apple contains soluble sugars, organic acids, phenolics and several ions, the main ones being calcium, magnesium, phosphorus and potassium. Increase in sugar content is known to decrease relaxation time depending on their nature (Desbois, 1992) but the effect of ions at biological concentrations is unknown. However, the results of this study showed no correlations between soluble solid content and relaxation times (see chapter 2). A more detailed study on the relation between the nature and concentration of ions and other components (i.e. phenolics) on the signal would nevertheless be of particular interest. For example, the EC cultivar which had the shortest relaxation times of all the cultivars studied presented red heterogeneous tissues due to the presence of anthocyanin. This phenolic compound is known to decrease relaxation times depending on its concentration (Kaku et al., 1992).

From a metabolic point of view, ions are involved in various cell processes. Calcium, for example, is widely studied for its role on fruit postharvest (Aghdam et al., 2012). Experiments involving Gd^{3+} or other contrasting agents as probes (Bonnet and Toth, 2010) could also be helpful to understand ion interactions in the cells by achieving its subcellular and tissue localization by multi-exponential MRI.

3) Temperature

NMR relaxation is also a good probe for thermal process, which could also improve understanding of the relaxation. For example, the temperature effects between freezing and cell rupture at about 50°C (Gonzalez et al., 2010; Maheswari et al., 1999) could bring information on the different compartments behavior. Indeed, according to Curie's Law the NMR signal intensity decreases with temperature and the T_2 increases with temperature in agreement with an Arrhenius relation. So the study of the behavior of each T_2 component would provide a way to validate the NMR model of interpretation. Preliminary NMR results from Jonagored apple parenchyma samples (cylinders of 5 mm diameter and 1 cm height) measured between 5 to 40 °C were done. Two different behaviors of T_2 were identified. Between 5 to 25 °C, the specific variation of the longest T_2 component (Figure 5-4B) was clearly in agreement with its attribution to the vacuole. The absence of T_2 variation for the other components was in support of a more constrained water environment such as in the cytoplasm or in the cell wall (Figure 5-4A). After 25 °C, variation of the cellular structure occurred, leading to a different behavior of the signal. This change could be due to modifications in membranes permeability affecting exchanges between compartments/neighboring cells and especially the exchange between the vacuole and the cytoplasm (a faster exchange would induce a lower relaxation time for the vacuolar compartment).

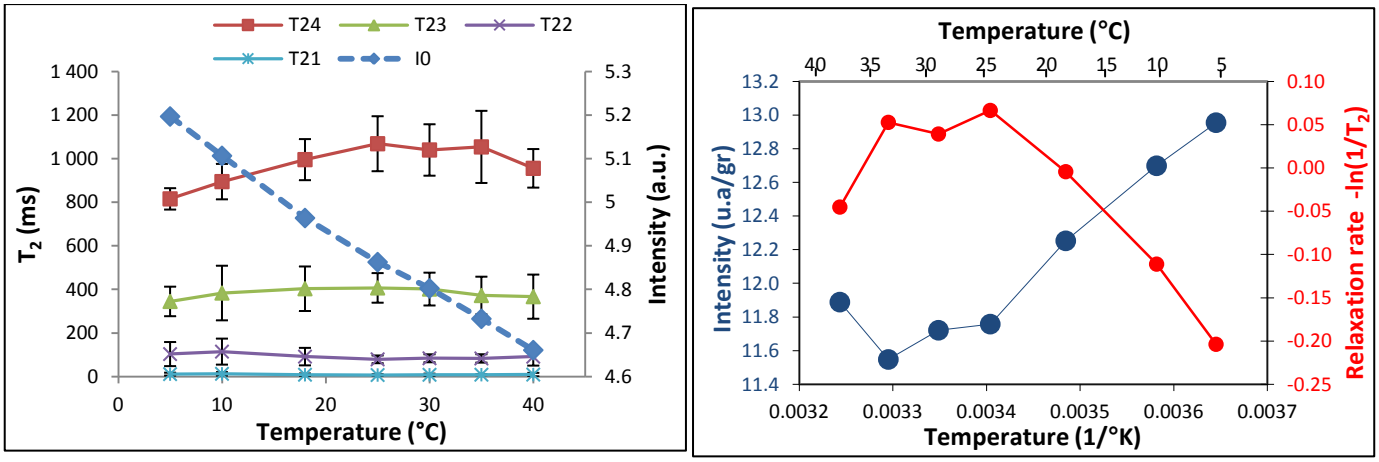

Figure 5-4 (A) Relaxation times and I_0 as a function of temperature and (B) Intensity and relaxation rate for the longest T_2 component of the 4-components multi-exponential signal of Jonagored apple parenchyma as measured by NMR (20 MHz, τ=0.5 ms)

These preliminary results warrant further studies on the effect of temperature, which could lead to a better understanding of the exchanges between compartments and to the identification of the temperature range at which the fruit can be best studied by MRI/NMR.

III. APPLE MECHANICAL PROPERTIES AND PHYSIOLOGY

The study of the mechanical properties of apple (chapter 2) showed that it was necessary to consider both elastic and viscous behaviors of the tissue. The current model explaining the mechanical properties of the fruit is based on the mechanical properties of the cell wall, associated with the intercellular spaces. Turgor pressure has also been linked to mechanical properties but is strongly correlated with the cell wall behavior (Singh et al., 2014).

In the cell wall, this study showed pectin and hemicellulose have a role in the mechanical behavior of the tissue. Results of chapter 2 suggested that these different components influenced differently viscous and elastic response of the tissue. To further study these effects, a higher number of sample should be measured and the role of cellulose could also be estimated. As mechanical properties change during storage (Alamar et al., 2008), following fruit with the same pre-harvest life could help minimizing external sources of variations to focus on the ones evolving during storage. In such as study, MRI could also help sampling different regions in the same fruit for which mechanical properties and chemical contents may vary.

Finally, as mechanical properties are strongly linked to texture, a texture assessment by sensory analysis of the samples would allow linking MRI and mechanical measurements directly to texture determinants. Such a combined assessment could contribute to the improvement of instrumental measurements of texture particularly during storage. Furthermore, MRI tri-exponential relaxation and apparent microporosity measurements in fruit parenchyma tissue that were shown to differentiate apple cultivars could be used to differentiate phenotypes in a selection program. The good correlations between MRI and mechanical measurements make MRI a powerful tool to potentially distinguish soft fruit from hard fruit. This makes

quantitative MRI a promising extension of MRI developments for online fruit quality assessment (Barreiro et al., 2002; Zhang and McCarthy, 2013).

To conclude, the results presented in this thesis demonstrated the interest of MRI approach for characterizing the fruit tissues according to water status and distribution and porosity. A better understanding of mechanisms implied in the NMR relaxation and of the relative influence of the structural and composition parameters on mechanical properties of the tissues was achieved.

REFERENCES

References

Abbott, J.A., 1999. Quality measurement of fruits and vegetables. Postharvest Biol. Technol. 15, 207-225.

Abbott, J.A., 2004. Textural quality assessment for fresh fruits and vegetables. Advances in Experimental Medicine and Biology 542, 265-279.

Abbott, J.A., Lu, R., 1996. Anisotropic mechanical properties of apples. Transactions of the ASAE 39, 1451-1459.

Adriaensen, H., Musse, M., Quellec, S., Vignaud, A., Cambert, M., Mariette, F., 2013. MSE-MRI sequence optimisation for measurement of bi- and tri-exponential T2 relaxation in a phantom and fruit. Magnetic Resonance Imaging 31, 1677–1689.

Aghdam, M.S., Hassanpouraghdam, M.B., Paliyath, G., Farmani, B., 2012. The language of calcium in postharvest life of fruits, vegetables and flowers. Sci. Hortic. 144, 102-115.

Alamar, M.C., Vanstreels, E., Oey, M.L., Molto, E., Nicolai, B.M., 2008. Micromechanical behaviour of apple tissue in tensile and compression tests: Storage conditions and cultivar effect. J. Food Eng. 86, 324-333.

Albersheim, P., Darvill, A., Roberts, K., Sederoff, R., Staehelin, A., 2010a. Biochemistry of the cell wall molecules, Plant cell walls. Garland Science, pp. 67-117.

Albersheim, P., Darvill, A., Roberts, K., Sederoff, R., Staehelin, A., 2010b. Cell walls and plant anatomy, Plant cell walls. Garland Science, pp. 1-42.

Assor, C., Placet, V., Chabbert, B., Habrant, A., Lapierre, C., Pollet, B., Perre, P., 2009. Concomitant changes in viscoelastic properties and amorphous polymers during the hydrothermal treatment of hardwood and softwood. J. Agric. Food Chem. 57, 6830-6837.

Bain, J.M., Robertson, R.N., 1951. The physiology of growth in apple fruits. I. Cell size, cell number, and fruit development. Australian journal of scientific research. Ser. B: Biological sciences 4, 75-107.

Bakker, C.J.G., de Roos, R., 2006. Concerning the preparation and use of substances with a magnetic susceptibility equal to the magnetic susceptibility of air. Magn.Reson.Med. 56, 1107-1113.

Barbacci, A., Lahaye, M., Magnenet, V., 2013. Another Brick in the Cell Wall: Biosynthesis Dependent Growth Model. PLoS One 8.

Barreiro, P., Moya, A., Correa, E., Ruiz-Altisent, M., Fernandez-Valle, M., Peirs, A., Wright, K.M., Hills, B.P., 2002. Prospects for the rapid detection of mealiness in apples by nondestructive NMR relaxometry. Appl. Magn. Reson. 22, 387-400.

Barreiro, P., Ortiz, C., Ruiz-Altisent, M., Ruiz-Cabello, J., Fernandez-Valle, M.E., Recasens, I., Asensio, M., 2000. Mealiness assessment in apples and peaches using MRI techniques. Magnetic Resonance Imaging 18, 1175-1181.

Barreiro, P., Ruiz-Cabello, J., Fernandez-Valle, M.E., Ortiz, C., Ruiz-Altisent, M., 1999. Mealiness assessment in apples using MRI techniques. Magnetic Resonance Imaging 17, 275-281.

Becker, T., Knoche, M., 2012. Water induces microcracks in the grape berry cuticle. Vitis 51, 141-142.

Belton, P.S., Ratcliffe, R.G., 1985. NMR and compartmentation in biological tissues. Prog. Nucl. Magn. Reson. Spectrosc. 17, 241-279.

Billy, L., Mehinagic, E., Royer, G., Renard, C.M.G.C., Arvisenet, G., Prost, C., Jourjon, F., 2008. Relationship between texture and pectin composition of two apple cultivars during storage. Postharvest Biol. Technol. 47, 315-324.

Black, R.D., Early, T.A., Roemer, P.B., Mueller, O.M., Mogrocampero, A., Turner, L.G., Johnson, G.A., 1993. A high-temperature superconducting receiver for nuclear-magnetic-resonance microscopy. Science 259, 793-795.

Blahovec, J., Lahodová, M., 2012. DMA thermal analysis of different parts of potato tuber. Food Chemistry 133, 1101-1106.
Blahovec, J., Lahodová, M., Kindl, M., 2013. Temperature stimulated changes in potato and bean sprouts. J. Food Eng. 117, 299-303.
Blakeney, A.B., Harris, P.J., Henry, R.J., Stone, B.A., 1983. A simple and rapid preparation of alditol acetates for monosaccharide analysis. Carbohydrate Research 113, 291-299.
Blumenkrantz, N., Asboe-Hansen, G., 1973. New method for quantitative determination of uronic acids. Analytical biochemistry 54, 484-489.
Bonnet, C.S., Toth, E., 2010. MRI probes for sensing biologically relevant metal ions. Future Medicinal Chemistry 2, 367-384.
Bourne, M.C., 1982. Food texture and viscosity: concept and measurement.
Bremaud, I., Gril, J., Thibaut, B., 2011. Anisotropy of wood vibrational properties: dependence on grain angle and review of literature data. Wood Science and Technology 45, 735-754.
Brookfield, P.L., Nicoll, S., Gunson, F.A., Harker, F.R., Wohlers, M., 2011. Sensory evaluation by small postharvest teams and the relationship with instrumental measurements of apple texture. Postharvest Biol. Technol. 59, 179-186.
Brownstein, K.R., Tarr, C.E., 1979. Importance of classical diffusion in NMR studies of water in biological cells. Physical Review A 19, 2446-2453.
Bruce, D.M., 2003. Mathematical modelling of the cellular mechanics of plants. Philosophical Transactions of the Royal Society of London Series B-Biological Sciences 358, 1437-1444.
Brummell, D.A., 2006. Cell wall disassembly in ripening fruit. Functional Plant Biology 33, 103-119.
Bu-Contreras, R., Rao, M.A., 2002. Review: Dynamic rheological behavior of heated potatoes. Food Science and Technology International 8, 3-10.
Burdon, J., Clark, C., 2001. Effect of postharvest water loss on 'Hayward' kiwifruit water status. Postharvest Biol. Technol. 22, 215-225.
Burgert, I., Dunlop, J.W.C., 2011. Micromechanics of cell walls, In: Wojtaszek, P. (Ed.), Mechanical integration of plant cells and plants. Springer, Heidelberg, pp. 27-52.
Callaghan, P.T., 1991. Principles of Nuclear Magnetic Resonance Microscopy. Oxford Press.
Capitani, D., Brilli, F., Mannina, L., Proietti, N., Loreto, F., 2009. In Situ Investigation of Leaf Water Status by Portable Unilateral Nuclear Magnetic Resonance. Plant Physiol. 149, 1638-1647.
Carpita, N., McCann, M., 2000. The Cell Wall, Biochemistry & Molecular Biology of Plants.
Chanliaud, E., Burrows, K.M., Jeronimidis, G., Gidley, M.J., 2002. Mechanical properties of primary plant cell wall analogues. Planta 215, 989-996.
Chauvin, M.A., Ross, C.F., Pitts, M., Kupferman, E., Swanson, B., 2010. Relationship between instrumental and sensory determination of apple and pear texture. Journal of Food Quality 33, 181-198.
Chen, L., Opara, U.L., 2013. Texture measurement approaches in fresh and processed foods - A review. Food Res Int 51, 823-835.
Chen, P., McCarthy, M.J., Kauten, R., 1989. NMR for Internal Quality Evaluation of Fruits and Vegetables. Transactions of the ASAE 32, 1747-1753.
Cho, B.K., Chayaprasert, W., Stroshine, R.L., 2008a. Effects of internal browning and watercore on low field (5.4 MHz) proton magnetic resonance measurements of T-2 values of whole apples. Postharvest Biol. Technol. 47, 81-89.
Cho, B.K., Chayaprasert, W., Stroshine, R.L., 2008b. Effects of internal browning and watercore on low field (5.4 MHz) proton magnetic resonance measurements of T-2 values of whole apples. Postharvest Biol Technol 47, 81-89.

Clark, C.J., Burmeister, D.M., 1999. Magnetic resonance imaging of browning development in 'Braeburn' apple during controlled-atmosphere storage under high CO2. Hortscience 34, 915-919.
Clark, C.J., Drummond, L.N., MacFall, J.S., 1998a. Quantitative NMR imaging of kiwifruit (Actinidia deliciosa) during growth and ripening. J. Sci. Food Agric. 78, 349-358.
Clark, C.J., MacFall, J.S., 2003. Quantitative magnetic resonance imaging of 'Fuyu' persimmon fruit during development and ripening. Magn Reson Imaging 21, 679-685.
Clark, C.J., MacFall, J.S., Bieleski, R.L., 1998b. Loss of watercore from 'Fuji' apple observed by magnetic resonance imaging. Sci. Hortic. 73, 213-227.
Cosgrove, D.J., 1993. Wall extensibility - its nature, measurement and relationship to plant-cell growth. New Phytologist 124, 1-23.
Costa, F., Cappellin, L., Fontanari, M., Longhi, S., Guerra, W., Magnago, P., Gasperi, F., Biasioli, F., 2012. Texture dynamics during postharvest cold storage ripening in apple (Malus x domestica Borkh.). Postharvest Biol. Technol. 69, 54-63.
Cybulska, J., Zdunek, A., Konstankiewicz, K., 2011. Calcium effect on mechanical properties of model cell walls and apple tissue. J. Food Eng. 102, 217-223.
Daillant-Spinnler, B., MacFie, H.J.H., Beyts, P.K., Hedderley, D., 1996. Relationships between perceived sensory properties and major preference directions of 12 varieties of apples from the southern hemisphere. Food Quality and Preference 7, 113-126.
de Graaf, R.A., Brown, P.B., McIntyre, S., Nixon, T.W., Behar, K.L., Rothman, D.L., 2006. High magnetic field water and metabolite proton T-1 and T-2 relaxation in rat brain in vivo. Magn.Reson.Med. 56, 386-394.
De Guio, F., 2008. Compréhension et maîtrise des effets de susceptibilité magnétique air/matière en imagerie par résonance magnétique. Application à la caractérisation des produits alvéolés dans les procédés agroalimentaires. Rennes 1, Rennes.
De Guio, F., Benoit-Cattin, H., Davenel, A., 2008. Signal decay due to susceptibility-induced intravoxel dephasing on multiple air-filled cylinders: MRI simulations and experiments. Magnetic Resonance Materials in Physics Biology and Medicine 21, 261-271.
De Smedt, V., Pauwels, E., De Baerdemaeker, J., Nicolai, B., 1998. Microscopic observation of mealiness in apples: A quantitative approach. Postharvest Biol. Technol. 14, 151-158.
De Vries, J.A., Voragen, A.G.J., Rombouts, F.M., Pilnik, W., 1981. Extraction and purification of pectins from Alcohol Insoluble Solids from ripe and unripe apples. Carbohydrate Polymers 1, 117-127.
De Vries, J.A., Voragen, A.G.J., Rombouts, F.M., Pilnik, W., 1984. Changes in the structure of apple pectic substances during ripening and storage. Carbohydrate Polymers 4, 3-13.
Defraeye, T., Lehmann, V., Gross, D., Holat, C., Herremans, E., Verboven, P., Verlinden, B.E., Nicolai, B.M., 2013. Application of MRI for tissue characterisation of 'Braeburn' apple. Postharvest Biol Technol 75, 96-105.
Desbois, P., 1992. Repartition - mobilite et etats de l'eau dans les produits cerealiers de cuisson par resonance magnetique nucleaire. Universite de Nantes, p. 170.
Devaux, M.-F., Bouchet, B., Legland, D., Guillon, F., Lahaye, M., 2008. Macro-vision and grey level granulometry for quantification of tomato pericarp structure. Postharvest Biol. Technol. 47, 199-209.
Donker, H.C.W., Van As, H., Edzes, H.T., Jans, A.W.H., 1996. NMR imaging of white button mushroom (Agaricus bisporis) at various magnetic fields. Magn Reson Imaging 14, 1205-1215.
Dortch, R.D., Yankeelov, T.E., Yue, Z., Quarles, C.C., Gore, J.C., Does, M.D., 2009. Evidence of multiexponential T-2 in rat glioblastoma. NMR Biomed. 22, 609-618.
Duval, F., Cambert, M., Mariette, F., 2005. NMR study of tomato pericarp tissue by spin-spin relaxation and water self-diffusion. Appl Magn Reson 28, 29-40.

Edzes, H.T., van Dusschoten, D., Van As, H., 1998. Quantitative T-2 imaging of plant tissues by means of multi-echo MRI microscopy. Magnetic Resonance Imaging 16, 185-196.
Esau, K., 1977. The fruit, In: Wiley, J. (Ed.), Anatomy of seed plants, 2nd edn, New York, pp. 429-454.
FAO, 2014. FAOSTAT http://faostat.fao.org/site/339/default.aspx.
Fernandez-Seara, M.A., Wehrli, F.W., 2000. Postprocessing technique to correct for background gradients in image-based R-2(*) measurements. Magn.Reson.Med. 44, 358-366.
Fischer, M., Amadò, R., 1994. Changes in the pectic substances of apples during development and postharvest ripening. Part 1: Analysis of the alcohol-insoluble residue. Carbohydrate Polymers 25, 161-166.
Fisk, E.L., Millington W.F., 1962. Atlas of plant morphology. Portfolio II: Photomicrographs of flower, fruit and seed. Burgess, Minneapolis, Minnesota.
Fleischer, A., O'Neill, M.A., Ehwald, R., 1999. The pore size of non-graminaceous plant cell walls is rapidly decreased by borate ester cross-linking of the pectic polysaccharide rhamnogalacturonan II. Plant Physiol. 121, 829-838.
Fruk, G., Cmelik, Z., Jemric, T., Hribar, J., Vidrih, R., 2014. Pectin role in woolliness development in peaches and nectarines: A review. Sci. Hortic. 180, 1-5.
Fry, S.C., York, W.S., Albersheim, P., Darvill, A., Hayashi, T., Joseleau, J.P., Kato, Y., Lorences, E.P., Maclachlan, G.A., McNeil, M., Mort, A.J., Reid, J.S.G., Seitz, H.U., Selvendran, R.R., Voragen, A.G.J., White, A.R., 1993. An unambiguous nomenclature for xyloglucan-derived oligosaccharides. Physiol. Plant. 89, 1-3.
Galvez-Lopez, D., 2011. Etude des déterminants structuraux et génétiques de la texture de la pomme.
Galvez-Lopez, D., Laurens, F., Quemener, B., Lahaye, M., 2011. Variability of cell wall polysaccharides composition and hemicellulose enzymatic profile in an apple progeny. International journal of biological macromolecules 49, 1104-1109.
Gao, Q., Pitt, R.E., 1991. Mechanics of parenchyma tissue based on cell orientation and microstructure. Transactions of the ASAE 34, 232-238.
Goffinet, M.C., Robinson, T.L., Lakso, A.N., 1995. A comparison of 'empire' apple fruit size and anatomy in unthinned and hand-thinned trees. J. Horticult. Sci. 70, 375-387.
Gonzalez, J.J., Valle, R.C., Bobroff, S., Viasi, W.V., Mitcham, E.J., McCarthy, M.J., 2001. Detection and monitoring of internal browning development in 'Fuji' apples using MRI. Postharvest Biol. Technol. 22, 179-188.
Gonzalez, M.E., Barrett, D.M., McCarthy, M.J., Vergeldt, F.J., Gerkema, E., Matser, A.M., Van As, H., 2010. 1H-NMR Study of the Impact of High Pressure and Thermal Processing on Cell Membrane Integrity of Onions. J. Food Sci. 75, E417-E425.
Gwanpua, S.G., Van Buggenhout, S., Verlinden, B.E., Christiaens, S., Shpigelman, A., Vicent, V., Kermani, Z.J., Nicolai, B.M., Hendrickx, M., Geeraerd, A., 2014. Pectin modifications and the role of pectin-degrading enzymes during postharvest softening of Jonagold apples. Food Chemistry 158, 283-291.
Harada, T., Kurahashi, W., Yanai, M., Wakasa, Y., Satoh, T., 2005. Involvement of cell proliferation and cell enlargement in increasing the fruit size of Malus species. Sci. Hortic. 105, 447-456.
Harker, F.R., Hallett, I.C., 1992. Physiological changes associated with development of mealiness of apple fruit during cool storage. Hortscience 27, 1291-1294.
Harker, F.R., Maindonald, J., Murray, S.H., Gunson, F.A., Hallett, I.C., Walker, S.B., 2002. Sensory interpretation of instrumental measurements 1: texture of apple fruit. Postharvest Biol. Technol. 24, 225-239.
Harker, F.R., Redgwell, R.J., Hallett, I.C., Murray, S.H., Carter, G., 1997a. Texture of Fresh Fruit, Horticultural Reviews. John Wiley & Sons, Inc., pp. 121-224.

Harker, F.R., Stec, M.G.H., Hallett, I.C., Bennett, C.L., 1997b. Texture of parenchymatous plant tissue: A comparison between tensile and other instrumental and sensory measurements of tissue strength and juiciness. Postharvest Biol. Technol. 11, 63-72.
Harker, F.R., Sutherland, P.W., 1993. Physiological changes associated with fruit ripening and the development of mealy texture during storage of nectarines. Postharvest Biol. Technol. 2, 269-277.
Harker, F.R., White, A., Gunson, F.A., Hallett, I.C., De Silva, H.N., 2006. Instrumental measurement of apple texture: A comparison of the single-edge notched bend test and the penetrometer. Postharvest Biol. Technol. 39, 185-192.
Herremans, E., Melado-Herreros, A., Defraeye, T., Verlinden, B., Hertog, M., Verboven, P., Val, J., Fernández-Valle, M.E., Bongaers, E., Estrade, P., Wevers, M., Barreiro, P., Nicolaï, B.M., 2014. Comparison of X-ray CT and MRI of watercore disorder of different apple cultivars. Postharvest Biol Technol 87, 42-50.
Herremans, E., Verboven, P., Bongaers, E., Estrade, P., Verlinden, B.E., Wevers, M., Hertog, M., Nicolai, B.M., 2013. Characterisation of 'Braeburn' browning disorder by means of X-ray micro-CT. Postharvest Biol Technol 75, 114-124.
Hills, B.P., 1992a. The proton exchange cross-relaxation model of water relaxation in biopolymer systems. Mol. Phys. 76, 489-508.
Hills, B.P., 1992b. The proton exchange cross-relaxation model of water relaxation in biopolymer systems. Mol. Phys. 76, 509-523.
Hills, B.P., 2006. Applications of Low-Field NMR to Food Science, In: Webb, G.A. (Ed.), Annual Reports on Nmr Spectroscopy, Vol 58. Elsevier Academic Press Inc, San Diego, pp. 177-230.
Hills, B.P., Duce, S.L., 1990. The influence of chemical and diffusive exchange on water proton transverse relaxation in plant tissues. Magn Reson Imaging 8, 321-331.
Hills, B.P., Lefloch, G., 1994. NMR-studies of non-freezing water in cellular plant-tissue. Food Chemistry 51, 331-336.
Hills, B.P., Remigereau, B., 1997. NMR studies of changes in subcellular water compartmentation in parenchyma apple tissue during drying and freezing. Int. J. Food Sci. Technol. 32, 51-61.
Hills, B.P., Takacs, S.F., Belton, P.S., 1990. A new interpretation of proton NMR relaxation time measurements of water in food. Food Chemistry 37, 95-111.
Hinshaw, W.S., Bottomley, P.A., Holland, G.N., 1979. Demonstration of the resolution of NMR imaging in biological systems. Experientia 35, 1268-1269.
Hoebler, C., Barry, J.L., David, A., Delortlaval, J., 1989. Rapid acid-hydrolysis of plant-cell wall polysaccharides and simplified quantitative determination of their neutral monosaccharides by gas-liquid chromatography. J. Agric. Food Chem. 37, 360-367.
Ishida, N., Koizumi, M., Kano, H., 2000. The NMR microscope: a unique and promising tool for plant science. Annals of Botany 86, 259-278.
Jackman, R.L., Marangoni, A.G., Stanley, D.W., 1992. The effects of turgor pressure on puncture and viscoelastic properties of tomato tissue. Journal of Texture Studies 23, 491-505.
Jackman, R.L., Stanley, D.W., 1995. Perspective in the textural evaluation of plant foods. Trends in Food Science & Technology 6, 187-194.
Jaeger, S.R., Andani, Z., Wakeling, I.N., MacFie, H.J.H., 1998. Consumer preferences for fresh and aged apples: A cross-cultural comparison. Food Quality and Preference 9, 355-366.
James, H.J., Jobling, J.J., 2009. Contrasting the structure and morphology of the radial and diffuse flesh browning disorders and CO2 injury of ‘Cripps Pink’ apples. Postharvest Biol. Technol. 53, 36-42.
Jarvis, M.C., Briggs, S.P.H., Knox, J.P., 2003. Intercellular adhesion and cell separation in plants. Plant Cell Environ. 26, 977-989.
Johnston, J.W., 2001. Postharvest Apple Softening: Effects of At-harvest and Post-harvest Factors.

Johnston, J.W., Hewett, E.W., Hertog, M.L.A.T.M., 2002. Postharvest softening of apple (*Malus domestica*) fruit: a review. New Zealand Journal of Crop and Horticultural Science 30, 145-160.

Kaku, S., 1993. Monitoring stress sensitivity by water proton NMR relaxation-times in leaves of Azaleas that originated in different ecological habitats. Plant and Cell Physiology 34, 535-541.

Kaku, S., Iwayainoue, M., Toki, K., 1992. Anthocyanin influence on water proton NMR relaxation-times and water contents in leaves of evergreen woody plants during the winter. Plant and Cell Physiology 33, 131-137.

Khan, A.A., Vincent, J.F.V., 1990. Anisotropy of apple parenchyma. J. Sci. Food Agric. 52, 455-466.

Knee, M., 1973. Polysaccharides and glycoproteins of apple fruit cell walls. Phytochemistry 12, 637-653.

Knee, M., 1978a. Metabolism of polymethylgalacturonate in apple fruit cortical tissue during ripening. Phytochemistry 17, 1261-1264.

Knee, M., 1978b. Properties of polygalacturonate and cell cohesion in apple fruit cortical tissue. Phytochemistry 17, 1257-1260.

Konstankiewicz, K., Pawlak, K., Zdunek, A., 2001. Influence of structural parameters of potato tuber cells on their mechanical properties. International Agrophysics 15, 243-246.

Konstankiewicz, K., Zdunek, A., 2001. Influence of turgor and cell size on the cracking of potato tissue. International Agrophysics 15, 27-30.

Lahaye, M., Falourd, X., Quemener, B., Devaux, M.-F., Audergon, J.-M., 2014. Histological and cell wall polysaccharide chemical variability among apricot varieties. LWT - Food Science and Technology 58, 486-496.

Lahaye, M., Falourd, X., Quemener, B., Ralet, M.C., Howad, W., Dirlewanger, E., Arus, P., 2012a. Cell wall polysaccharide chemistry of peach genotypes with contrasted textures and other fruit traits. J. Agric. Food Chem. 60, 6594-6605.

Lahaye, M., Quemener, B., Causse, M., Seymour, G.B., 2012b. Hemicellulose fine structure is affected differently during ripening of tomato lines with contrasted texture. International Journal of Biological Macromolecules 51, 462-470.

Lara, I., Belge, B., Goulao, L.F., 2014. The fruit cuticle as a modulator of postharvest quality. Postharvest Biol. Technol. 87, 103-112.

Legland, D., Devaux, M.F., Bouchet, B., Guillon, F., Lahaye, M., 2012. Cartography of cell morphology in tomato pericarp at the fruit scale. Journal of Microscopy 247, 78-93.

Levigne, S., Thomas, M., Ralet, M.C., Quemener, B., Thibault, J.F., 2002. Determination of the degrees of methylation and acetylation of pectins using a C18 column and internal standards. Food Hydrocolloids 16, 547-550.

Lin, T.T., Pitt, R.E., 1986. Rheology of apple and potato tissue as affected by cell turgor pressure. Journal of Texture Studies 17, 291-313.

MacDougall, A.J., Rigby, N.M., Ryden, P., Tibbits, C.W., Ring, S.G., 2001. Swelling Behavior of the Tomato Cell Wall Network. Biomacromolecules 2, 450-455.

Maheswari, M., Joshi, D.K., Saha, R., Nagarajan, S., Gambhir, P.N., 1999. Transverse relaxation time of leaf water protons and membrane injury in wheat (Triticum aestivum L.) in response to high temperature. Annals of Botany 84, 741-745.

Malladi, A., Hirst, P.M., 2010. Increase in fruit size of a spontaneous mutant of 'Gala' apple (Malusxdomestica Borkh.) is facilitated by altered cell production and enhanced cell size. J. Exp. Bot. 61, 3003-3013.

Mariette, F., 2004. NMR retaxometry and MRI techniques: a powerful association in food science. C. R. Chim. 7, 221-232.

Mariette, F., Guillement, J.P., Tellier, C., Marchal, P., 1996. Continuous relaxation time distribution decomposition by MEM, In: Rutledge, D.N. (Ed.), Signal Treatment and Signal Analysis in NMR. Elsevier, Paris, pp. 218-234.

Mariette, F., Rodriguez, S., Lucas, T., Marchal, P., 1999. Influence de la déshydratation sur la répartition cellulaire de l'eau étudiée par relaxation RMN, Les produits alimentaires et l'eau, Agoral 99. Edition Tec & Doc, Nantes, pp. 417-422.

Marigheto, N., Venturi, L., Hibberd, D., Wright, K.M., Ferrante, G., Hills, B.P., 2007. Methods for peak assignment in low-resolution multidimensional NMR cross-correlation relaxometry. J Magn Reson 187, 327-342.

Marigheto, N., Venturi, L., Hills, B., 2008. Two-dimensional NMR relaxation studies of apple quality. Postharvest Biol. Technol. 48, 331-340.

Martinez, V.Y., Nieto, A.B., Castro, M.A., Salvatori, D., Alzamora, S.M., 2007. Viscoelastic characteristics of Granny Smith apple during glucose osmotic dehydration. J. Food Eng. 83, 394-403.

Massiot, P., Baron, A., Drilleau, J.F., 1996. Effect of storage of apple on the enzymatic hydrolysis of cell wall polysaccharides. Carbohydrate Polymers 29, 301-307.

Matas, A.J., Lopez-Casado, G., Cuartero, J., Heredia, A., 2005. Relative humidity and temperature modify the mechanical properties of isolated tomato fruit cuticles. Am. J. Bot. 92, 462-468.

McCarthy, M.J., Zion, B., Chen, P., Ablett, S., Darke, A.H., Lillford, P.J., 1995. Diamagnetic susceptibility changes in apple tissue after bruising. J Sci Food Agr 67, 13-20.

Mebatsion, H.K., Verboven, P., Endalew, A.M., Billen, J., Ho, Q.T., Nicolai, B.M., 2009. A novel method for 3-D microstructure modeling of pome fruit tissue using synchrotron radiation tomography images. J. Food Eng. 93, 141-148.

Mehinagic, E., Royer, G., Symoneaux, R., Bertrand, D., Jourjon, F., 2004. Prediction of the sensory quality of apples by physical measurements. Postharvest Biol. Technol. 34, 257-269.

Melado-Herreros, A., Munoz-Garcia, M.A., Blanco, A., Val, J., Fernandez-Valle, M.E., Barreiro, P., 2013. Assessment of watercore development in apples with MRI: Effect of fruit location in the canopy. Postharvest Biol. Technol. 86, 125-133.

Melado, A., Barreiro, P., Val, J., Blanco, A., Ruiz-Cabello, J., Rodriguez, I., 2010. Non destructive assessment of watercore in apples using MRI. disorder detection with HR-MAS.

Menard, K.P., 1998. Dynamic mechanical analysis: a practical introduction. CRC Press.

Mendoza, F., Verboven, P., Mebatsion, H.K., Kerckhofs, G., Wevers, M., Nicolai, B., 2007. Three-dimensional pore space quantification of apple tissue using X-ray computed microtomography. Planta 226, 559-570.

Mitra, P.P., Sen, P.N., Schwartz, L.M., 1993. Short-time behavior of the diffusion-coefficient as a geometrical probe of porous media. Physical Review B 47, 8565-8574.

Mitra, P.P., Sen, P.N., Schwartz, L.M., Ledoussal, P., 1992. Diffusion propagator as a probe of the structure of porous media. Physical Review Letters 68, 3555-3558.

Mohnen, D., 2008. Pectin structure and biosynthesis. Current Opinion in Plant Biology 11, 266-277.

Moller, S.M., Travers, S., Bertram, H.C., Bertelsen, M.G., 2013. Prediction of postharvest dry matter, soluble solids content, firmness and acidity in apples (cv. Elshof) using NMR and NIR spectroscopy: a comparative study. Eur. Food Res. Technol. 237, 1021-1024.

Musse, M., Cambert, M., Mariette, F., 2010a. NMR Study of Water Distribution inside Tomato Cells: Effects of Water Stress. Appl. Magn. Reson. 38, 455-469.

Musse, M., De Franceschi, L., Cambert, M., Sorin, C., Le Caherec, F., Burel, A., Bouchereau, A., Mariette, F., Leport, L., 2013. Structural changes in senescing oilseed rape leaves at tissue and subcellular levels monitored by nuclear magnetic resonance relaxometry through water status. Plant Physiol. 163, 392-406.

Musse, M., De Guio, F., Quellec, S., Cambert, M., Challois, S., Davenel, A., 2010b. Quantification of microporosity in fruit by MRI at various magnetic fields: comparison with X-ray microtomography. Magnetic Resonance Imaging 28, 1525-1534.
Musse, M., Quellec, S., Cambert, M., Devaux, M.F., Lahaye, M., Mariette, F., 2009. Monitoring the postharvest ripening of tomato fruit using quantitative MRI and NMR relaxometry. Postharvest Biol. Technol. 53, 22-35.
Oey, M.L., Vanstreels, E., De Baerdemaeker, J., Tijskens, E., Ramon, H., Hertog, M.L.A.T.M., Nicolai, B., 2007. Effect of turgor on micromechanical and structural properties of apple tissue: A quantitative analysis. Postharvest Biol. Technol. 44, 240-247.
Otsu, N., 1979. Threshold selection method from gray-level histograms. IEEE Trans Syst Man Cybern SMC-9, 62-66.
Palmer, J.W., Harker, F.R., Tustin, D.S., Johnston, J., 2010. Fruit dry matter concentration: a new quality metric for apples. J. Sci. Food Agric. 90, 2586-2594.
Pena, M.J., Carpita, N.C., 2004. Loss of highly branched arabinans and debranching of rhamnogalacturonan I accompany loss of firm texture and cell separation during prolonged storage of apple. Plant Physiol. 135, 1305-1313.
R Core Team, 2013. R: A Language and Environment for Statistical Computing. R Foundation for Statistical Computing, Vienna, Austria.
Raffo, A., Gianferri, R., Barbieri, R., Brosio, E., 2005. Ripening of banana fruit monitored by water relaxation and diffusion H-1-NMR measurements. Food Chem. 89, 149-158.
Ralet, M.-C., Williams, M.A.K., Tanhatan-Nasseri, A., Ropartz, D., Quemener, B., Bonnin, E., 2012. Innovative Enzymatic Approach to Resolve Homogalacturonans Based on their Methylesterification Pattern. Biomacromolecules 13, 1615-1624.
Ratcliffe, R.G., Roscher, A., Shachar-Hill, Y., 2001. Plant NMR spectroscopy. Prog. Nucl. Magn. Reson. Spectrosc. 39, 267-300.
Ray, S., Vigouroux, J., Quemener, B., Bonnin, E., Lahaye, M., 2014. Novel and diverse fine structures in LiCl-DMSO extracted apple hemicelluloses. Carbohydrate Polymers 108, 46-57.
Redgwell, R.J., MacRae, E., Hallett, I., Fischer, M., Perry, J., Harker, R., 1997. In vivo and in vitro swelling of cell walls during fruit ripening. Planta 203, 162-173.
Renard, C.M.G.C., Voragen, A.G.J., Thibault, J.F., Pilnik, W., 1990. Studies on apple protopectin: I. Extraction of insoluble pectin by chemical means. Carbohydrate Polymers 12, 9-25.
Rokitta, M., Rommel, E., Zimmermann, U., Haase, A., 2000. Portable nuclear magnetic resonance imaging system. Review of Scientific Instruments 71, 4257-4262.
Ropartz, D., Bodet, P.-E., Przybylski, C., Gonnet, F., Daniel, R., Fer, M., Helbert, W., Bertrand, D., Rogniaux, H., 2011. Performance evaluation on a wide set of matrix-assisted laser desorption ionization matrices for the detection of oligosaccharides in a high-throughput mass spectrometric screening of carbohydrate depolymerizing enzymes. Rapid Communications in Mass Spectrometry 25, 2059-2070.
Scheenen, T.W.J., van Dusschoten, D., de Jager, P.A., Van As, H., 2000. Quantification of water transport in plants with NMR imaging. J. Exp. Bot. 51, 1751-1759.
Schneider, C.A., Rasband, W.S., Eliceiri, K.W., 2012. NIH Image to ImageJ: 25 years of image analysis. Nat Meth 9, 671-675.
Schotsmans, W., Verlinden, B.E., Lammertyn, J., Nicolai, B.M., 2004. The relationship between gas transport properties and the histology of apple. J. Sci. Food Agric. 84, 1131-1140.
Schultink, A., Liu, L., Zhu, L., Pauly, M., 2014. Structural Diversity and Function of Xyloglucan Sidechain Substituents. Plants 3, 526-542.
Scilab, 2012, v5.3.3. Scilab entreprises, Orsay, France,
Sibgatullin, T.A., Anisimov, A.V., de Jager, P.A., Vergeldt, F.J., Gerkema, E., Van As, H., 2007. Analysis of diffusion and relaxation behavior of water in apple parenchymal cells. Biofizika 52, 268-276.

Sibgatullin, T.A., Vergeldt, F.J., Gerkema, E., Van As, H., 2010. Quantitative permeability imaging of plant tissues. Eur. Biophys. J. Biophys. Lett. 39, 699-710.
Singh, F., Katiyar, V.K., Singh, B.P., 2014. Analytical study of turgor pressure in apple and potato tissues. Postharvest Biol. Technol. 89, 44-48.
Slavov, A., Garnier, C., Crepeau, M.-J., Durand, S., Thibault, J.-F., Bonnin, E., 2009. Gelation of high methoxy pectin in the presence of pectin methylesterases and calcium. Carbohydrate Polymers 77, 876-884.
Snaar, J.E.M., 2002. NMR of Porous Bio-systems.
Snaar, J.E.M., Van as, H., 1992. Probing water compartments and membran-permeability in plant-cells by H-1-NMR relaxation measurements. Biophysical Journal 63, 1654-1658.
Song, Y.Q., Venkataramanan, L., Hurlimann, M.D., Flaum, M., Frulla, P., Straley, C., 2002. T-1-T-2 correlation spectra obtained using a fast two- dimensional Laplace inversion. J Magn Reson 154, 261-268.
StatPoint Technologies, I., 2010. XVI Statgraphics Centurion, 16.1.11 ed, Herndon, VA.
Sukstanskii, A.L., Yablonskiy, D.A., 2003. Gaussian approximation in the theory of MR signal formation in the presence of structure-specific magnetic field inhomogeneities. Journal of Magnetic Resonance 163, 236-247.
Suzuki, T., Sasaki, Y., Kuroda, K. and Oosawa, K., 2003. Histological features and dynamics of the development of watercore in apple (*Malus Domestica*) fruit. 628, 495-500.
Systat, 2007. TableCurve 2D. Systat, San Jose, California.
Szczesniak, A.S., 2002. Texture is a sensory property. Food Quality and Preference 13, 215-225.
Taglienti, A., Massantini, R., Botondi, R., Mencarelli, F., Valentini, M., 2009. Postharvest structural changes of Hayward kiwifruit by means of magnetic resonance imaging spectroscopy. Food Chemistry 114, 1583-1589.
Talbott, L.D., Ray, P.M., 1992. Molecular-size and separability features of pea cell-wall polysaccharides - implications for models of primary wall structure. Plant Physiol. 98, 357-368.
Tibbits, C.W., MacDougall, A.J., Ring, S.G., 1998. Calcium binding and swelling behaviour of a high methoxyl pectin gel. Carbohydrate Research 310, 101-107.
Ting, V.J.L., Silcock, P., Bremer, P.J., Biasioli, F., 2013. X-Ray Micro-Computer Tomographic Method to Visualize the Microstructure of Different Apple Cultivars. J. Food Sci. 78, E1735-E1742.
Toivonen, P.M.A., Brummell, D.A., 2008. Biochemical bases of appearance and texture changes in fresh-cut fruit and vegetables. Postharvest Biol. Technol. 48, 1-14.
Tong, C., Krueger, D., Vickers, Z., Bedford, D., Luby, J., El-Shiekh, A., Shackel, K., Ahmadi, H., 1999. Comparison of softening-related changes during storage of 'Honeycrisp' apple, its parents, and 'Delicious'. Journal of the American Society for Horticultural Science 124, 407-415.
Torrey, H.C., 1956. Bloch Equations with Diffusion Terms. Physical Review 104, 563-565.
Tu, S.S., Choi, Y.J., McCarthy, M.J., McCarthy, K.L., 2007. Tomato quality evaluation by peak force and NMR spin-spin relaxation time. Postharvest Biol. Technol. 44, 157-164.
Van As, H., 2007. Intact plant MRI for the study of cell water relations, membrane permeability, cell-to-cell and long distance water transport. J. Exp. Bot. 58, 743-756.
Van as, H., Reinders, J.E.A., Dejager, P.A., Vandesanden, P., Schaafsma, T.J., 1994. In-situ plant water-balance studies using a portable NMR spectrometer. J. Exp. Bot. 45, 61-67.
Van As, H., van Duynhoven, J., 2013. MRI of plants and foods. J Magn Reson 229, 25-34.
Van der Toorn, A., 2000. Developmental changes and water status in tulip bulbs during storage: visualisation by NMR imaging. J. Exp. Bot. 51, 1277-1287.

Van der Weerd, L., Claessens, M., Ruttink, T., Vergeldt, F.J., Schaafsma, T.J., Van As, H., 2001. Quantitative NMR microscopy of osmotic stress responses in maize and pearl millet. J. Exp. Bot. 52, 2333-2343.

Varela, P., Salvador, A., Fiszman, S., 2007. Changes in apple tissue with storage time: Rheological, textural and microstructural analyses. J. Food Eng. 78, 622-629.

Vaysse P., L.P., 2004. Pomme-poire de la récolte au conditionnement: outils pratiques. CTIFL.

Veraverbeke, E.A., Verboven, P., Scheerlinck, N., Hoang, M.L., Nicolai, B.M., 2003a. Determination of the diffusion coefficient of tissue, cuticle, cutin and wax of apple. J. Food Eng. 58, 285-294.

Veraverbeke, E.A., Verboven, P., Van Oostveldt, P., Nicolai, B.M., 2003b. Prediction of moisture loss across the cuticle of apple (Malus sylvestris subsp mitis (Wallr.)) during storage Part 1. Model development and determination of diffusion coefficients. Postharvest Biol. Technol. 30, 75-88.

Veraverbeke, E.A., Verboven, P., Van Oostveldt, P., Nicolai, B.M., 2003c. Prediction of moisture loss across the cuticle of apple (Malus sylvestris subsp mitis (Wallr.)) during storage: part 2. Model simulations and practical applications. Postharvest Biol. Technol. 30, 89-97.

Verboven, P., Kerckhofs, G., Mebatsion, H.K., Ho, Q.T., Temst, K., Wevers, M., Cloetens, P., Nicolai, B.M., 2008. Three-dimensional gas exchange pathways in pome fruit characterized by synchrotron x-ray computed tomography. Plant Physiol. 147, 518-527.

Vincent, J., 2012. Structural Biomaterials: Third Edition. Princeton University Press.

Vincent, J.F.V., 1989. Relationship between density and stiffness of apple flesh. J. Sci. Food Agric. 47, 443-462.

Volz, R.K., Harker, F.R., Hallet, I.C., Lang, A., 2004. Development of texture in apple fruit - A biophysical perspective. Acta Horticulturae 636, 473-479.

Volz, R.K., Harker, F.R., Lang, S., 2003. Firmness decline in 'Gala' apple during fruit development. Journal of the American Society for Horticultural Science 128, 797-802.

Wang, S.Y., Wang, P.C., Faust, M., 1988. Non-destructive detection of watercore in apple with nuclear magnetic-resonance imaging. Sci. Hortic. 35, 227-234.

Wang, Y., Li, X., Sun, G., Li, D., Pan, Z., 2014. A comparison of dynamic mechanical properties of processing-tomato peel as affected by hot lye and infrared radiation heating for peeling. J. Food Eng. 126, 27-34.

Watada, A.E., Abbott, J.A., Hardenburg, R.E., 1980. Sensory characteristics of apple fruit. Journal of the American Society for Horticultural Science 105, 371-375.

Wu, J., Guo, K.Q., 2010. Dynamic viscoelastic behaviour and microstructural changes of Korla pear (Pyrus bretschneideri rehd) under varying turgor levels. Biosyst. Eng. 106, 485-492.

Xu, C., Li, Y., 2014. Development of carrot parenchyma softening during heating detected in vivo by dynamic mechanical analysis. Food Control 44, 214-219.

Yablonskiy, D.A., 1998. Quantitation of intrinsic magnetic susceptibility-related effects in a tissue matrix. Phantom study. Magn.Reson.Med. 39, 417-428.

Yablonskiy, D.A., Haacke, E.M., 1994. Theory of the NMR signal behavior in megnetically inhomogeneous tissues - the static dephasing regime. Magn.Reson.Med. 32, 749-763.

Yoshioka, H., Aoba, K., Kashimura, Y., 1992. Molecular-weight and degree of methoxylation in cell-wall polyuronide during softening in pear and apple fruit. Journal of the American Society for Horticultural Science 117, 600-606.

Zhang, L., McCarthy, M.J., 2013. Assessment of pomegranate postharvest quality using nuclear magnetic resonance. Postharvest Biol. Technol. 77, 59-66.

Zimmerman, J.R., Brittin, W.E., 1957. Nuclear Magnetic Resonance Studies in Multiple Phase Systems: Lifetime of a Water Molecule in an Adsorbing Phase on Silica Gel. The Journal of Physical Chemistry 61, 1328-1333.

Appendix

Appendix

I. MRI MEASUREMENTS AND FITTING

Apples were placed on a specifically designed support made to fit the shape of the RF coil and each fruit was carefully marked before the first experiment to allow the fruit to be placed nearly in the same position during subsequent experiments (Figure 1).

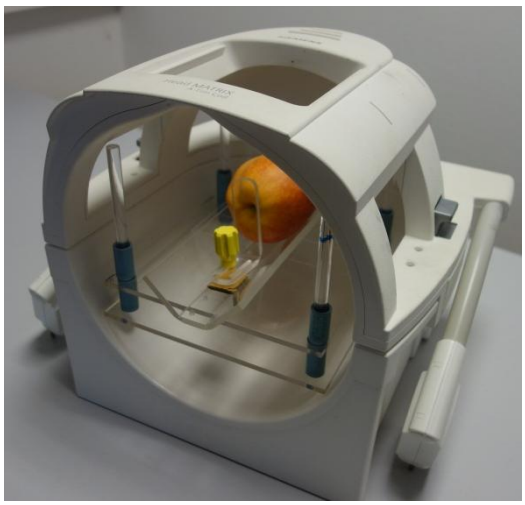

Figure 1: experimental support and head receiver coil used for the measurements.

Two sequences were used: 1\ MSE sequence, 512 echoes. TE = 7.1 ms, TR = 10 s, 1 acc, BW = 256 Hz/pixel, FOV = 152 mm x 152 mm, matrix = 128 x 128 and 2\ MGE, 12 echoes. TE1 = 2.8 ms, ΔTE = 1.6 ms. TR = 10s, 2 acc, BW = 2090 Hz/pixel, FOV = 152 mm x 152 mm, matrix = 128 x 128. An example of the images obtained for the two sequences is shown on Figure 0-2.

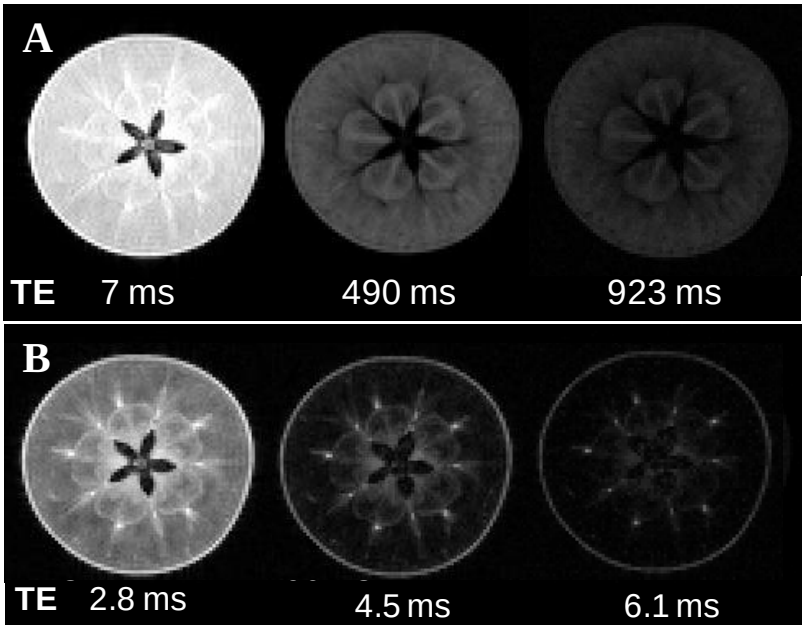

Figure 3: Example of images from (A) MSE and (B) MGE sequences at different echo times for the same fruit Granny Smith at one-month storage time.

Relaxation parameters were then computed on a pixel basis (mono-exponential T_2, T_2* and apparent microporosity maps) and on the mean signal of the ROIs (multi-exponential T_2 and apparent microporosity of the regions). The ROI-based approach was used as it improved the SNR.

For the ROIs, a tri-exponential fitting equation (Equation 1) was chosen to fit T_2 relaxation curves. I_{0i} and T_{2i} correspond to the relative intensities and transverse relaxation times, respectively, of the different components of the signal.

$$I(t) = \sum_{i=0}^{3} I_{0i} \times e^{-\frac{t}{T_{2i}}} + const$$

Equation 1

The choice of this tri-exponential model was motivated by the results of previous studies in MRI (Adriaensen et al., 2013). Levenberg-Marquardt algorithm was used for fitting. Initial parameters used were the relaxation parameters obtained in preliminary experiments on each cultivar and for each ROI. As an example, parameters used for the outer ROI is shown in Table 1. Seven parameters were adjusted (intensities and

relaxation times for three components and an offset). The mean SNR for one voxel was approximately 120 in outer parenchyma ROI and the mean size of the corresponding ROI was approximately 350 voxels.

Table 1: Initial parameters used for tri-exponential fitting on outer cortex ROIs for the different cultivars studied

	T_{21} (ms)	T_{22} (ms)	T_{23} (ms)	I_{01} (a.u.)	I_{02} (a.u.)	I_{03} (a.u.)	offset (a.u.)
Fuji caliber 1	20	120	480	20	130	780	10
Fuji caliber 2	25	120	520	30	150	840	10
Fuji caliber 3	25	130	550	30	150	900	10
Ariane	30	140	530	35	160	860	10
Granny Smith	25	140	550	30	170	830	10
EC	20	90	280	10	140	650	10

Table 2 shows an example of the results of the fitting for Ariane cultivar and an example of the experimental data and the corresponding fitted curve is presented on Figure 4.

Table 2: Example of fitting results for Ariane fruit at 1-month storage time

T_{21} (ms)	T_{22} (ms)	T_{23} (ms)	I_{01} (a.u.)	I_{02} (a.u.)	I_{03} (a.u.)	offset (a.u.)
25 ± 3	135 ± 3	530 ± 1	38.0 ± 2.3	164.4 ± 1.9	844.5 ± 2.2	8.7 ± 0.1

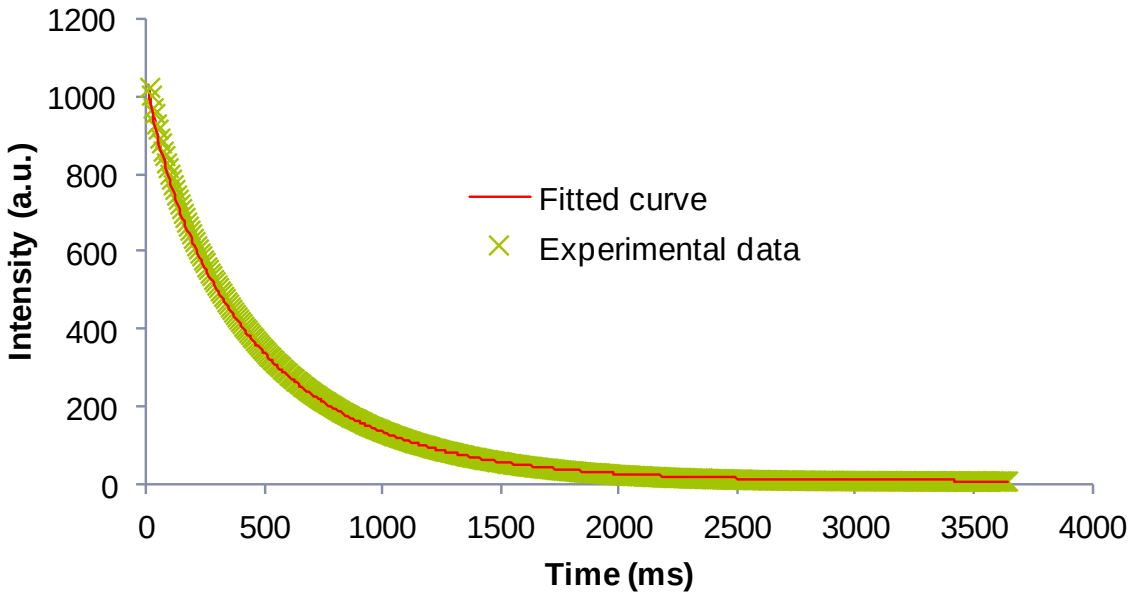

Figure 4: Typical transverse magnetization decay curve measured in outer cortex of an apple and its fit by tri-exponential model

II. ACCURACY OF TRI-EXPONENTIAL FITTING

In order to estimate the accuracy of the multi-exponential fitting, Monte Carlo simulations were performed by using the software Scilab (Scilab, 2012). Relaxation parameters fitted on the experimental data (Table 3) were used to compute the simulation curves. The value of noise for one pixel (σ) was estimated from the background of the images, as $\sigma = \text{mean}_b / \sqrt{\frac{\pi}{2}}$, with mean_b the means value of the intensity computed in the region of the interest of the image background. The signal to noise ratio for one pixel (SNR) of the first image of the MSE sequence (TE=7.1 ms) was about 120.

Table 3: values used to compute the curve used for simulations

T_{21} (ms)	T_{22} (ms)	T_{23} (ms)	I_{01} (au)	I_{02} (au)	I_{03} (au)
22	138	532	45	153	853

A randomly distributed Gaussian noise was added on both real and imaginary parts leading to a Rician noise on the resulting curve. Two conditions were studied by varying the number of the voxels (V) used for averaging the signal in the experimental studies (see Chapter 3), by using noise values computed as $\frac{\sigma}{\sqrt{V}}$ with V fixed at 175 and 350, corresponding to the approximate size of the ROIs of the inner and outer parenchyma used. Such obtained curves were fitted by Equation 1 with the initial guesses for the regression set at the values used for computing of the simulated T_2 relaxation curves (Table 3). A bias and a standard deviation were then computed for all parameters fitted which are presented in Table 4.

Table 4: Mean bias and standard deviations resulting from the simulation for tri-exponential fitting parameters

	ROI	I_{01} (%)	T_{21} (ms)	I_{02} (%)	T_{22} (ms)	I_{03} (%)	T_{23} (ms)
Bias	**Inner**	-0.06	-0.78	-0.19	-3.50	0.44	-1.76
	Outer	-0.04	-0.41	-0.11	-1.93	0.24	-0.98
Standard Deviation	**Inner**	0.19	2.15	0.18	3.65	0.34	0.97
	Outer	0.14	1.63	0.13	2.82	0.26	0.75

The values obtained for both bias and standard deviations of all parameters were relatively low. In particular, their values were acceptable when compared to the variations measured in our studied between different cultivars or tissues characterized by different cell sizes (see previous chapters).

III. ACCURACY OF APPARENT MICROPOROSITY ESTIMATION

As for multi-exponential T_2 measurements, the accuracy of apparent microporosity estimation was investigated. A mono exponential decay curve (Equation 2) was fitted for both T_2 and T_2* relaxation signals. The mean SNR of the first image in the outer cortex region was 80 for T_2* images and 120 for T_2 images.

$$I(t) = \mathrm{I}(0) \times e^{-\frac{t}{T_2}} + const$$

Equation 2

Apparent microporosity was computed according to the equation $\varepsilon = \frac{9\sqrt{3}R_2^{\#}}{2\pi\gamma\Delta\chi B_0}, with\ R_2^{\#} = \frac{1}{T_2^*} - \frac{1}{T_2}$, ε the apparent microporosity, γ the proton gyromagnetic ratio, Δχ the difference of magnetic susceptibility between water and air and B_0 the magnetic field. T_2* is the main source of error on apparent microporosity estimation. As a consequence, during simulation, only the values of T_2* were varied. The error from other parameters was neglected. As for multi-exponential fitting, initial parameters were chosen to be in agreement with experimental data: amplitude was 1500 a.u and T_2* was varied from 1 to 4 ms. 30 000 fitting were performed for each T_2* value and for 1 voxel (maps), 175-voxel and 350-voxel ROIs. Bias and standard deviation are shown on Figure 5.

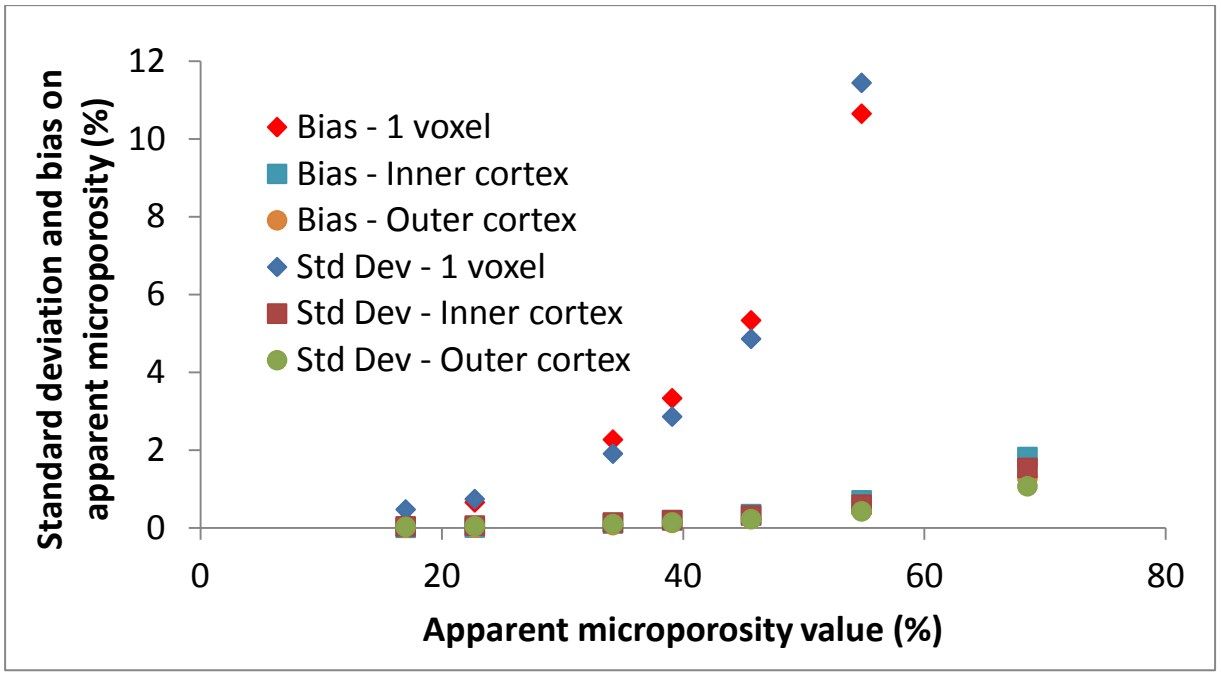

Figure 5: Mean bias and standard deviations resulting from the simulation for apparent microporosity estimations

The results showed that an important standard deviation and bias were observed for high values of apparent microporosity for 1 voxel (>40%), while the bias and standard deviation computed on ROIs were acceptable in the whole range of apparent microporosities studied. The statistics were made by using the ROI-based approach. The variations due to cultivar or apple size changes remain higher than these bias and standard deviation.